DEVELOPMENT AND APPLICATION OF HYPERPOLARIZED KRYPTON-83 AS A NEW MRI CONTRAST AGENT

THEODORE WILLIAM BRUCE HUGHES-RILEY, BSc (Hons.)

Thesis submitted to the University of Nottingham for the degree of Doctor of Philosophy

DECEMBER 2014

Abstract

Development and application of hyperpolarized krypton-83 as a new MRI contrast agent

Hyperpolarized (hp) gases such ^{129}Xe and ^{83}Kr (spin $I = 1/2$ and $I = 9/2$ respectively) can allow for significantly enhanced signal in a number of magnetic resonance applications. As a result there has been a growing interest in recent years to advance hp noble gas technology to non-invasively image the airspace of lungs, with the goal of developing a helpful probe for lung pathologies. ^{83}Kr longitudinal relaxation (T_1) has been shown to be sensitive to various surface properties, and may prove to be an interesting for identifying certain diseases including those that change surface chemistry (such as cystic fibrosis) or the surface-to-volume ratio in the lung (like in emphysema).

This thesis contains several studies furthering ^{83}Kr lung imaging, while also exploring methods for ^{129}Xe imaging. A major focus has been on increasing spin polarization of the noble gases, as an increased polarization yields a greater MR signal strength. A novel low-pressure spin-exchange optical pumping technique has been utilized in this work allowing for ^{83}Kr polarizations exceeding 17.5 %; as opposed to 4.4 % previously reported in literature.

Gas produced in this fashion must be pressurized to above ambient before it is possible for it to be delivered to a lung. Two methodologies for pressurizing the noble gas via compression are explored and optimized for hp gas delivery to excised lungs with ^{83}Kr polarizations as high as 13.8 % achievable after compression. This ultimately allowed for the first ever coronal ^{83}Kr lung images in an *ex vivo* lung model. Further work repeated with isotopically enriched ^{83}Kr achieved a surface-sensitive T_1 relaxation map in this system.

Finally gas handling techniques where created to allow for efficient and thorough mixing of the hp noble gases and O_2 while minimizing relaxation effects. This is vital for any future *in vivo* studies.

List of publications

Publications

Joseph S. Six, **Theodore Hughes – Riley**, David M.L. Lilburn, Alan C. Dorkes, Karl F. Stupic, Dominick E. Shaw, Peter G. Morris, Ian P. Hall, Galina E. Pavlovskaya, Thomas Meersmann (2013). Pulmonary MRI contrast using surface quadrupolar relaxation (SQUARE) of hyperpolarized ^{83}Kr. *Magnetic Resonance Imaging* (2014)*, 32*(1), 48-53.

Theodore Hughes-Riley, Joseph S. Six, David M.L. Lilburn, Karl F. Stupic, A.C. Dorkes, Dominick E. Shaw, Galina E. Pavlovskaya, Thomas Meersmann, Cryogenics free production of hyperpolarized ^{129}Xe and ^{83}Kr for biomedical MRI applications, *Journal of Magnetic Resonance* (2013), 237, 23-33.

David M. L. Lilburn, **Theodore Hughes-Riley**, Joseph S. Six, Karl F. Stupic, Dominick E. Shaw, Galina E. Pavlovskaya, Thomas Meersmann (2013). Validating Excised Rodent Lungs for Functional Hyperpolarized Xenon-129 MRI. *PloS one*, *8*(8), e73468.

Joseph S. Six, **Theodore Hughes-Riley**, Karl F. Stupic, Galina E. Pavlovskaya, Thomas Meersmann (2012). Pathway to Cryogen Free Production of Hyperpolarized Krypton-83 and Xenon-129. *PloS one*, *7*(11), e49927.

Selected conference proceedings

Theodore Hughes-Riley, Joseph S. Six, David Lilburn, Karl F. Stupic, Galina E. Pavlovskaya, Thomas Meersmann. "Exploring T_1 and T_2 relaxation in excised rat lungs" XeMat 2012, Dublin, Ireland, June 27-29. (Presentation)

Theodore Hughes-Riley, Joseph S. Six, Mathieu Baudin, Galina E. Pavlovskaya, Thomas Meersmann, "Hyperpolarization of noble gases via spin-exchange optical pumping using line-narrowed laser sources to achieve high levels of spin polarization" EUROMAR 2011, Frankfurt, Germany, August 21 – 25, 2011. (Poster)

‘Calm seas never made a good sailor.’

Acknowledgements

I would like to acknowledge a number of people for both their professional and personal support in the writing of this thesis and collection of the contained data. I think that it's only proper to start by thanking to Professor Thomas Meersmann, my principle PhD supervisor. I am grateful for the opportunity that working for him has given me, and for his time, support and mentorship over the years. I am also appreciative to my other supervisors Professor Ian Hall and Professor Peter Morris for their advice and input over the duration of my PhD.

I'd like to thank Joseph Six and Dr David Lilburn, fellow PhD students and two people whom I have spent many late nights with collecting data. They have been instrumental in conducting the experimental work in this thesis and have both become dear friends. I'd like to thank Dr Karl Stupic for his part in my training during my PhD and as seen from the list of publications earlier the critical role he played in all of the research I was part of. Similarly I'd like to express my gratitude to Dr Galina Pavlovskaya for her insight and assistance. I also want to make sure that I mention Clémentine Lesbats and Mathieu Baudin, both of whose support was greatly appreciated.

I am of course very thankful also to others that have helped make this research possible including Clive Dixon, Alan Dorkes, Mike Olsen, Ian Taylor, and Ian Thexton for constructing the wealth of specialized glassware and equipment used throughout this work.

I have also received a lot of support from the many friends I have made in the Sir Peter Mansfield Magnetic Resonance Centre. While I'd like to, I can't list everyone here, but all the same you have my gratitude.

I am also very grateful for friends and family for their encouragement. While again I can't list everyone (mainly to keep the printing costs down) I want to specifically thank my parents, Nigel and Gaye Hughes-Riley. Additionally I'd like to show my appreciation to Christopher Joyce and Mathew Perry (not the actor).

Finally I would like to acknowledge and thank the Medical Research Council for funding me through my PhD.

Thesis Contents

Chapter 1

An introduction to hyperpolarized gas research and its application towards lung studies

1.1 Overview

While magnetic resonance imaging (MRI) has proven to be a useful tool for detecting and characterizing a number of diseases since its conception in 1973 [2, 3], pulmonary MRI is problematic due to the relatively low tissue density of the lung [4] and the resulting poor MRI signal strength. As pulmonary pathology is a leading cause of death in the world, there is great interest in developing techniques to better identify and characterize these diseases.

An example is COPD (Chronic Obstructive Pulmonary Disease), a disease where there is a breakdown of lung tissue, and a deterioration of small airways. COPD alone is the fifth most likely cause of death in the United States, the annual death rate for the disease having doubled in just over thirty years[5]. Other obstructive lung diseases include chronic bronchitis, and asthma. Obstructive pathologies are not the only lung diseases of interest; emphysema, cystic fibrosis, asthma, acute lung injury, and acute respiratory syndrome are some examples.

Albert *et al.* [6] proposed a technique utilizing hyperpolarized ^{129}Xe (spin $I = 1/2$) to allow direct imaging of the lung airspaces with significantly improved signal intensity to that of a regular proton MRI. The use of hyperpolarized gases, including ^{3}He (spin $I = 1/2$), as a contrast agent for lung imaging has since gained a sizeable following [6-9].

The quadrupolar, MR-active, noble gas isotope ^{83}Kr (spin $I = 9/2$) has also been explored as a potential probe for lung pathologies [1, 10, 11]. Due to its nuclear electric quadrupole moment (eQ) the T_1 relaxation of ^{83}Kr is dominated by surface interactions making it a potential surface probe for the lung parenchyma [1]. Having a lower gyromagnetic ratio than other NMR active noble gases used for imaging, ^{83}Kr T_1 relaxation is not dominated by the presence of paramagnetic molecules, such as oxygen, enabling it to provide T_1 contrast in the gas phase *in vivo*.

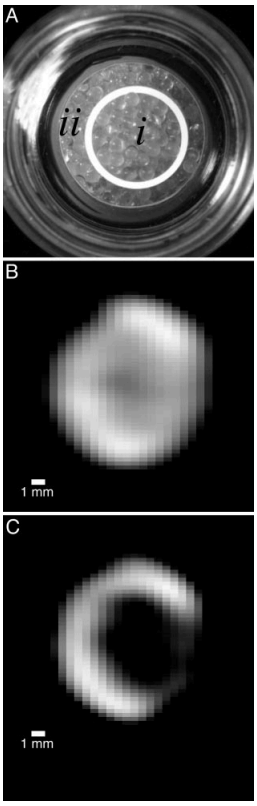

Fig. 1.1 *– Diagram reproduced from the literature [1] highlighting surface-dependant ^{83}Kr T_1 MRI contrast. (**a**) A photograph of a closely packed glass bead sample. The beads at the centre, **i**, of the sample have been treated with a siliconizing agent that drastically reduces the T_1 time of ^{83}Kr (T_1 = 9 sec). Untreated beads have a T_1 = 35 sec. (**b**) MR image of the sample after 3 seconds. T_1 is sufficiently long for all beads that the signal strength of the ^{83}Kr is uniform for the most part. (**c**) MR image of the sample after 9 seconds. The T_1 of the silicon beads is only 9 seconds. Therefore at this point the majority of the ^{83}Kr in contact with the siliconized beads has relaxed causing a significantly reduced signal intensity in the centre. The figure demonstrates that T_1 weighted ^{83}Kr MRI contrast is responsive to surface chemistry. Used in accordance with the PNAS reprint policy. © 2005 National Academy of Sciences, USA.*

The purpose of this work is to improve our understanding of hyperpolarized noble gases in order to optimise our handling, storage, and delivery of these gases. The ultimate objective of this ongoing effort is to further develop hyperpolarized ^{83}Kr for use in lung studies in pre-clinical and eventually clinical settings. In the process of developing hyperpolarized ^{83}Kr, hp ^{129}Xe production and usage was also investigated; primarily because in a clinical setting ^{83}Kr MRI would likely be a complimentary modality to ^{129}Xe imaging. ^{129}Xe is also well explored in the literature, therefore understanding the well-reported behaviour of hp ^{129}Xe could make it easier to understand the behaviour of ^{83}Kr.

This thesis will begin with two chapters outlining the background and theory of the work presented. The bulk of the thesis will comprise a number of experimental chapters.

Chapter 3, *Optimizing the spin-exchange optical pumping process for ^{83}Kr and ^{129}Xe*, will focus on the polarization of the gas through spin-exchange optical pumping (SEOP). A method to generate high polarizations in gas mixtures with a high concentration of noble gas by optically pumping at low pressure (< 1 atm) will be detailed. This is an essential step towards the generation of highly polarized, highly concentrated gas mixtures containing ^{83}Kr.

Chapter 4, *Extraction and compression of low pressure hyperpolarized gases*, contains an extensive study of how one can return low-pressure optically pumped gas to atmospheric pressure without substantial losses in polarization, so that it can be used *in vivo*. Building on literature for hp ^{3}He gas compression [12-18], two methods to recompress both low-pressure ^{129}Xe and ^{83}Kr are

presented. These techniques are utilized to produce highly polarized hp gas at atmospheric pressure. The gas was applied to an *ex vivo* rat model and images of the pulmonary air spaces, for both ^{129}Xe and ^{83}Kr, were acquired. This included acquiring a surface-sensitive T_1 map using hp ^{83}Kr in an excised lung.

Understanding longitudinal and transverse relaxation rates is important for *in vivo* MRI with hyperpolarized noble gases: this is the focus of Chapter 5, *Exploring T_1 relaxation as a function of oxygen density on model surfaces*. One aspect of this is understanding relaxation in the presence of O_2 which has previously been used as a form of contrast for hp ^{3}He MRI [19-21] and is important to be able to quantify when mixing and storing breathable gas mixtures. While ^{129}Xe has already been studied extensively by Jameson *et al.* [22] using thermal samples and reexamined by Kraayvanger *et al.* in hyperpolarized systems [23] literature relating to O_2 dominated T_1 relaxation is scarce in regards to relaxation in the presence of a porous media or a lung [24]. So far T_1 relaxation as a result of O_2 concentration for ^{83}Kr has also received little attention [1, 25] and this relationship has not yet been characterized in the gas phase, which is vital to understand when mixing, storing and delivering the hp gas mixture during an *in vivo* study.

The relaxation behavior of ^{129}Xe in Xe-O_2 mixtures at physiologically relevant pressures in the gas phase will be re-examined and compared with the behavior in porous model systems and in excised rat lungs. The relaxation behavior of ^{83}Kr in Kr-O_2 mixtures will also be characterized. Two methodologies to mix O_2 and hp gas mixtures will be examined. One method, using low pressure gas mixing, will describe a way to mix large quantities of hp gas and O_2 without experiencing significant T_1 relaxation during the mixing process; which may be of interest for future Xe-O_2 mapping studies.

Chapter 6 will be dedicated to discussion of potential of hp gas imaging. Briefly detailed will be other work conducted to improve polarization, and some of the other applications of the techniques described in this thesis so far. How the work presented in this thesis aids the study of lungs through the use of hp gas imaging will be considered, and potential future steps to further this work will be debated.

1.2 MRI of the lungs

By 2002, just 29 years after its first inception, there were over 20 000 MRI scanners in use around the world; responsible for over 60 million examinations a year [26]. Applications for MRI have grown and scans of the lungs and respiratory system are becoming progressively more significant for clinical purposes. This is due in part to its advantages over other forms of imaging, namely Computed Tomography (CT), as MRI does not use ionizing radiation [27] and has superior soft tissue contrast [28]. The non-invasive nature of MRI is especially useful when used to scan children, or people who require frequent re-examination where it is desirable to limit radiation exposure as much as possible. It is believed that 0.4% of all cancers in the United States are due to CT scans taken in the past, with that figure likely to increase significantly (up

to 2%) in the near future [29]. As a non-invasive imaging modality, MRI does not expose patients to potentially harmful radiation.

While MRI of the lungs may be of significant use in cases where the employment of ionizing radiation must be avoided, it does come with some drawbacks. In a normal clinical MRI the protons of the highly abundant water molecules in the tissue are excited to generate signal. Unfortunately, the lungs have a very low tissue-to-volume ratio [4] leading to a low proton density and consequently yield a very weak MR signal intensity. The signal strength contributes to the resolution of the acquired image; so poor signal intensity is unfavourable. Fig. 1.2 shows a comparison from the literature of a proton scan of the lung cavity *in vivo* compared to an MRI of the same region using signal from hyperpolarized ^{3}He.

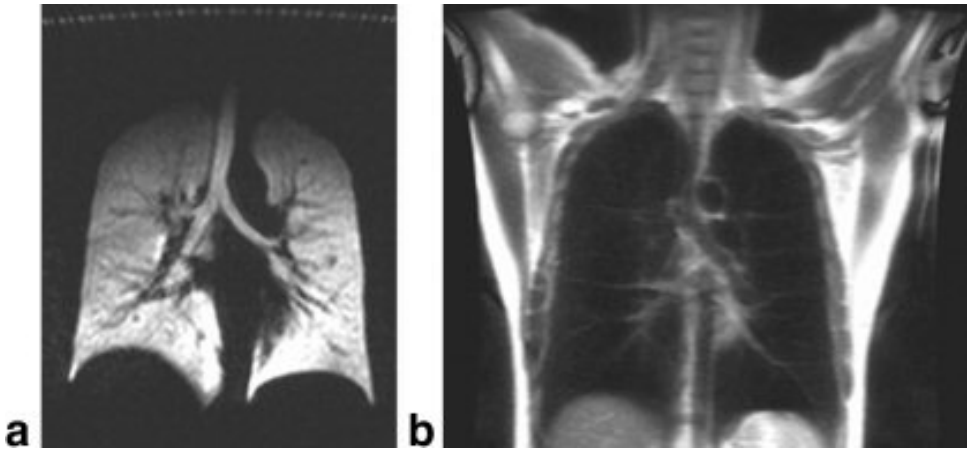

Fig. 1.2 *– Image taken from the literature* [30]. ***(a)*** *Hyperpolarized ^{3}He image of a human chest. Gas phase hp ^{3}He allows for a well-resolved image of the lung airspace.* ***(b)*** *Proton MRI of the same human chest. A low tissue-to-volume ratio in the lungs results in a low signal intensity in this portion of the image. Reproduced with permission from Wiley. © 2007 Wiley.*

Resolution can also deteriorate due to modulation artefacts created by pulsatile flow, cardiac, and respiratory motion [31]. Depending on the frequency of the modulation this will either display itself as a broad low-intensity streak, or an evident streak artefact; for low and high frequency modulation respectively [32].

The tissue-air interface also contributes to artefacts in lung MRI. The interface inflicts a magnetic susceptibility variation resulting in strong local field gradients that enforces a spatially dependent phase on the spins, thus leading to destructive interference during slice selection. Hence there will be partial cancellation of generated MR signals. Depending on selected slice thickness this can result in a significant signal-to-noise (SNR) degradation [33].

Techniques have been developed over the past few years to combat some of these issues. For example projection reconstruction (Fig 1.3b) coupled with ventilation and cardiac gating has been used to reduced motion artefacts and therefore improve SNRs [31]. However, the limitation imposed by proton density is still the primary restricting factor concerning the resolution of MRI in the lung.

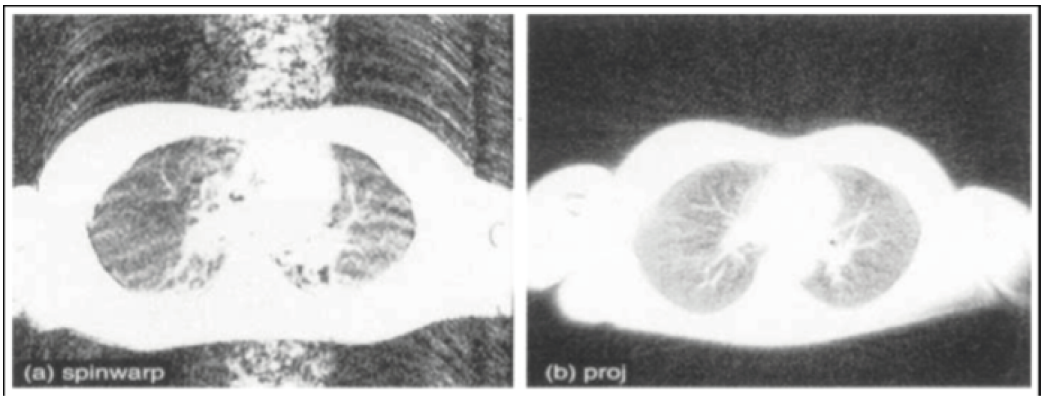

Fig. 1.3 *– Two lung images from literature[31]. (**a**) Image taken using conventional T_1-weighted multi-slice spin-wrap. Note the significant blurring due to motion artefacts. (**b**) Hadamard projection reconstruction multi-slice image. Motion artefacts are no longer present. Reproduced with permission from Wiley. © 1992 Wiley.*

Albert *et al.* first accomplished the use of hyperpolarized noble gas as a contrast agent to allow direct imaging of the airspace in mouse lungs [6]. Their paper detailed how they used hyperpolarized ^{129}Xe to produce gas-phase images of a higher resolution than those previous produced of the lung parenchyma using proton MRI.

Noble gases are an ideal contrast agent for the lungs as they are gaseous under standard temperature and pressure (STP), and they are chemically non-reactive. The tidal volume (VT) of the average human lung is about 0.5 L. In the human studies that followed Albert's initial experiment [34], patients are typically expected to inhale one-litre of ^{129}Xe, which constitutes 15 - 25% of the total lung capacity (TLC). This is a sufficient volume to obtain a good signal using hyperpolarized noble gas, assuming an adequate level of polarization. The polarizations of noble gas isotopes at thermal equilibrium do not produce a satisfactory signal at this volume, so hyperpolarization is crucial.

Another advantage of MRI is that functional images can be obtained. The field of functional Magnetic Resonance Imaging (fMRI) has received a lot of attention, especially regarding the brain [35-37]. The use of hyperpolarized gases can allow for the acquisition of functional information from the lungs. ^{3}He in particular has been used in a number of dynamic applications, as discussed later (**Section 1.3.1**).

1.3 Applications of hyperpolarized noble gases

Of the noble gas family there are five isotopes that are stable and spin-active (spin $I > 0$). These are listed in Table 1.1 along with their other notable attributes. Each isotope will be addressed individually in the following sections however it is important to highlight at this point that the isotopes fall into two broad categories; quadrupolar nuclei and non-quadrupolar nuclei (monopolar nuclei).

Isotope	Spin	Gyromagnetic ratio γ (10^{-7} rad/Ts)	Frequency ratio compared to protons γ/γ_{Proton}	Quadrupole moment (10^{28} m^2)
^{3}He	1/2	-20.38	.762	-
^{21}Ne	3/2	-2.11	.079	0.09
^{83}Kr	9/2	-1.03	.039	0.26
^{129}Xe	1/2	-7.44	.278	-
^{131}Xe	3/2	2.21	.083	0.12

Table 1.1 *- Table displaying all NMR active, stable, noble gas nuclei with important nuclear properties [38].*

1.3.1 Applications of ^{3}He

The potential application of ^{3}He (spin *I = 1/2*) for MRI of the lungs is well investigated [39-46] and at present ^{3}He is the most extensively studied gas for hyperpolarized MR lung imaging studies. It possesses a high gryomagnetic ratio γ = -20.38 x 10^{-7} rad/Ts allowing for a good SNR compared to the other useable noble gases (signal intensity would be approximately 76 % of that of a proton signal assuming all other conditions were the same, such as density, volume, and nuclear polarization). It also has no known toxic side effects making it completely non-invasive, which is preferable for *in vivo* use. ^{3}He is also highly insoluble allowing the gas to largely stay within the lung air space during a breath-hold experiment [39]. Another property of interest is that, due to its low mass and small size, ^{3}He is highly diffusive [47]. These three properties have prompted research into three areas of particular interest for lung studies; dynamic ventilation imaging, diffusion imaging, and the regional evaluation of oxygen concentration.

The regional evaluation of oxygen concentration exploits the fact that as an isotope with a high gyromagnetic ratio, the relaxation of ^{3}He is dominated by paramagnetic substances. Molecular oxygen has two unpaired electrons and, as a consequence, is paramagnetic. Increased densities of oxygen will therefore cause an increase in the rate of relaxation of the nearby ^{3}He. This relationship was originally characterised by Saam *et al.* [48] and has since been used to gain addition information about the lung.

One example shows regional intrapulmonary oxygen partial pressures [49] as determined by oxygen induced signal decay (due to T_1 relaxation) that is known to be linear [48]. From this, regional oxygen concentration can be measured as a function of time, allowing one to extrapolate the regional O_2

uptake. The uptake is a function of perfusion and therefore regional perfusion maps can be made. Lung pathology for both emphysema and chronic thromboembolic pulmonary hypertension are clearly identifiable from these regional perfusion maps [39]. As such regionally evaluating oxygen concentrations could yield potential clinical methods in diagnosing various pathological conditions [39, 42, 43].

Dynamic ventilation imaging can be used to measure apparent diffusion coefficients (ADC). Salerno *et al.* have produced images of the ADC in the lungs of volunteers and patients suffering from emphysema in the hopes of developing a means to accurately determine the severity and extent of the disease [43].

ADC is acquired using a number of images with gradient fields applied for different durations. Diffusion in a magnetic gradient causes signal attenuation [50]. This effect has been studied experimentally and is well understood [51, 52]. By comparing images taken with different applied gradient durations and strengths one is able to calculate regional ADC values [53, 54]. The ADC inversely corresponds to the freedom of movement available to the gas [45] and therefore the ADC enables one to determine the microstructure of the lung. This is useful when exploring COPD as in lungs where regions are obstructed, the motion of the ^{3}He will be more restricted, and hence the ADC will increase; as shown by Salerno *et al.* in humans [43].

Ventilation contrast is another method used in conjunction with ^{3}He MRI. This technique requires the intravenous injection of a superparamagnetic contrast agent. As discussed earlier paramagnetic materials are the principle contributor to T_1 relaxation in hyperpolarized ^{3}He, meaning that the presences of the contrast agent will display regions of significantly reduced signal. Depending on the contrast agent used, this can provide additional information in ventilation studies and allow for perfusion studies to be conducted [44].

It has been seen that ^{3}He can retain its polarization for a long time making it easier to store and transport than other hyperpolarized gases. Heil *et al.* have shown that in SEOP cells coated in certain metal films, T_1 times of up to 120 hours can be achieved [53]. Babcock *et al.* have observed polarisations of 81 % using SEOP [55].

As well as via SEOP, ^{3}He can also be produced using metastability-exchange optical pumping (MEOP) [56]. An RF discharge is used to move the electrons of ^{3}He atoms into the meta-stable 2^3S state. This state is optically pumped with circularly polarized light; the polarization is then transferred to the ^{3}He nuclear spin through spin exchange collisions. ^{3}He polarizations have been seen to exceed 70 % using MEOP [13].

Unfortunately, ^{3}He has an extremely low natural abundance on earth and in practice is acquired by tritium decay, a by-product of the nuclear weapons industry. The limited supply would make the widespread clinical use of the gas difficult. This issue was highlighted recently in a congressional testimony to the House of Representatives of the United States of America [57]; the United States being a major supplier of ^{3}He. The testimony admits that for some

imaging applications hp ^{129}Xe is a suitable substitute; however ^{129}Xe needs to be explored further for its usefulness in diffusion studies given the high diffusivity of the ^{3}He atom.

1.3.2 Applications of ^{129}Xe

Most noble gases (although not He) can be extracted from the atmosphere by cryogenically freezing air. The noble gases (approximately 1 % of air) are separated by taking advantage of the different boiling points of the constituent gases. This process is called fractional distillation and can be costly due to the small quantities of noble gases. Krypton and Xenon, which are the focus of this work, only constitute 1.14 and 0.087 ppmv respectively, and therefore other methods for their separation have been suggested [58].

Xenon has two NMR active isotopes, ^{129}Xe and ^{131}Xe, which have natural abundances of 26.4 % and 21.2 % respectively [59]. Enrichment is possible; at present isotopically enriched ^{129}Xe is about £150 per litre. This is significantly cheaper than ^{3}He, which has its cost set at $1000 [60] per litre (~£631 per litre as of late 2012) by the United States (it is $600 per litre for US federally funded medical research).

^{129}Xe can be polarized rapidly (as discussed in **Chapter 3**). High polarizations can be achieved, and polarizations of up to 84 % have been reported [61]. In a typically system ^{129}Xe hp gas mixture is frozen out of the hp gas mixture, allowing for pure hp ^{129}Xe gas to be used. Large quantities can also be produced as shown by the Hersman group [62]. T_1 times are typically of the order of 2-2.5 hours in a coated glass cell [63] however Gatzke *et al.* have shown that T_1 times in excess of 500 hours can be achieved using frozen mixtures including hp ^{129}Xe when cooled to 4.2 K [64].

Despite having an anaesthetic effect [65], ^{129}Xe has various properties that make it of interest as a potential lung probe. It is highly soluble in the blood as well as tissues [66]. ^{129}Xe, like ^{3}He, exhibits rapid T_1 relaxation in the presence of paramagnetic substances. This relationship between T_1 relaxation and O_2 concentration has been explored to some extent [22-24] and could possibly be utilized to produce maps of regional oxygen uptake similar to those created using ^{3}He.

^{129}Xe is also very sensitive to its environment exhibiting large chemical shifts depending on the chemical environment, due to shielding of the nucleus by its large electron cloud. Shifts over 7000 ppm have been observed and chemical shifts exceeding 200 ppm have been recorded in the lung [67-70].

These sizable shifts allow for individual peaks to be selected using selective RF pulses, exciting only a narrow portion of the frequencies in the spectrum: Fig. 1.4 shows three distinct peaks can be discerned. As a result ^{129}Xe has been of interest for dissolution-based studies, where ^{129}Xe in different phases (i.e. dissolved in the tissue, dissolved in blood) can be selectively excited giving information pertaining to transport mechanisms [67-71].

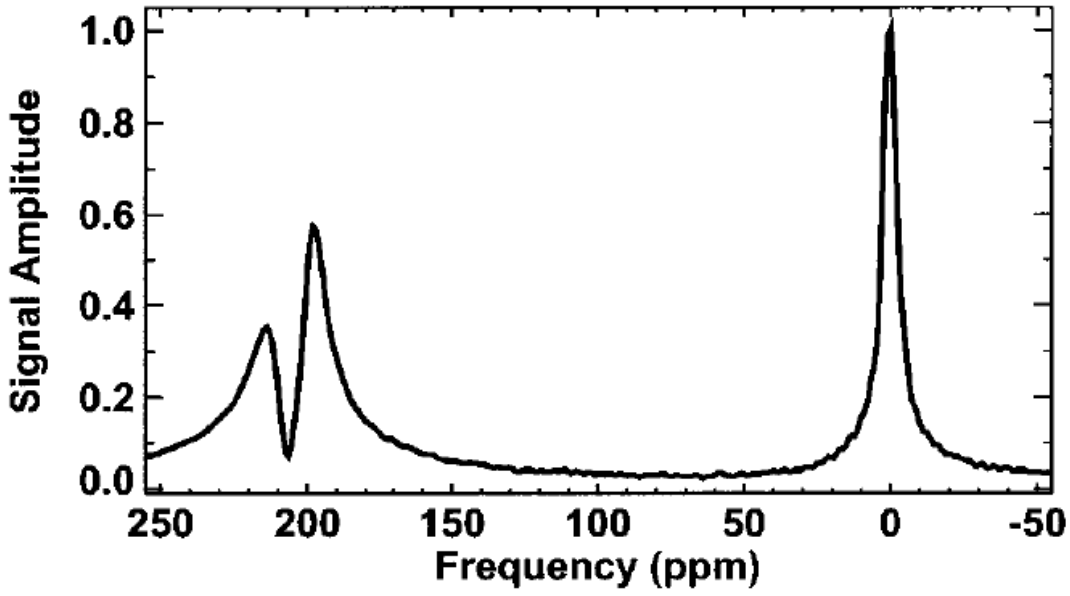

Fig. 1.4 *– NMR spectrum taken from the literature [70] showing hp ^{129}Xe inside of a canine lung. The spectrum was recorded chemical shift selectively, significantly reducing the signal obtained from the hp ^{129}Xe gas phase peak at 0 ppm. The next largest peak at ~ 200 ppm is hp ^{129}Xe dissolved in the lung parenchyma. The smallest peak at ~ 220 ppm is hp ^{129}Xe bound to haemoglobin. These well-defined chemical shifts can allow for NMR and imaging to be conducted on ^{129}Xe in a particular phase, allowing for the dynamics of the lung to be better investigated. Reproduced with permission from Wiley. © 2000 Wiley.*

1.3.2.1 ^{129}Xe dissolution studies

While studying diffusion dynamics in canine lungs, Ruppert *et al*. noted that the dissolved phase ^{129}Xe peak amplitudes relating to the lung parenchyma changed depending on the individual dog [71]. It was seen that the ratio of the tissue peak area over the gas-phase peak for the larger dog was notably bigger than for the smaller dog; while the blood peak area ratios were similar for both dogs. In both dogs the ^{129}Xe had the same amount of time to diffuse through the lung parenchyma, so in the larger dog more tissue must have been present. This implied that either the tissue compartments were smaller or the parenchyma walls were thicker (which was unlikely due to reasons discussed later). It was noted however that this could indicate possible pathology in one of the dogs.

Time constants for ^{129}Xe tissue and blood saturation were recorded by Ruppert *et al*. It was observed that there was a difference between the saturation rates; blood taking longer to saturate. The authors (Ruppert *et al.*) believed that this difference was the time taken for the ^{129}Xe to enter the blood cells through the lung parenchyma wall. The perfusion of ^{129}Xe may therefore provide a probe of the lung physiology. The authors go on to argue that, if the parenchyma walls were thicker (due to pathology) it would take ^{129}Xe longer to saturate it. Subsequently this would lead to more ^{129}Xe being in the tissue diffused phase upon saturation, resulting in a greater saturation amplitude in the tissue

diffused phase graph. The thickening of the parenchyma wall would not change the blood diffused-phase saturation amplitude presumably because the xenon could reach the blood at a timescale that was short enough compared to the transport due to the blood flow. For this to be a viable probe then the parameters for the lung while healthy would need to be known.

The diffusive and chemical shift properties of ^{129}Xe can also be exploited for imaging applications. Ruppert *et al*. explored the idea of using ^{129}Xe perfusion to study the effects that inflation and tissue density have on the ^{129}Xe gas tissue exchange rate and gas depolarisation in various animals [69]. Utilising xenon polarisation transfer contrast MRI (XTC MRI), as explained below, the authors were able to develop gas depolarisation maps.

Due to the presence of ^{129}Xe in the lungs for this study, selective RF pulses could be used to selectively depolarise ^{129}Xe in certain phases. The dissolved phase ^{129}Xe could therefore be completely depolarized using a series of these pulses. The depolarised ^{129}Xe exchanged with the hyperpolarized gas phase ^{129}Xe. This lowered the overall polarisation of the ^{129}Xe in the gas phase; therefore on subsequent image acquisitions of the gas phase ^{129}Xe, regions where more gas has been exchanged with the tissue would display a signal-intensity drop. From this it was possible to create a map showing changes in signal intensity, and consequently a map of depolarisation could be acquired. The areas of greater depolarisation displayed the regions of greater tissue volume [70]. This allowed the authors to detect regional tissue density changes with great precision.

Ruppert *et al.* speculated that this method could be further developed to acquire other information, such as localised surface-to-volume ratios [69, 70]. This could yield a number of clinical applications, since it would allow for the non-invasive detection of various pathological conditions; especially those affecting smaller scale structures, such as pulmonary emphysema. The T_1 relaxation of ^{83}Kr has been shown to be sensitive to surface-to-volume ratios [72] and may therefore also prove to be useful for studying pathology of this type.

The work of Ruppert *et al.* also showed that compression of the lung tissue caused an increase in the ^{129}Xe gas-tissue exchange rate. This was due to an increase in the surface-to-volume ratio of the lung [69]. A greater surface area allowed more ^{129}Xe to diffuse into the tissue at any given time. The authors suggest that this could be used as a means to calculate lung capacity in healthy patients, and detect pathology in those where the lung capacity is already accurately known.

Driehuys *et al.* explored gas exchange between the capillary system and alveoli [68]. In this paper a method named Xenon Alveolar Capillary Transfer Imaging (XACT) is proposed. In contrast to the XTC method where the gas phase was monitored, the dissolved-tissue or the blood phase dissolved xenon (as shown in Fig. 1.4) was detected after receiving a selective RF excitation. Phase evolution was allowed so that the phase of the spins were offset by a 90° between the blood and tissue dissolved-phase peaks. The scanner receiver window was opened and sets of data for both of the excited regions spectrum were collected. Capillary-alveoli transfer was taken as the relationship of the ^{129}Xe dissolved in the blood compared to ^{129}Xe in the dissolved in the lung

tissue. The authors (Driehuys *et al.*) explain that the primary advantage of this method over both XTC and ADC, which can indirectly measure gas exchange, was that XACT receives its sensitivity from small-scale structural changes, and could be useful in determining thickening of the blood-tissue interface.

Advancing their previous work to develop regional evaluation in the lung in 2009, Driehuys *et al.* investigated pulmonary perfusion and gas exchange in rats by the intravenous administration of hp ^{129}Xe saturated saline solution and compared the resulting images with conventional inhalation images [67]. The authors managed to acquire data with this technique that provided images that were entirely dependent on pulmonary perfusion (the ^{129}Xe was delivered solely by the arterial blood stream). In contrast to other methods the signal generated was known to be entirely perfusion based, as the gas phase signal could be isolated using a selective pulse, proving the presence of gas-phase ^{129}Xe. This should make the method more sensitive to diseases affecting gas exchange (such as COPD) as capillaries are affected before any of the major blood vessels.

Other diffusion-based studies include work by Abdeen *et al.* have so far shown that the diffusion capacity of ^{129}Xe in red blood cells does not provide a useful indicator for lung inflammation due to fungal spores [73]. However the work did show changes in the lung parenchyma perfusion capacity in the presence of pathology, leading Driehuys *et al.* to suggest that this may prove to be a useful probe with further research. This is one of many studies [73, 74] to explore diffusion capacity and perfusion as possible probes for pathology; in particular for inflammatory injury.

1.3.2.2 ^{129}Xe as a biosensor

There has also been interest in using ^{129}Xe as a biosensor [75-77]; first suggested by Spence *et al.* at Berkeley [78]. In their paper they dissolved ^{129}Xe into a solution with a synthesised molecule based on cryptophane-A. The molecule essentially had three parts, a cage to encapsulate the ^{129}Xe, a ligand that would bind with the desired target (in this case the target was a protein), and a tether between the two.

The theory was that the cage would bind with the ^{129}Xe, and the sensor would bind with the target protein. Without the presence of the target protein this should cause a chemical shift in the ^{129}Xe spectrum, which was shown. The peak associated to the cryptophane-A molecule bound with ^{129}Xe had a slight splitting, the smaller peak referred to ^{129}Xe bound to cryptophane-A molecules that lacked the sensor and tether components.

When this was repeated in the presence of the protein (avidin) a second sub-peak emerged and the signal intensity of the main cryptophane-A molecule bound with ^{129}Xe peak decreased (Fig. 1.5). The new peak represented cryptophane-A molecules with ^{129}Xe bound to the proteins. The authors also explored the chemical shift present using a cryptophane-E cage.

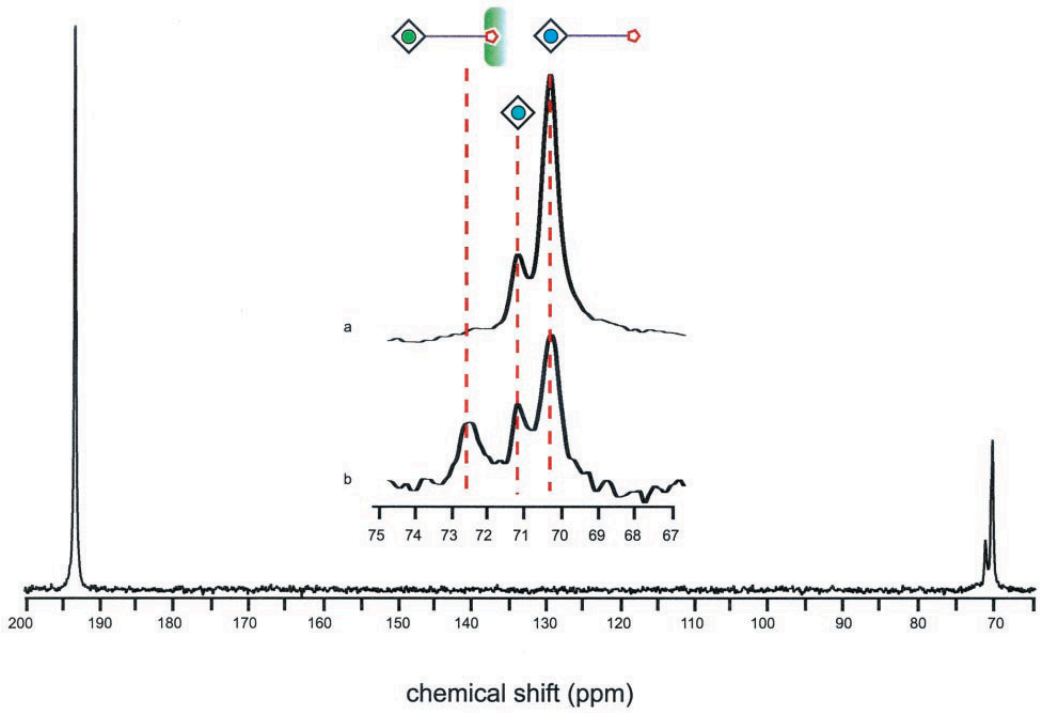

Fig. 1.5 *– Figure taken from literature [78].* ^{129}*Xe spectra for a functionalized biomarker; chemical shifts are referenced to gaseous* ^{129}*Xe. The spectrum is shown in the absence of the target protein (i.e. avidin). The peak at 70 ppm shows Xe encapsulated by cryptophane-A. The peak at 193 ppm is* ^{129}*Xe in water. (**a**) An expanded view of the 70 ppm line (with splitting) for Xe encapsulated by cryptophane-A in the absence of the protein. The largest peak is the functionalized Xe, where the smaller peak corresponds to Xe encapsulated by cryptophane-A without the ligand and the tether (i.e. non-functionalized) (**b**) Xe encapsulated by cryptophane-A in the presence of the protein; the third peak corresponds to this binding between functionalized Xe and the protein. As one might expect, the peak corresponding to functionalized Xe has dropped. Used in accordance with the PNAS reprint policy. © 2001 National Academy of Sciences, USA.*

It was the belief of Spence *et al.* that the chemical shift caused by the protein attaching to the cryptophane-A molecule was due to the cage deforming. This may subsequently deform the ^{129}Xe electron cloud, hence causing a chemical shift. Ruiz *et al.* later showed the induced chirality of the ^{129}Xe [79], which combined with theoretical work by Sears *et al.* [80] seemed to agree with this initial conclusion.

Spence *et al.* believed that one of the major advantages of this technique is that it could potentially be performed *in vitro* or *in vivo* by taking advantage of MRI's ability to spatially encode the location of the ^{129}Xe. Toxins are one of the possible targets suggested; which could prove to be a useful probe of pathology for the lung in specific cases.

1.3.2.3 ^{129}Xe for clinical studies

The first human chest imaging and spectroscopy using hp ^{129}Xe was reported by Mugler *et al.* and showed that using ^{129}Xe as a contrast agent in the human lung was feasible [34]. Despite having undesirable anaesthetic properties the anaesthetic threshold of xenon is 70% of the inhaled gas mixture, allowing for relatively large volumes of ^{129}Xe to be inhaled. Irrespective of this the authors reported that after the inhalation of approximately 500 cm^3 of gas during one experiment a volunteer experienced numbness in their legs and nausea, both side effects common to anaesthesia [34]. Other slight side effects included euphoria and a floral aroma.

In this preliminary study Mugler *et al.* obtained gas phase ^{129}Xe chest images that correspond well to the proton void space images also taken. It was reported that a voxel volume of 0.9 cm^3 could be achieved. However, no dissolved phase images were apparent. It was likely due to insufficient dissolved phase signal.

Despite not acquiring any dissolved phase images, later work by Mugler *et al*. did acquire dissolved phase ^{129}Xe images in human subjects [81] (this was first shown by Cleveland *et al.* [82]). This work also explored humans with both asthma and mild COPD. Spatial variations in the gas distribution as well as differences between healthy lungs and those with pathology allowed the conditions to be characterized.

1.3.3 Applications of ^{131}Xe

^{131}Xe has a nuclear electric quadrupole moment. As with all spin $I > 1/2$ nuclei ^{131}Xe is susceptible to electric field gradients (EFGs). When a ^{131}Xe atom collides with a surface, its electron cloud distorts generating an EFG. This EFG couples to the nucleus and causes quadrupolar driven T_1 relaxation. This is the dominant form of relaxation for ^{131}Xe when not in the presence of high concentrations of paramagnetic substances [74]. This effect can be exploited making ^{131}Xe and other quadrupolar nuclei (such as ^{21}Ne (spin $I = 3/2$) and ^{83}Kr (spin $I = 9/2$)) sensitive surface probes.

^{131}Xe can be polarised rapidly. Typical T_1 times are around twenty-two seconds under atmospheric conditions. This decreases inversely with pressure due to the EFGs created by the electron clouds of other xenon atoms [83]. *In vivo* T_1 times would be significantly less making the use of ^{131}Xe impractical as a surface probe in lung studies. However, ^{131}Xe may be able to provide information on the upper airways such as the trachea and bronchi, not completely ruling it out as a potential tool for respiratory diagnostics.

^{131}Xe can also provide useful information that can aid in the development of other quadrupolar nuclei, namely ^{83}Kr. ^{131}Xe is easier to study in some respects than ^{83}Kr as it has a simpler spin system allowing for less complex theoretical models; which subsequently could be used as a first order approximation for ^{83}Kr. Also, the volume of literature on ^{129}Xe allows for comparative studies of two nuclei of the same element.

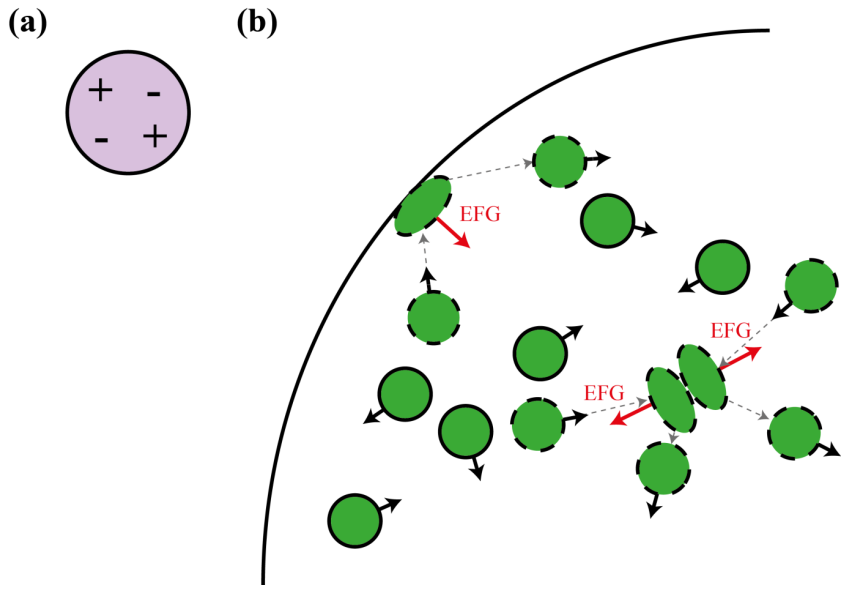

Fig. 1.6 *– **(a)** Charge distribution in the nucleus for ^{131}Xe, this would also apply for other quadrupolar nuclei. Charge distribution is not homogenous over the entirety of the nucleus; instead different charge polarities are restricted to regions of the nucleus. When influenced by an electric field gradient the nucleus will be affected differently depending on the field's properties. **(b)** Electron cloud of ^{131}Xe atom deforming during surface collision. The black arrows show the random motion of the atoms. Deformation caused by collisions will depend on the properties of the surface in addition to properties of the noble gas (such as velocity). This deformation means that the charge distribution of the electron cloud is no longer uniform creating an electric field gradient (EFG), represented by the red arrows. Under most conditions the presence of an EFG will be the dominant factor affecting quadrupolar nuclei T_1 relaxation. Therefore T_1 relaxation will depend upon the surface properties of a sample, making quadrupolar nuclei a useful surface probe.*

1.3.4 Applications of ^{21}Ne

^{21}Ne has been successfully optically pumped using SEOP [84]. ^{21}Ne is not currently being studied by any research groups for use as a MRI contrast agent to this author's knowledge. It has a low natural abundance making it difficult to extract, and it is not susceptible to large chemical shifts. One property of interest is that it has a spin $I = 3/2$ giving it nuclear electric quadrupole moment. However, the quadrupolar moment of ^{21}Ne is very small (less than the quadrupole moments of both ^{131}Xe and ^{83}Kr [38]) meaning that it has a lower sensitivity and therefore is less likely to become a viable lung probe.

^{21}Ne has been explored for other applications. The Romalis group have investigated creating a co-magnetometer using hp ^{21}Ne as opposed to ^{3}He as is commonly used. The sensitivity of the co-magnetometer is inversely proportional to the gryomagnetic ratio so the use of hp ^{21}Ne could vastly improve sensitivity over ^{3}He. Polarizations of ~ 8% are reported [85]. With this in mind it is difficult to see how ^{21}Ne has an advantage over its counterpart

^{83}Kr that has both a lower gryomagnetic ratio and greater reported polarizations (^{83}Kr polarizations are discussed in detail in **Chapter 3**).

Without further studies the possible future applications of ^{21}Ne cannot be determined.

1.3.5 Applications of ^{83}Kr

^{83}Kr is a spin *I = 9/2* isotope giving it a nuclear electric quadrupole moment. The gas can be polarized rapidly (**Chapter 3**). Under atmospheric conditions ^{83}Kr has a T_1 time of several minutes depending on the properties of surface present [72], this has been shown to reduce between 0.7 – 3.7 s in rat lungs [86]. ^{83}Kr has a significantly lower gyromagnetic ratio than ^{3}He or ^{129}Xe. This leads to a lower signal strength in NMR applications, however also means that the T_1 of ^{83}Kr is fairly insensitive to the presence of paramagnetic substances, such as O_2 [25]. Therefore T_1 weighted images that are sensitive to the surface of lungs in pre-clinical and clinical studies would not be affected by the presence of O_2 in the (breathing) mixture.

Owing to its complex quadrupolar spin system, ^{83}Kr surface absorption processes affect both T_1 relaxation and line width, providing surface information that is far more sensitive than shifts and line width changes associated to ^{129}Xe shielding. Like ^{129}Xe, ^{83}Kr has a large electron cloud meaning that it will also experience chemical shifts depending on the chemistry of its environment. However, the shifts experienced by ^{83}Kr are approximately three times smaller than those in ^{129}Xe [11] and the quadrupolar T_1 relaxation is a more valuable parameter for pulmonary MRI.

Using samples containing various types of glass bead Stupic *et al.* studied the T_1 relaxation of ^{83}Kr, showing how various factors could affect the relaxation rate [72]. Hyperpolarized (hp) gas was created using a SEOP apparatus similar to the one described later (**Chapter 3**, Fig. 3.4). Stupic's work was the first to attempt to separate Rb vapour from the hp ^{83}Kr, a task that was achieved by shuttling the gas through an air-cooled filter; an important step before potential clinical studies.

Four sizes of degassed glass beads with diameters of 0.1 - 2.5 mm were used in this study. A portion of the beads were left untreated while others were either washed with ammonium hydroxide or given a silicon coating. The beads were tightly packed into detection cells creating varying sizes of macroscopic pores, similar to the airways of the lung, which the hp ^{83}Kr was transferred into (Fig 1.1). The surface-to-volume ratio was therefore inversely proportional to the radius of the pores. The T_1 times in the samples were then recorded by taking a number of medium flip angles pulses (12°) and calculated using a non-linear least square fit.

The results showed that a greater surface-to-volume ratio resulted in shorter T_1 times due to the dominance of the quadrupolar relaxation on the surface. Further to this, the longest T_1 times were seen in detection cells with no beads in them. One unexpected result was that if the only source of observed

relaxation was surface-to-volume dependant then relaxation times should have been linearly proportional to the radii of the pores, this was not what was seen with the trend deviating more with increasing bead diameters. It was assumed that the beads were ideally packed giving uniform pour sizes; Stupic *et al.* suggested that this might not be the case for the larger beads. Further study would be required to fully quantify this effect.

The study also showed that ^{83}Kr relaxes more quickly when absorbed by polar surfaces (i.e. hydrophobic surfaces) due to increased strength of the van der Waal interactions. Stupic *et al.* proposed that this could subsequently increase properties such as the absorption time of the ^{83}Kr, or the magnitude of the quadrupolar interaction, decreasing the T_1 time. A previous study had shown spatially resolved T_1 contrast using beads that had been treated with a siliconizing agent, and beads that had not been, as shown in Fig. 1.1 [1].

This method was also tested in various polymers with non-ideal pore sizes. An observable shift (-1.73 ppm) for the material phase ^{83}Kr was seen. T_1 times were recorded and changes in relaxation based on surface chemistry and surface-to-volume ratio similar to those seen with glass bead samples were observed.

Sensitivity to surface temperature has also been shown. Cleveland *et al.* found that increasing the temperature of hp ^{83}Kr increases the T_1 relaxation in a Pyrex® glass cell similar to the SEOP cell [87]. The authors suggest that while an increased temperature would improve the Kr-Rb exchange rate due to increased Rb concentration, it should also reduce the self-relaxation of the ^{83}Kr through quadrupolar interactions; as at a higher temperature the ^{83}Kr would have a shorter contact time with other atoms and the cell walls.

A proof-of-principle study has been conducted in excised rat lungs by Cleveland *et al.* [86]. This work concentrated on NMR spectroscopy of the hp ^{83}Kr in the lung, comparing acquired signals to those acquired from a balloon of the same volume. The intensities were compared to give a qualitative assessment of whether hp ^{83}Kr would stay polarized for a sufficient amount of time to enter the alveoli, which this work shows that it does. In addition the authors explored the T_1 relaxation in the lungs and obtained an image of the lungs (2.3 x 2.3 mm resolution). This built on previous imaging work [1] showing the potential of T_1 weighted contrast using ^{83}Kr in the lung.

Further studies in excised rat lungs by Stupic *et al.* expanded on this work [25]. The affect of various ventilation schemes and volumes on the ^{83}Kr T_1 time were investigated. Different ventilation schemes where shown to have an effect on T_1 times, however different volumes were not. This was an interesting result as the surface-to-volume ratio should have decreased with an increased inhalation volume and subsequently T_1 should have increased. The author suggested that this was due to the mechanics of lung inhalation and may possibly suggest that the inflation of alveoli was rapid, with regions closed-off until enough gas was inhaled. This would mean that the surface-to-volume was consistent at different inhalation volumes. The study also looked at Kr-O_2 mixtures within the excised lung. As previously thought moderate concentrations of O_2 (up to 40 %) had a negligible effect on the Kr T_1 time when in the presence of a large surface (as is the case in the rat lung).

1.4 References

[1] G.E. Pavlovskaya, Z.I. Cleveland, K.F. Stupic, T. Meersmann, Hyperpolarized Krypton-83 as a New Contrast Agent for Magnetic Resonance Imaging, Proceedings of the National Academy of Sciences of the United States of America, 102 (2005) 18275-18279.
[2] P.C. Lauterbur, Image formation by induced local interactions: examples employing nuclear magnetic resonance. , Nature, 242 (1973) 2.
[3] A.N. Garroway, P.K. Grannell, P. Mansfield, Image formation in NMR by a selective irradiative process, Journal of Physics C: Solid State Physics, 7 (1974) L457.
[4] S.J. Gould, P.G. Isaacson, Bronchus-associated lymphoid tissue (BALT) in human fetal and infant lung, The Journal of Pathology, 169 (1993) 229-234.
[5] W.E.H.Y.T.M. Jemal A, TRends in the leading causes of death in the united states, 1970-2002, JAMA: The Journal of the American Medical Association, 294 (2005) 1255-1259.
[6] M.S. Albert, G.D. Cates, B. Driehuys, W. Happer, B. Saam, C.S. Springer, A. Wishnia, Biological Magnetic Resonance Imaging Using Laser Polarized Xe-129, Nature, 370 (1994) 199-201.
[7] D.M. Lilburn, G.E. Pavlovskaya, T. Meersmann, Perspectives of Hyperpolarized Noble Gas MRI beyond ^{3}He, Journal of Magnetic Resonance, (2013).
[8] S. Fain, M.L. Schiebler, D.G. McCormack, G. Parraga, Imaging of lung function using hyperpolarized helium,Äê3 magnetic resonance imaging: Review of current and emerging translational methods and applications, Journal of Magnetic Resonance Imaging, 32 (2010) 1398-1408.
[9] H. Middleton, R.D. Black, B. Saam, G.D. Cates, G.P. Cofer, R. Guenther, W. Happer, L.W. Hedlund, G.A. Johnson, K. Juvan, J. Swartz, Mr-Imaging with Hyperpolarized He-3 Gas, Magnetic Resonance in Medicine, 33 (1995) 271-275.
[10] Z.I. Cleveland, G.E. Pavlovskaya, K.F. Stupic, J.B. Wooten, J.E. Repine, T. Meersmann, Detection of Tobacco Smoke Deposition by Hyperpolarized Krypton-83 MRI, Magnetic Resonance Imaging, 26 (2008) 270-278.
[11] Z.I. Cleveland, T. Meersmann, Studying porous materials with krypton-83 NMR spectroscopy, Magnetic Resonance in Chemistry, 45 (2007) S12-S23
[12] G. Eckert, W. Heil, M. Meyerhoff, E.W. Otten, R. Surkau, M. Werner, M. Leduc, P.J. Nacher, L.D. Schearer, A Dense Polarized He-3 Target Based on Compression of Optically Pumped Gas, Nuclear Instruments & Methods in Physics Research Section a-Accelerators Spectrometers Detectors and Associated Equipment, 320 (1992) 53-65.
[13] W. Heil, K. Andersen, D. Hofmann, H. Humblot, J. Kulda, E. Lelievre-Berna, O. Schärpf, F. Tasset, ^{3}He neutron spin filter at ILL, Physica B: Condensed Matter, 241-243 (1997) 56-63.
[14] D.S. Hussey, D.R. Rich, A.S. Belov, X. Tong, H. Yang, C. Bailey, C.D. Keith, J. Hartfield, G.D.R. Hall, T.C. Black, W.M. Snow, T.R. Gentile, W.C. Chen, G.L. Jones, E. Wildman, Polarized ^{3}He gas compression system using metastability-exchange optical pumping, Review of Scientific Instruments, 76 (2005) 053503-053512.
[15] W.M. Snow, Neutron Polarizers Based on Polarized 3He, in, 2005, pp. Medium: ED.

[16] T.R. Gentile, G.L. Jones, A.K. Thompson, R.R. Rizi, D.A. Roberts, I.E. Dimitrov, R. Reddy, D.A. Lipson, W. Gefter, M.D. Schnall, J.S. Leigh, Demonstration of a compact compressor for application of metastability-exchange optical pumping of He-3 to human lung imaging, Magnetic Resonance in Medicine, 43 (2000) 290-294.
[17] T.R. Gentile, D.R. Rich, A.K. Thompson, W.M. Snow, G.L. Jones, Compressing spin-polarized [3]He with a modified diaphragm pump, National Institute of Standards and Technology, Gaithersburg, MD, ETATS-UNIS, 2001.
[18] R.S. Timsit, J.M. Daniels, E.I. Dennig, A.K.C. Kiang, A.D. May, An Experiment to Compress Polarized 3He Gas, Canadian Journal of Physics, 49 (1971) 508-516.
[19] B. Eberle, N. Weiler, K. Markstaller, H.U. Kauczor, A. Deninger, M. Ebert, T. Grossmann, W. Heil, L.O. Lauer, T.P.L. Roberts, W.G. Schreiber, R. Surkau, W.F. Dick, E.W. Otten, M. Thelen, Analysis of intrapulmonary O-2 concentration by NIR imaging of inhaled hyperpolarized helium-3, Journal of Applied Physiology, 87 (1999) 2043-2052.
[20] M.C. Fischer, S. Kadlecek, J.S. Yu, M. Ishii, K. Emami, V. Vahdat, D.A. Lipson, R.R. Rizi, Measurements of regional alveolar oxygen pressure using hyperpolarized He-3 MRI, Academic Radiology, 12 (2005) 1430-1439.
[21] K. Cieslar, V. Stupar, E. Canet-Soulas, S. Gaillard, Y. Cremillieux, Alveolar oxygen partial pressure and oxygen depletion rate mapping in rats using He-3 ventilation imaging, Magnetic Resonance in Medicine, 57 (2007) 423-430.
[22] C.J. Jameson, A.K. Jameson, J.K. Hwang, Nuclear-Spin Relaxation by Intermolecular Magnetic Dipole Coupling in the Gas-Phase - Xe-129 in Oxygen, Journal of Chemical Physics, 89 (1988) 4074-4081.
[23] C.P.B. R.J. Kraayvanger, W. Dominguez-Viqueira, J. Parra-Robles, M. Foz, W.W. Lam, G.E. Santyr Measurement of alveolar oxygen partial pressure in the rat lung using Carr-Purcell-Meiboom-Gill spin-spin relaxation times of hyperpolarized 3He and 129Xe at 74 mT, Magnetic Resonance in Medicine, 64 (2010) 1484-1492.
[24] P.L. V. Pasquier, A. Delville, 129Xe NMR as a probe of gas diffusion and relaxation in disordered porous media: an application to Vycor, The Journal of Physical Chemistry, 100 (1996) 10249-10256.
[25] K.F. Stupic, N.D. Elkins, G.E. Pavlovskaya, J.E. Repine, T. Meersmann, Effects of pulmonary inhalation on hyperpolarized krypton-83 magnetic resonance T-1 relaxation, Physics in Medicine and Biology, 56 (2011) 3731-3748.
[26] Curiosity-Driven Research MRI Magnetic Resonance Imaging, in, Insititute of Physics.
[27] J. Biederer, H.-U. Kauczor, General Requirements of MRI of the Lung and Suggested Standard Protocol
MRI of the Lung, in, Springer Berlin Heidelberg, 2009, pp. 3-16.
[28] O. Dietrich, S.O. Schoenberg, M.F. Reiser, General Advantages of Parallel Imaging
Parallel Imaging in Clinical MR Applications, in, Springer Berlin Heidelberg, 2007, pp. 173-176.

[29] D.J. Brenner, E.J. Hall, Current concepts - Computed tomography - An increasing source of radiation exposure, New England Journal of Medicine, 357 (2007) 2277-2284.
[30] S.B. Fain, F.R. Korosec, J.H. Holmes, R. O'Halloran, R.L. Sorkness, T.M. Grist, Functional lung imaging using hyperpolarized gas MRI, Journal of Magnetic Resonance Imaging, 25 (2007) 910-923.
[31] G.H. Glover, J.M. Pauly, Projection Reconstruction Techniques for Reduction of Motion Effects in MRI, Magnetic Resonance in Medicine, 28 (1992) 275-289.
[32] M.A. Schmidt, G.-Z. Yang, P.D. Gatehouse, D.N. Firmin, FID-based lung MRI at 0.5 T: Theoretical considerations and practical implications, Magnetic Resonance in Medicine, 39 (1998) 666-672.
[33] S. Su, J.K. Saunders, I.C.P. Smith, Resolving Anatomical Details in Lung Parenchyma: Theory and Experiment for a Structurally and Magnetically Inhomogeneous Lung Imaging Model, Magnetic Resonance in Medicine, 33 (1995) 760-765.
[34] J.P. Mugler, B. Driehuys, J.R. Brookeman, G.D. Cates, S.S. Berr, R.G. Bryant, T.M. Daniel, E.E. deLange, J.H. Downs, C.J. Erickson, W. Happer, D.P. Hinton, N.F. Kassel, T. Maier, C.D. Phillips, B.T. Saam, K.L. Sauer, M.E. Wagshul, MR imaging and spectroscopy using hyperpolarized Xe-129 gas: Preliminary human results, Magnetic Resonance in Medicine, 37 (1997) 809-815.
[35] N.K. Logothetis, What we can do and what we cannot do with fMRI, Nature, 453 (2008) 869-878.
[36] S.A. Engel, D.E. Rumelhart, B.A. Wandell, A.T. Lee, G.H. Glover, E.-J. Chichilnisky, M.N. Shadlen, fMRI of human visual cortex, Nature, 369 (1994) 525-525.
[37] C. Kaufmann, R. Wehrle, T.C. Wetter, F. Holsboer, D.P. Auer, T. Pollm√§cher, M. Czisch, Brain activation and hypothalamic functional connectivity during human non-rapid eye movement sleep: an EEG/fMRI study, Brain, 129 (2006) 655-667.
[38] R.K. Harris, E.D. Becker, S.M. Cabral de Menezes, R. Goodfellow, P. Granger, NMR nomenclature. Nuclear spin properties and conventions for chemical shifts (IUPAC recommendations 2001), Pure and Applied Chemistry, 73 (2001) 1795-1818.
[39] E.J.R. van Beek, J.M. Wild, H.U. Kauczor, W. Schreiber, J.P. Mugler, E.E. de Lange, Functional MRI of the lung using hyperpolarized 3-helium gas, Journal of Magnetic Resonance Imaging, 20 (2004) 540-554.
[40] H.E. Moller, X.J. Chen, B. Saam, K.D. Hagspiel, G.A. Johnson, T.A. Altes, E.E. de Lange, H.U. Kauczor, MRI of the lungs using hyperpolarized noble gases, Magnetic Resonance in Medicine, 47 (2002) 1029-1051.
[41] R.E. Jacob, S.W. Morgan, B. Saam, He-3 spin exchange cells for magnetic resonance imaging, Journal of Applied Physics, 92 (2002) 1588-1597.
[42] J.R. Mayo, M.E. Hayden, Hyperpolarized Helium 3 Diffusion Imaging of the Lung1, Radiology, 222 (2002) 8-11.
[43] M. Salerno, E.E. de Lange, T.A. Altes, J.D. Truwit, J.R. Brookeman, J.P. Mugler, Emphysema: Hyperpolarized Helium 3 Diffusion MR Imaging of the Lungs Compared with Spirometric Indexes —Initial Experience 1., Radiology, 222 (2002) 252-260.

[44] V. Stupar, Y. Berthezène, E. Canet, H. Tournier, D. Dupuich, Y. Crémillieux, Helium3 Polarization Using Spin Exchange Technique: Application to Simultaneous Pulmonary Ventilation/Perfusion Imaging in Small Animals, Investigative Radiology, 38 (2003) 334-340.
[45] J.P. Mugler III, C. Wang, G.W. Miller, G.D. Cates Jr, J.F. Mata, J.R. Brookeman, E.E. de Lange, T.A. Altes, Helium-3 Diffusion MR Imaging of the Human Lung Over Multiple Time Scales, Academic Radiology, 15 (2008) 693-701.
[46] A.K. Venkatesh, A.X. Zhang, J. Mansour, L. Kubatina, C.-H. Oh, G. Blasche, M. Selim Ünlü, D. Balamore, F.A. Jolesz, B.B. Goldberg, M.S. Albert, MRI of the lung gas-space at very low-field using hyperpolarized noble gases, Magnetic Resonance Imaging, 21 (2003) 773-776.
[47] B.M. Goodson, Nuclear magnetic resonance of laser-polarized noble gases in molecules, materials, and organisms, Journal of Magnetic Resonance, 155 (2002) 157-216.
[48] B. Saam, W. Happer, H. Middleton, Nuclear-Relaxation of He-3 in the Presence of O-2, Physical Review A, 52 (1995) 862-865.
[49] A.J. Deninger, B. Eberle, M. Ebert, T. Grossmann, W. Heil, H.U. Kauczor, L. Lauer, K. Markstaller, E. Otten, J. Schmiedeskamp, W. Schreiber, R. Surkau, M. Thelen, N. Weiler, Quantification of Regional Intrapulmonary Oxygen Partial Pressure Evolution during Apnea by 3He MRI, Journal of Magnetic Resonance, 141 (1999) 207-216.
[50] R.L. Gamblin, T.R. Carver, Polarization and Relaxation Processes in He^{3} Gas, Physical Review, 138 (1965) A946-A960.
[51] W. Zheng, Z.I. Cleveland, H.E. M√∂ller, B. Driehuys, Gradient-induced longitudinal relaxation of hyperpolarized noble gases in the fringe fields of superconducting magnets used for magnetic resonance, Journal of Magnetic Resonance, 208 284-290.
[52] L.D. Schearer, G.K. Walters, Nuclear Spin-Lattice Relaxation in Presence of Magnetic-Field Gradients, Physical Review, 139 (1965) 1398-1402.
[53] W. Heil, H. Humblot, E. Otten, M. Schafer, R. Sarkau, M.l. Leduc, Very long nuclear relaxation times of spin polarized helium 3 in metal coated cells, Physics Letters A, 201 (1995) 337-343.
[54] E. Brunner, Enhancement of surface and biological magnetic resonance using laser-polarized noble gases, Concepts in Magnetic Resonance, 11 (1999) 313-335.
[55] E. Babcock, B. Chann, T.G. Walker, W.C. Chen, T.R. Gentile, Limits to the polarization for spin-exchange optical pumping of He-3, Physical Review Letters, 96 (2006) 083003.
[56] F.D. Colegrove, L.D. Schearer, G.K. Walters, Polarization of He^{3} Gas by Optical Pumping, Physical Review, 132 (1963) 2561-2572.
[57] J.C. Woods, Congressional Hearing: "Caught by Surprise: Causes and Consequences of the Helium-3 Supply Crisis", Testimony before the House Committee on Science and Technology, Subcommittee on Investigations and Oversight, (2010).
[58] S.J. Cook, J.L. Griffths, Recovery of Krypton and Xenon, in: E.P. Register (Ed.), Air Products And Chemical, Inc., 2003.
[59] R.L. Streever, H.Y. Carr, Nuclear Magnetic Resonance of Xe129 in Natural Xenon, Physical Review, 121 (1961) 20-&.

[60] D. Kramer, For some, helium-3 supply picture is brightening, Physics Today, 64 20-23.
[61] G. Schrank, Z. Ma, A. Schoeck, B. Saam, Characterization of a low-pressure high-capacity 129Xe flow-through polarizer, Physical Review A, 80 (2009) 063424.
[62] I.C. Ruset, S. Ketel, F.W. Hersman, Optical pumping system design for large production of hyperpolarized Xe-129, Physical Review Letters, 96 (2006) 053002.
[63] M.E. Wagshul, T.M. Button, H.F. Li, Z. Liang, C.S. Springer, K. Zhong, A. Wishnia, In vivo MR imaging and spectroscopy using hyperpolarized 129Xe, Magnetic Resonance in Medicine, 36 (1996) 183-191.
[64] M. Gatzke, G.D. Cates, B. Driehuys, D. Fox, W. Happer, B. Saam, Extraordinarily slow nuclear spin relaxation in frozen laser-polarized ^{129}Xe, Physical Review Letters, 70 (1993) 690-693.
[65] S.C. Cullen, E.G. Gross, The Anesthetic Properties of Xenon in Animals and Human Beings, with Additional Observations on Krypton, Science, 113 (1951) 580-582.
[66] S.-Y. Yeh, R.E. Peterson, Solubility of krypton and xenon in blood, protein solutions, and tissue homogenates, Journal of Applied Physiology, 20 (1965) 1041-1047.
[67] B. Driehuys, H.E. Moller, Z.I. Cleveland, J. Pollaro, L.W. Hedlund, Pulmonary Perfusion and Xenon Gas Exchange in Rats: MR Imaging with Intravenous Injection of Hyperpolarized Xe-129, Radiology, 252 (2009) 386-393.
[68] B. Driehuys, G.P. Cofer, J. Pollaro, J.B. Mackel, L.W. Hedlund, G.A. Johnson, Imaging alveolar-capillary gas transfer using hyperpolarized Xe-129 MRI, Proceedings of the National Academy of Sciences of the United States of America, 103 (2006) 18278-18283.
[69] K. Ruppert, J.F. Mata, J.R. Brookeman, K.D. Hagspiel, J.P. Mugler, Exploring lung function with hyperpolarized Xe-129 nuclear magnetic resonance, Magnetic Resonance in Medicine, 51 (2004) 676-687.
[70] K. Ruppert, J.R. Brookeman, K.D. Hagspiel, J.P. Mugler, Probing lung physiology with xenon polarization transfer contrast (XTC), Magnetic Resonance in Medicine, 44 (2000) 349-357.
[71] K. Ruppert, J.R. Brookeman, K.D. Hagspiel, B. Driehuys, J.P. Mugler, NMR of hyperpolarized Xe-129 in the canine chest: spectral dynamics during a breath-hold, Nmr in Biomedicine, 13 (2000) 220-228.
[72] K.F. Stupic, Z.I. Cleveland, G.E. Pavlovskaya, T. Meersmann, Quadrupolar Relaxation of Hyperpolarized Krypton-83 as a Probe for Surfaces, Solid State Nuclear Magnetic Resonance, 29 (2006) 79-84.
[73] N. Abdeen, A. Cross, G. Cron, S. White, T. Rand, D. Miller, G. Santyr, Measurement of xenon diffusing capacity in the rat lung by hyperpolarized 129Xe MRI and dynamic spectroscopy in a single breath-hold, Magnetic Resonance in Medicine, 56 (2006) 255-264.
[74] S. Mansson, J. Wolber, B. Driehuys, P. Wollmer, K. Golman, Characterization of diffusing capacity and perfusion of the rat lung in a lipopolysaccaride disease model using hyperpolarized Xe-129, Magnetic Resonance in Medicine, 50 (2003) 1170-1179.
[75] M.M. Spence, E.J. Ruiz, S.M. Rubin, T.J. Lowery, N. Winssinger, P.G. Schultz, D.E. Wemmer, A. Pines, Development of a functionalized xenon

biosensor, Journal of the American Chemical Society, 126 (2004) 15287-15294.
[76] C. Hilty, T.J. Lowery, D.E. Wemmer, A. Pines, Spectrally resolved magnetic resonance imaging of a xenon biosensor, Angewandte Chemie-International Edition, 45 (2006) 70-73.
[77] O. Taratula, I.J. Dmochowski, Functionalized 129Xe contrast agents for magnetic resonance imaging, Current Opinion in Chemical Biology, 14 97-104.
[78] M.M. Spence, S.M. Rubin, I.E. Dimitrov, E.J. Ruiz, D.E. Wemmer, A. Pines, S.Q. Yao, F. Tian, P.G. Schultz, Functionalized xenon as a biosensor, Proceedings of the National Academy of Sciences of the United States of America, 98 (2001) 10654-10657.
[79] E.J. Ruiz, D.N. Sears, A. Pines, C.J. Jameson, Diastereomeric Xe chemical shifts in tethered cryptophane cages, Journal of the American Chemical Society, 128 (2006) 16980-16988.
[80] D.N. Sears, C.J. Jameson, R.A. Harris, Nuclear magnetic shielding and chirality. I. The shielding tensor of Xe interacting with Ne helices, The Journal of Chemical Physics, 119 (2003) 2685-2690.
[81] J.P. Mugler, T.A. Altes, I.C. Ruset, I.M. Dregely, J.F. Mata, G.W. Miller, S. Ketel, J. Ketel, F.W. Hersman, K. Ruppert, Simultaneous magnetic resonance imaging of ventilation distribution and gas uptake in the human lung using hyperpolarized xenon-129, Proceedings of the National Academy of Sciences of the United States of America, 107 (2010) 21707-21712.
[82] Z.I. Cleveland, G.P. Cofer, G. Metz, D. Beaver, J. Nouls, S.S. Kaushik, M. Kraft, J. Wolber, K.T. Kelly, H.P. McAdams, B. Driehuys, Hyperpolarized Xe-129 MR Imaging of Alveolar Gas Uptake in Humans, Plos One, 5 (2010).
[83] K.F. Stupic, Z.I. Cleveland, G.E. Pavlovskaya, T. Meersmann, Hyperpolarized Xe-131 NMR spectroscopy, Journal of Magnetic Resonance, 208 (2011) 58-69.
[84] T.E. Chupp, K.P. Coulter, Polarization of Ne-21 by Spin Exchange with Optically Pumped Rb Vapor, Physical Review Letters, 55 (1985) 1074-1077.
[85] R.K. Ghosh, Spin exchange optical pumping of neon and its applications, (2009).
[86] Z.I. Cleveland, G.E. Pavlovskaya, N.D. Elkins, K.F. Stupic, J.E. Repine, T. Meersmann, Hyperpolarized Kr-83 MRI of lungs, Journal of Magnetic Resonance, 195 (2008) 232-237.
[87] Z.I. Cleveland, G.E. Pavlovskaya, K.F. Stupic, C.F. LeNoir, T. Meersmann, Exploring hyperpolarized 83Kr by remotely detected NMR relaxometry, Journal of Chemical Physics, 124 (2006) 044312.

Chapter 2

An overview of NMR, MRI, and hyperpolarized gas theory

This chapter will provide the basic overarching theory relating to NMR spectroscopy, hyperpolarized gas, and MRI. Specific theory topics will be covered in depth in their respective experimental chapters. Far more extensive overviews of the theory of all of these topics exist in the literature [1-4].

2.1 Signal intensity

2.1.1 NMR signal intensity (thermal equilibrium systems)

In order to be detected using NMR spectroscopy a nucleus must have a magnetic moment μ; which is defined as a function of the nuclear spin quantum number I, and the gyromagnetic ratio γ. This leads to Eq. 2.1.

$$\mu = \gamma I$$

[Eq. 2.1]

The orientation of the vector μ is randomly determined unless it is in the presence of an external magnetic field, B_0, in which case the magnetic moment of the nucleus will align with the field. For the sake of simplicity let us define B_0 as being a uniform, static field along the z-axis (which is the convention).

In the presence of B_0, μ can be one of a number of discrete values depending upon the value of I. Similarly this relates to an energy level shown in Eq. 2.2.

$$\hat{H} = -\gamma \hbar B_0 \hat{I}_Z$$

[Eq. 2.2]

Where $\hat{I}_Z$ is the spin operator in the z-axis denoted by the magnetic quantum number m that can only change by increments of one; it encompasses a range of values between $-I$ and I. For example, for a spin $I = 1/2$ nucleus $m = -1/2$ or $1/2$. Similarly, for a spin $I = 3/2$ nucleus m = -3/2, -1/2, 1/2, or 3/2, and so on.

Eq. 2.3 gives the number of available spin-states for a system.

$$N = 2I + 1$$

[Eq. 2.3]

Where N is the number of available states. Fig. 2.1 demonstrates this splitting for different magnetic quantum numbers.

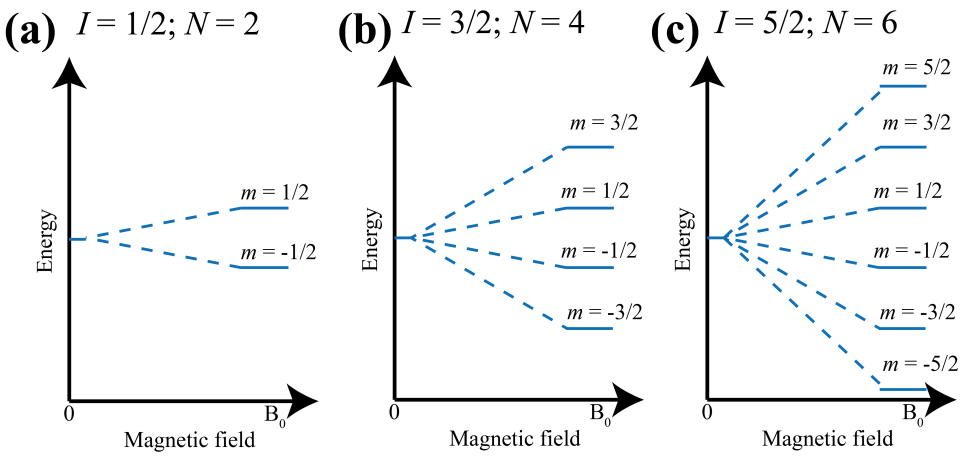

Fig. 2.1 – Energy level splitting for a given magnetic field strength for spins with different quantum numbers ***(a)*** *I = 1/2, as is the case for nuclei including* ^{1}H, ^{3}He, ^{129}Xe. *There are two potential energy states.* ***(b)*** *I = 3/2, as is the case for* ^{131}Xe, *the spin can be in one of four energy states.* ***(c)*** *I = 5/2 (i.e. for* ^{85}Rb*), there are six potential energy states.*

The transition between energy states results in the absorption or emission of energy as shown by Eq. 2.4.

$$\Delta E = \left|\gamma \hbar B_0 m\right|$$

[Eq. 2.4]

A transition can be caused by electromagnetic radiation (typically in the radio frequency regime) that meets the resonance condition. Pulsed irradiation at the resonance frequency may cause a precession (of the macroscopic ensemble) of the nuclear magnetic moments around the magnetic field. The precession frequency is defined as ω_0, the Larmor frequency (Eq. 2.5).

$$\omega_0 = \gamma B_0$$

[Eq. 2.5]

In practical terms when an NMR sample is excited by pulsed RF (radio frequency) radiation, nuclei are moved between energy state states. The resulting response (i.e. Larmor precession) is related to current induced in the NMR probe. This current is proportional to the magnetization of the precessing nuclei, its precession frequency, and the spin polarization described by the Boltzmann distribution. Therefore, the NMR signal intensity is primarily dependent on the magnetic field strength (B_0), the gyromagnetic ratio (γ) of the nuclei and the distribution of spin states.

2.1.2 Polarization (thermal equilibrium system)

The distribution of spin states is described by the Boltzmann distribution. For systems at thermal equilibrium in standard conditions the difference in population between spin states will be small. For simplicity let us consider a

nucleus of spin $I = 1/2$. For this we can describe a polarization, P, as being the difference between the populations of the spin-states.

$$P = \frac{n\uparrow - n\downarrow}{n\uparrow + n\downarrow}$$

[Eq. 2.6]

$n\uparrow$ denotes spins in the m = +1/2 spin state and $n\downarrow$ denotes spins in the m = -1/2 spin state. Using the Boltzmann distribution one can reach Eq. 2.7.

$$\frac{n\uparrow}{n\downarrow} = e^{\Delta E/k_B T} = e^{\gamma\hbar B_0 m/k_B T}$$

[Eq. 2.7]

Where k_B is the Boltzmann constant and T is the absolute temperature in Kelvin. From this one can derive an equation for polarization based on Eq. 2.6.

$$P = \frac{n\uparrow - n\downarrow}{n\uparrow + n\downarrow} = \frac{e^{-\gamma\hbar B_0 m/k_B T} - e^{-\gamma\hbar B_0 m/k_B T}}{e^{-\gamma\hbar B_0 m/k_B T} + e^{-\gamma\hbar B_0 m/k_B T}}$$

[Eq. 2.8]

Observable magnetization is proportional to the polarization. At high temperatures, such as those experienced under standard conditions, $\gamma\hbar B_0 m/k_B T$ « 1 as the difference between energy levels will be small. This is shown by the well-known equation (2.9), which is shown below.

$$P = \left(\frac{1}{2}\right)\frac{|\gamma|\hbar B_0}{kT}$$

[Eq. 2.9]

Magnetization is an important factor that contributes to NMR signal intensity. This can contribute to MRI image resolution, as higher resolutions are only possible with a high NMR signal-to-noise ratio. Bulk magnetization (M_0) as a function of the spin polarization is given by Eq. 2.10.

$$M_0 = \frac{1}{2} N_{Spin}\gamma\hbar P$$

[Eq. 2.10]

Where N_{Spin} is the number of spins in the sample. This can be combined with Eq. 2.9 to give Eq. 2.11.

$$M_0 = \frac{N_S \gamma^2 \hbar^2 B_0}{4kT}$$

[Eq. 2.11]

MR signal is the electro-motive force induced in the RF coil by the rotating magnetization. This can be given by the following equation [5]:

$$\xi = K\omega_0 (B_1)_{xy} M_0 V_0 \cos(\omega_0 t)$$

[Eq. 2.12]

Where $(B_1)_{xy}$ is the component of the excitation field in the x,y plane, K is a factor to account for field inhomogeneity, and V_0 is the sample volume. This can be combined with Eq. 2.5 and Eq 2.11 to reach Eq 2.13.

$$\xi = \left(\frac{KN_{Spin}\hbar^2 V_0 (B_1)_{xy}}{4kT} \right) \gamma^3 (B_0)^2 \cos(\omega t)$$

[Eq. 2.13]

This shows the factors that signal intensity is dependant upon for thermal equilibrium MRI, these being; B_1 field homogeneity, the cube of the gyromagnetic ratio, the square of the field strength, and sample size.

High concentrations of proton nuclei in most tissue makes clinical proton MRI viable, however proton MRI has limitations in organs that contain a low tissue-to-volume ratio, such as the lungs.

An additional factor not discussed so far is noise. In an ideal system, signal that is not produced from the sample would not be an issue. However in a real MR scanner sources of unwanted signal are introduced. Typically in a modern MR system Johnson noise will be the major cause of electrical noise. This is caused by agitation of the charge carrying electrons in a conductor. This can be introduced by various components, most notably the RF coil or the scanner itself. This introduces the concept of a signal-to-noise ratio (SNR); the only signal that is realistically usable is that that exceeds the noise. In a thermally polarized system there are some factors that improve signal that also increase the noise (such as temperature).

2.1.3 Polarization (hyperpolarized system)

As previously discussed signal intensity in NMR and MRI is dependant on various factors including the magnetic field strength, as well as the gyromagnetic ratio, the polarization and the concentration of the spin-active nuclei. The gyromagnetic ratio of a nucleus is an intrinsic quantum property and cannot be changed. Ideally to maximize signal intensity nuclei with high gyromagnetic ratios would be used for imaging (such as protons). Much lung airspace imaging to date has been preformed using ^{3}He due to its high gyromagnetic ratio. Some nuclei gyromagnetic ratios are listed in Table 1.1.

As the spin polarization of hyperpolarized systems are not governed by a thermal equilibrium Boltzmann distribution, and instead the polarization generated by hyperpolarization techniques (spin-exchange optical pumping in

this work), Eq. 2.11 is not true for hp gas systems. This means that the signal intensity takes the form of Eq. 2.14.

$$\xi = \left(\frac{KN_{Spin}\hbar V_0 (B_1)_{xy}}{2} \right) \gamma^2 B_0 \cos(\omega t) \cdot P$$

[Eq. 2.14]

Where P is the polarization due to SEOP. The SNR ratio for an hp system is dominated by the polarization, P.

Therefore signal intensity increases linearly with magnetic field strength (this is not necessarily completely true due to increased dephasing at higher field strengths). This factor is normally limited by available equipment, as the manufacture of high field strength scanners is non-trivial.

The concentration of spins (N_{Spin}) in airspace imaging is limited to the inhalation volume of the human lung. While a typical tidal volume is around ½ litre, imaging studies have been carried out where a litre of gas is inhaled [6].

Polarization (P) can be increased in noble gases using a process of spin-exchange optical pumping (SEOP). SEOP can be used to dramatically deplete one of the spin-states. Fig. 2.2 shows a representation of this with corresponding NMR spectra.

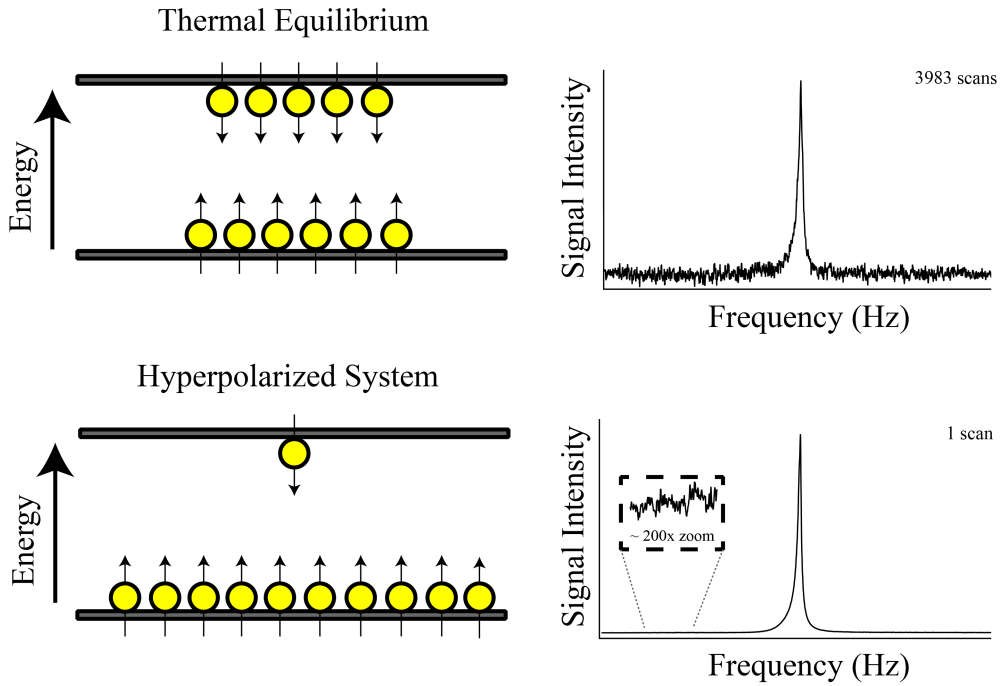

Fig. 2.2 – ***(Left)*** *A representation of spin-state distributions for a system in thermal equilibrium and a hyperpolarized system. At thermal equilibrium the spin-state populations are almost equal, whereas in the hyperpolarized system there is a greater discrepancy between the populations.* ***(Right)*** *Comparison between an NMR signal from a thermally polarized spin system and a system that has been hyperpolarized. Note that the signal-to-noise is significantly increased (by a factor of ~200) of the hyperpolarized spectrum recorded in a single acquisition as compared to the thermal spectrum after almost 4000 scans. Figure inspired by a diagram from literature [7].*

In a typical SEOP set-up the valence electron of an alkali metal vapour (the 5 ^{2}S electron in Rubidium) is electronically polarised via the resonant absorption of laser light tuned to the alkali D_1 absorption line (Fig. 2.3). The laser light is circularly polarised using a quarter-wave plate (which shifts components of the light) allowing only one of the Zeeman sublevels to be polarized due to quantum selection rules. Either left-handed or right-hand circularly polarized light can be chosen. Although the electrons will relax back into both sublevels, the constant selective excitation (and therefore depletion) will lead to an accretion of electrons in a single sublevel.

Excited electrons will relax to the ground state via a radiative process. This process will emit arbitrarily polarized photons that have a detrimental effect on the Rb polarization. As such, it is desirable to quench the emission of these photons. This is typically achieved by including N_2 in the SEOP cell to quench the florescence of the alkali metal vapour. The N_2 will dissipate the energy via a mode of vibration (i.e. through a non-radiative relaxation process) since its strong triple bond makes it very suitable for this role. ^{4}He is also commonly contained in the SEOP cell to increase the pressure and cause a pressure-dependant broadening of the D_1 absorption line [8]. As it is travelling through a

medium some of the laser light will experience changes in its propagation frequency. Broadening of the D_1 line allows the Rubidium electron to absorb a greater range of optical wavelengths, hence increasing the amount laser light absorbed. This can also help compensate for the line width limitations of the laser used. Greater laser power absorbed leads to higher Rb polarization.

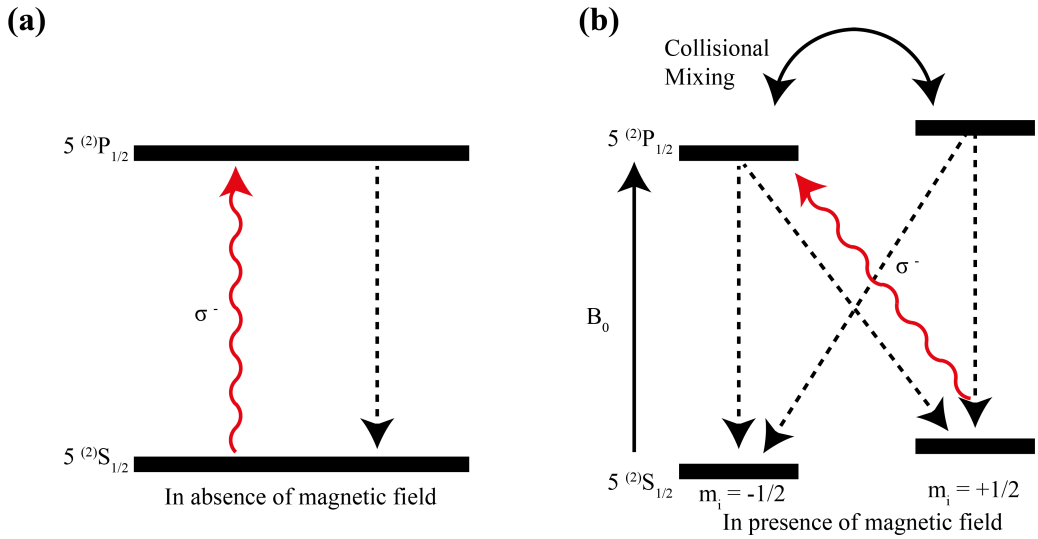

Fig. 2.3 – *(**a**) Excitation of the outer un-paired electron in Rb vapour by circularly polarized laser light in the absence of an external magnetic field. Under these conditions the energy levels are degenerate; there is no splitting of spin-states. (**b**) Excitation of the outer un-paired electron in Rb vapour by circularly polarized laser light in the presence of an external magnetic field (B_0). Zeeman splitting separates the two spin states. Therefore the circularly polarized laser light (tuned to the D_1 absorption) only excites one of the spin states. After collisional mixing the electron will relax back to either ground state. The overall process selectively depletes one of the spin-states. Energy splitting due to the Zeeman effect has been exaggerated on this diagram. Figure inspired by a diagram from literature* [9].

Polarization is transferred to the noble gas nuclei through the Fermi contact hyperfine interaction. This occurs when the alkali metal vapour and the noble gas come into contact either through binary collisions or through the formation of weakly bound van der Waals complexes as shown in Fig 2.4. Typically binary collisions are the dominant process for small nuclei (such as ^{3}He and ^{83}Kr) and van der Waals complexes become increasingly important for larger nuclei (for example, ^{129}Xe). During this interaction there is a finite probability that the unpaired, S-electron of the alkali metal will be at the location of the nucleus of the noble gas. If the spin of the electron and the spin of the noble gas nucleus are opposite then there will be an exchange of spin orientation, leading to a transfer of polarization.

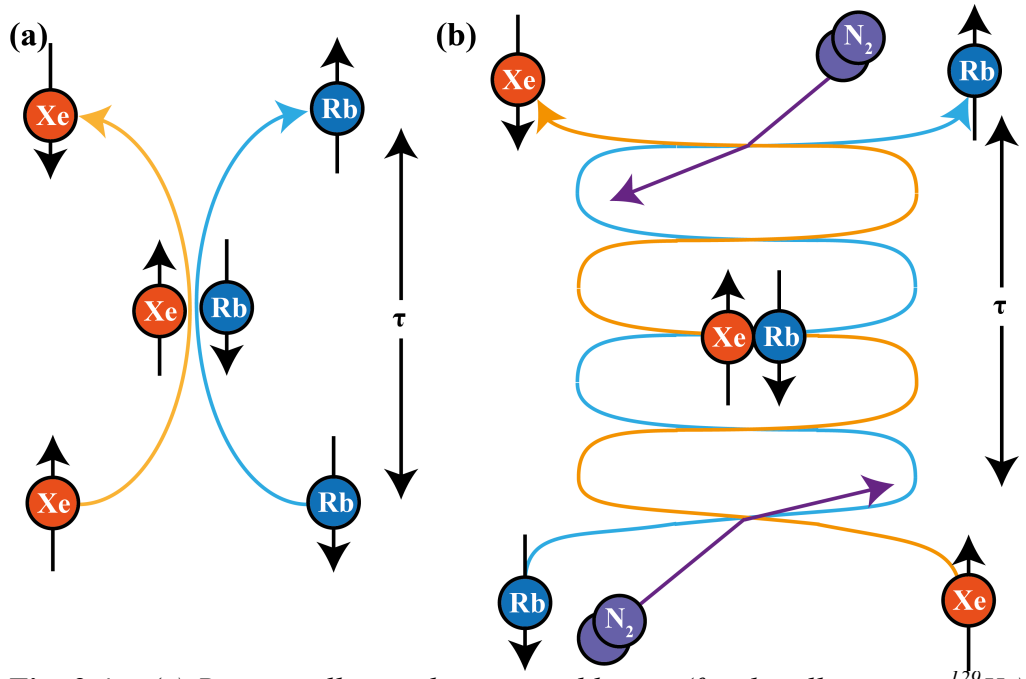

Fig. 2.4 *– **(a)** Binary collisions between noble gas (for this illustration ^{129}Xe) and the alkali metal vapour (for this illustration Rb). During this brief contact the Fermi hyperfine interaction allows polarization to be transferred from the S-electron of the alkali metal to the nucleus of the ^{129}Xe. **(b)** Three body collision leading to the formation of a weak van der Waals complex. In order to form the van der Waals complex momentum of the Rb and ^{129}Xe pair must be reduced. Initially the collision of a third body (for this illustration an N_2 molecule) can reduce the momentum of the other two bodies. Over the existence of the van der Waal complex the Fermi hyperfine interaction allows polarization to be transferred. A later collision with an N_2 molecule transfers momentum back to the two atoms breaking the van der Walls complex apart. Figure inspired by a diagram from literature [9].*

Happer and colleagues have conducted detailed theoretical studies of the SEOP process [1, 10]. Their 1984 paper detailed a quantum model for the Rb-SEOP of ^{129}Xe using a simple Hamiltonian to describe the spin relaxation and transfer in the SEOP cell as shown in Eq. 2.15 [1].

$$\hat{H} = A\vec{I}\cdot\vec{S} + \gamma\vec{N}\cdot\vec{S} + \alpha\vec{K}\cdot\vec{S} + g_S\mu_B\vec{B}\cdot\vec{S} + g_I\mu_B\vec{B}\cdot\vec{I} + g_K\mu_B\vec{B}\cdot\vec{K} + \ldots$$

[Eq. 2.15]

Where A, α and γ are coupling constants g_S, g_I and g_K are g-factors. $\vec{S}$ is the electron spin, $\vec{I}$ is the spin of the metal nucleus, $\vec{N}$ is the rotational angular momentum of the metal, $\vec{K}$ is the spin associated to the noble gas, and $\vec{B}$ is the magnetic field.

This equation neglects interactions due to a buffer gas (such as N_2 or He), as these are unimportant for explaining the optical pumping process more generally. It also discounts purely tensor-based interactions. Childs *et al.* have shown experimentally that with van der Waals molecules similar to those that form during the SEOP process, tensor interactions account for very little of the overall relaxation and transfer [11].

The term $A\vec{I}\cdot\vec{S}$ is a hyperfine interaction. This directly relates to the spin polarization of the unpaired outer electron of the alkali metal.

Terms containing the magnetic field $\vec{B}$ show the coupling between the spins of the electrons, alkali metal nuclei, and the Nobel gas nuclei and the applied magnetic field. It is responsible for the *normal* Zeeman Effect: the first order splitting of the energy levels dependant on the particles magnetic quantum number. This term is relatively small at the magnetic field strengths typically used in SEOP (40 - 80 G) and therefore these terms can be discarded.

The $\gamma\vec{N}\cdot\vec{S}$ term is responsible for the Anomalous Zeeman Effect that results in an additional energy level splitting during collisions or while the Rb and ^{129}Xe are part of a van der Waals complex. It relates to momentum transfer during these interactions and has been observed by Happer *et al.* to be the dominating causes of Rb relaxation during the SEOP process for ^{129}Xe SEOP.

The $\alpha\vec{K}\cdot\vec{S}$ term represents the Fermi contact hyperfine interaction between the noble gas nuclei and electrons of the alkali-metal vapour and is responsible for spin-exchange. This term can be expanded using quantum perturbation theory, however more simply it can be rewritten as shown by Eq. 2.16 [12].

$$\hat{H}_{KS} = \alpha\vec{K}\cdot\vec{S} = \frac{\alpha}{2}[K^+S + KS^+] + \alpha K_Z S_Z$$

[Eq. 2.16]

The term given in the square brackets contains the raising and lowering operators for K and S (commonly known as a flip-flop term) is responsible for spin-exchange between the alkali metal electron and noble gas nucleus. α is proportional to the probability of finding the unpaired alkali metal electron in the nucleus of the noble gas. This factor, contributing to actual spin exchange, is the primary part of Eq. 2.15 for determining Noble gas polarization.

Polarization of the noble gas as a function of time can be characterised by Eq. 2.17 [13].

$$P_{NG}(t) = \frac{\gamma_{SE} P_A}{\gamma_{SE} + \Gamma_{NG}} (1 - e^{-(\gamma_{SE} + \Gamma_{NG})t})$$

[Eq. 2.17]

Where P_{NG} is the total polarization of the noble gas, P_A is the average polarization of the alkali-metal vapour, and t is the residence time in the SEOP cell. γ_{SE} is the spin-exchange rate per atom of noble gas; it is a function of the spin-exchange rate constant of the alkali-metal, and the density of the alkali-metal vapour. Γ_{NG} is the relaxation rate of the noble gas in the absence of the alkali-metal vapour caused by wall collisions or magnetic field inhomogeneity.

The spin-exchange rate is determined by two mechanisms, the formation of van der Waals complexes, and binary collisions, described by Eq. 2.18 [14].

$$\gamma_{SE} = [A]\left(\frac{\gamma_{ANg} \zeta_A}{[Ng]} \left(\frac{1}{1 + br} \right) + \langle \sigma v \rangle \right)$$

[Eq. 2.18]

Where $[A]$ is the alkali metal density, γ_{ANg} is the spin-exchange rate between the noble gas and alkali metal when part of a van der Waal complex, ζ_A takes the isotopic composition of the alkali metal into account, $[Ng]$ is the noble gas number density, $\frac{1}{1+br}$ is a correction factor relating too take into account the presence of buffer gases, and $\langle \sigma v \rangle$ is the velocity averaged spin-exchange cross-section.

The average polarization of the alkali metal, P_A, is shown by Eq. 2.19.

$$P_A(z) = \frac{\gamma_{OP}(z)}{\gamma_{OP}(z) + \Gamma_A}$$

[Eq. 2.19]

Where $\gamma_{OP}(z)$ is the optical pumping rate per atom of alkali metal (at position z along the axis of the laser irradiation) and Γ_A is the rate of spin destruction

for the alkali metal electrons. This can be rewritten as a rate coefficient κ_A^i (which will depend on the gas mixture used) and a number density, $[M_i]$. From this we can reach Eq. 2.20.

$$P_{NG}(t) = \frac{\gamma_{SE}}{\gamma_{SE} + \Gamma_{NG}} \cdot \frac{\gamma_{OP}}{\gamma_{OP} + \sum \kappa_A^i [M_i]} (1 - e^{-(\gamma_{SE} + \Gamma_{NG})t})$$

[Eq. 2.20]

Eq. 2.20 can be simplified further for SEOP of certain isotopes when κ_A^i is considered. Literature values for N_2 and He (common buffer gases) are ≈ 9.4×10^{-24} m^3s^{-1} and ≈ 2.3×10^{-24} m^3s^{-1} respectively [15]. These are significantly lower than those for ^{129}Xe ($\kappa \approx 5.2\times10^{-21}$ m^3s^{-1}) or ^{83}Kr ($\kappa \approx 1.1\times10^{-21}$ m^3s^{-1}) [16]. The Rb-Rb spin destruction rate is large ($\kappa \approx 8.1\times10^{-19}$ m^3s^{-1}) [15], however at relatively high gas pressures the concentration of Rb, compared to gas, should be small resulting in negligible spin destruction.

It should be noted that the spin-destruction rates for Rb, Xe, and Kr were recorded at 300 K, far lower than the normal optical pumping temperature: Whereas the Rb, He and N_2 spin-destruction rates were taken at 420 K (close to the normal optical pumping temperature). It is therefore plausible that the actual Rb-NG spin relaxation rates are greater at the higher temperature, where more binary collisions would take place. It seems unlikely that values will go up by orders of magnitude, therefore in most cases for mixtures containing these noble gases (which make up the bulk of this work), the following simplification can be made [15, 16].

$$P_{NG}(t) = \frac{\gamma_{SE}}{\gamma_{SE} + \Gamma_{NG}} \cdot \frac{\gamma_{OP}}{\gamma_{OP} + \kappa_A^{NG} [Ng]} (1 - e^{-(\gamma_{SE} + \Gamma_{NG})t})$$

[Eq. 2.21]

2.2 Relaxation

2.2.1 Spin-lattice relaxation

As discussed earlier, in NMR spins, in the presence of the external field B_0, are excited by an RF pulse. This pulse reorients the magnetization of the spin from the longitudinal plane (M_Z) into the transverse one ($M_{X,Y}$) so that it can be detected. The application of a RF excitation also fulfils a resonance condition and the macroscopic magnetization will precess around the external field B_0 at the Larmor frequency ω_0. In a theoretically ideal system with only a single spin this condition would continue indefinitely however in a real system anisotropy in the local magnetic field leads to changes in the motion of individual spins. Eventually this results in the net magnetic moment of the spins returning to zero.

Relaxation can be described by the Bloch equations. The Bloch equations describe nuclear magnetisation as a function of time. In vector form the Bloch equations are given by Eq. 2.22.

$$\frac{d\bar{M}(t)}{dt} = \gamma \bar{M}(t) \times \bar{B}(t)$$

[Eq. 2.22]

Where $\bar{M}(t)$ is the nuclear magnetisation as a function of time, and $\bar{B}(t)$ is the magnetisation as a function of time. This equation forms the basis for Eq. 2.23 and Eq. 2.27.

One of the mechanisms responsible is spin-lattice relaxation. Otherwise known as T_1, or longitudinal relaxation, it describes the return of the spin magnetization from the transverse plane to the direction of the external field. Thermal motion within the sample (the lattice) means that other atoms (with their own magnetic fields) will create local fluctuations in the magnitude and direction of the overall field. Over many precessions the angle between the field B_0 and the plane that the nuclei precess in will change slightly.

Spins favour being in their lowest energy state for a given temperature, and will tend towards that state after an RF excitation. This is their thermal equilibrium state. As discussed before, at ambient temperature only a very small portion of the spins will orient themselves with the external magnetic field, leading to a very low net magnetic moment.

The change in magnetization due to relaxation can be described by Eq. 2.23.

$$\frac{dM_Z}{dt} = T_1[M_0 - M_Z(t)]$$

[Eq. 2.23]

Where M_0 is the magnetization at Boltzmann equilibrium and M_Z is the magnetization at time t after a RF pulse, and T_1 is a time constant. This can be rearranged and integrated. We can say that when t = infinity, the system has reached thermal equilibrium and therefore, $M_0 - M_Z = 0$. Similarly, at $t = 0$ (immediately after the RF excitation), $M_Z = 0$, as all of the magnetization would have been moved into the transverse plane. After rearranging the equation again we reach Eq. 2.24.

$$M_Z(t) = M_0[1 - e^{-t/T_1}]$$

[Eq. 2.24]

This description only holds true for thermal equilibrium systems. In a hyperpolarized system M_Z will be substantially greater than M_0. An approximation can be reached if we define $M_Z(0)$ as being the starting magnetization.

$$M_Z(t) \approx M_Z(0)[1 - e^{-t/T_1}]$$

[Eq. 2.25]

2.2.2 Measuring spin-lattice relaxation

2.2.2.1 Saturation recovery

A common method used to obtain the relaxation constant T_1 in a thermal system is to use a pulse sequence known as a saturation recovery. This method uses a series of dual 90º pulse. Between the two pulses there will be a given time, τ_R that is incremented (Fig. 2.5a). If the time is too short then the magnetization will not have relaxed fully back to its thermal equilibrium point, and therefore the second pulse will move much of the magnetization out of the observable plane, giving a weak signal. However if there has been sufficient time for most of the magnetization to relax back to thermal equilibrium then the second pulse will move most of the magnetization into the observable plane, resulting in a strong signal (Fig. 2.5b).

Signal strength as a function of time, τ_R, can be plotted (Fig. 2.5c) using Eq. 2.24 and T_1 can be extracted.

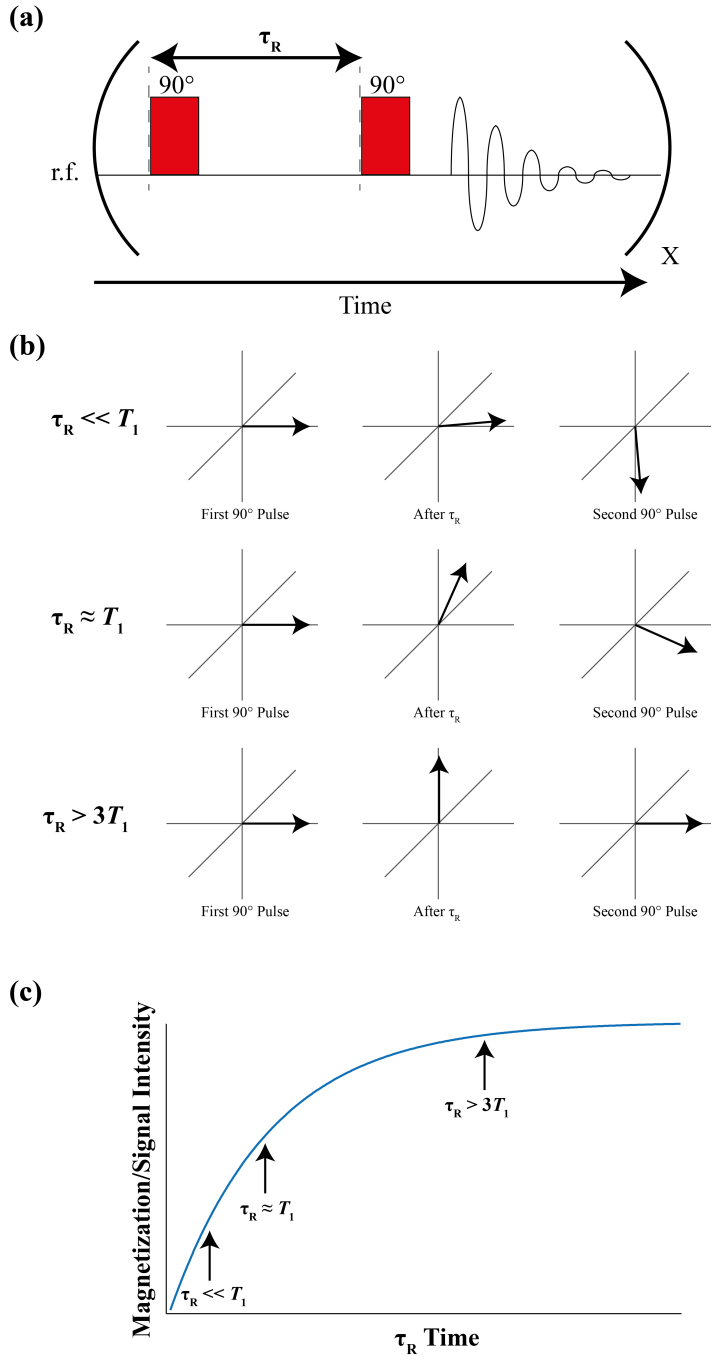

Fig. 2.5 *– **(a)** Saturation recovery NMR sequence. The sequence contains two 90° pulses separated by a time interval τ_R. The sequence is repeated X times; a minimum of five repeats is necessary so that the data can be fit exponentially (as shown in Fig. 2.5c). **(b)** Diagram illustrating the position of longitudinal magnetisation of spins at different time intervals τ_R. Corresponding observed magnetisations are shown in Fig. 2.5c. This diagram is only an artistic rendition and does not describe the exact position of magnetisation.*
*(**c**) Observed magnetisation as a function of time intervals τ_R fit to Eq. 2.24.*

This method cannot be used with hyperpolarized gas as once the gas has relaxed back to its thermal equilibrium state the polarization enhancement is lost.

2.2.2.2 Inversion recovery

Inversion recovery is another common method to acquire T_1 in a thermal system. This sequence consists of a 180° pulse followed by a 90° pulse at the time τ_R. If the delay τ_R is too short then the signal will have a negative intensity as the magnetisation will have been rotated beyond the x,y plane. After a very short time ($\tau_R << T_1$), little of the magnetization will have reoriented 90° with respect to the x,y plane. An additional 90° pulse would orient the magnetization into the negatively phased observable plane, resulting in a large negative signal. Conversely, maximum signal would be achieved when the delay is very long and the magnetization would be given time to recover from the 180° pulse ($\tau_R >> T_1$).

Signal intensity is plotted against the pulse delay time τ_R (Fig 2.6c). Eq. 2.24 must be modified to account for the inversion of magnetization (Eq. 2.26), and can be used to fit the data to extract T_1.

$$M_Z(t) = M_0(1 - 2e^{-t/T_1})$$

[Eq. 2.26]

Inversion recovery experiments are also impractical to measure T_1 in hyperpolarized gases. As with saturation recovery experiments the polarization enhancement is lost once the gas has relaxed back to thermal equilibrium, making these point-by-point experiments very time consuming.

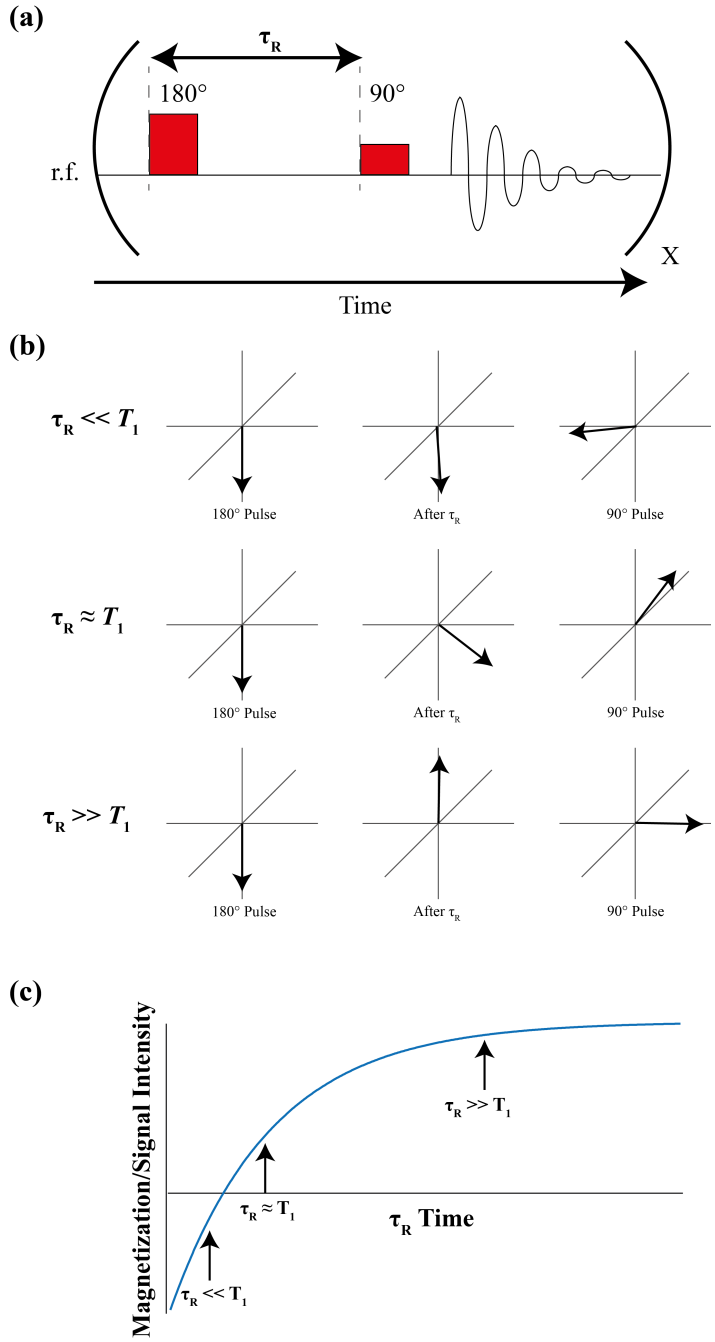

Fig 2.6 *– **(a)** Inversion recovery NMR sequence. The sequence contains one 180° pulse followed by one 90° pulse, separated by a time interval τ_R. The sequence is repeated X times; a minimum of five repeats is necessary so that the data can be fit exponentially (as shown in Fig. 2.6c). **(b)** Diagram illustrating the position of longitudinal magnetisation of spins at different time intervals τ_R. Corresponding observed magnetizations are shown in Fig. 2.6c). This diagram is only an artistic rendition and does not describe the exact position of magnetization. **(c)** Observed magnetization as a function of time intervals τ_R fit to Eq. 2.26.*

2.2.2.3 T_1 measurements in hp systems

A method to obtain T_1 values in an hp system is by using a sequence of small to medium flip-angle pulses. The sequence is displayed in Fig. 2.7 below. For each subsequent pulse the overall experimental time gets longer, and as a consequence the signal intensity will decrease. This is due to two factors; the dominating factor will be T_1 however signal will also deteriorate due to destruction of polarization from each RF excitation. It is desirable to keep this destruction to a minimum as diffusion of new gas that has not been excited by RF may alter the results. Due to this additional factor, and the fact that the behaviour being explored is the decay of signal, the data must be fit to Eq. 2.27. Eq. 2.27 compensates for spin destruction due to RF pulses.

$$M_Z(t) \approx (\cos\theta)^{t/\tau} e^{-t/T_1}$$

[Eq. 2.27]

Where θ is the flip angle in radians and τ is the time between pulses. An example of this fitting is given in Fig. 2.7c.

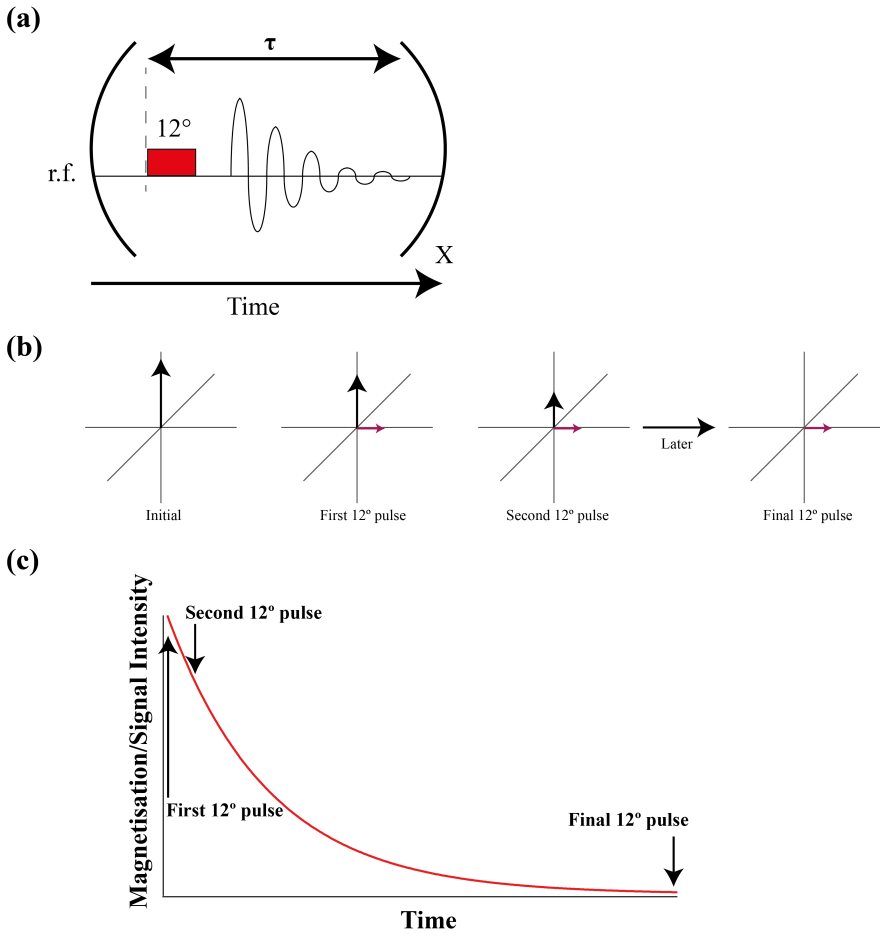

Fig. 2.7 *– **(a)** Medium flip-angle NMR sequence. For this particular example a 12° pulse length has been used. Pulses are spaced by the time interval τ. There are X number of pulse, this number must at least be five in order to characterise the exponential correctly. **(b)** Diagram illustrating the position of longitudinal magnetization of spins at different time intervals τ. Corresponding observed magnetisations are shown in Fig. 2.7c. This diagram is only an artistic rendition and does not describe the exact position of magnetisation. **(c)** Observed magnetization as a function of time intervals τ fit to Eq. 2.27.*

2.2.3 Spin-spin relaxation

The other relaxation mechanism in excited spin-systems is spin-spin, or transverse relaxation. This relaxation describes the de-phasing of the precession of spins once the magnetization has been tipped into the transverse plane (perpendicular to the B_0 field). Initially once an RF pulse is applied and the magnetization is tipped into the transverse plane, spins will begin precessing from the same point. However due to anisotropy in the net magnetic field the precession frequency of individual spins will be slightly different. Over time the spins will fall out of synchronization with one-another, ultimately leading to a net observable magnetization in the transverse plane ($M_{x,y}$) to equal zero. For dephasing caused by dipole interactions between two spins, the magnetization decays with the time constant T_2. This can be described similarly to T_1 in Eq. 2.24.

$$\frac{dM_{X,Y}}{dt} = T_2[M_0 - M_{X,Y}(t)] = -T_2 M_{X,Y}$$

[Eq. 2.28]

Where M_0 is again the magnetization at equilibrium. $M_{X,Y}$ at t = 0 is the net magnetization in this plane following the RF pulse. This equation can then be solved, ultimately giving Eq. 2.29.

$$M_{X,Y}(t) = M_{X,Y}(0)e^{-t/T_2}$$

[Eq. 2.29]

Where $M_{x,y}(0)$ is the magnetization in the transverse plane immediately after RF excitation.

T_2 is always either shorter than or equal to T_1.

2.2.3.1 Dephasing due to the inhomogeneity of the magnetic field B_0

While not strictly a relaxation process dephasing can also occur due to inhomogeneity in the magnetic field B_0. This can be due to many physical reasons leading to anisotropy in the magnetic environment. This effect is often added to the effect of the dephasing due to dipole interactions; this decay time constant is known as T_2*.

$$\frac{1}{T_2 *} = \frac{1}{T_2} + \frac{1}{T_{INHOM}} = \frac{1}{T_2} + \gamma \Delta B_0$$

[Eq. 2.30]

Where T_{INHOM} is the decay time constant of the magnetization as a result of dephasing due to field inhumanity and ΔB_0 is the difference in field strength of the inhomogeneity T_2*.

T_2* is always either shorter than or equal to T_2.

T_2* can be determined from the line width of an NMR spectrum. The full-width-half-maximum (FWHM) is equal to the reciprocal of T_2*.

2.2.4 Measuring spin-spin relaxation

2.2.4.1 Carr-Purcell-Meiboom-Gill sequence

Derived from the Hahn spin-echo sequence the Carr-Purcell-Meiboom-Gill (CPMG) [17] sequence (shown in Fig. 2.8a) is commonly used to measure the relaxation constant T_2. An initial 90º pulse is applied causing the magnetisation to move into the transverse plane and start to precess, and therefore also dephase. After a time, τ_E, a 180º pulses is applied inversing the magnetisation. Dephasing effects caused by field inhomogeneity will be reversed and after another τ_E this aspect of the dephasing will be refocused. This does not however refocus dephasing caused by dipole interactions (i.e. the true T_2). After multiple 180º pulses the decrease in signal intensity (and therefore observable magnetization) due to this dephasing can be plotted as a function of time, and from this the time constant T_2 can be extracted.

This method of refocusing the spin precessions is a useful tool to acquire the highest possible signal intensity in NMR and MRI applications.

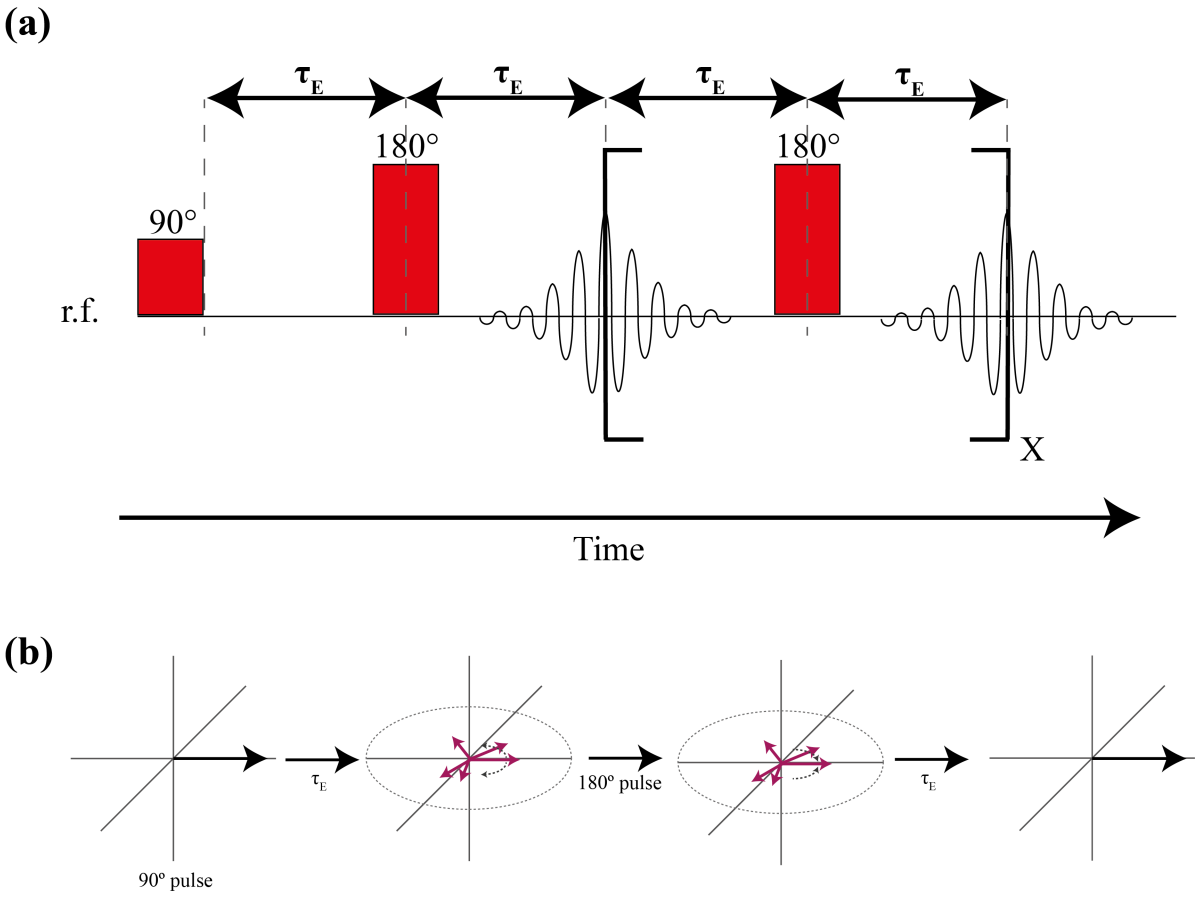

Fig. 2.8 *– **(a)** Carr-Purcell-Meiboom-Gill pulse sequence. Pulses are spaced by a time interval $2\tau_E$. There are X number of pulse, this number must at least be five in order to characterise the exponential correctly. **(b)** Diagram illustrating the position of transverse magnetization of spins at different time intervals τ_E. This diagram is only an artistic rendition and does not describe the exact position of magnetization.*

2.3 Magnetic resonance imaging

Eq. 2.5 states the resonance condition for most NMR experiments. While NMR can be useful in obtaining chemical and structural information of a sample, it cannot give quantified spatial information. In order to spatially encoded NMR data one can alter the Larmor frequency slightly by applying a small additional magnetic field, or gradient, over the sample. This is called frequency encoding and is described by Eq. 2.31.

$$\omega(r) = \gamma(B_0 + G \cdot r)$$

[Eq. 2.31]

$\omega(r)$ is the precession frequency of the spin at spatial coordinates r and where G is the gradient field strength in Tesla. With a single linear gradient over a sample spins on one side of a sample will experience greater field strength, and therefore precess faster, while on the other side of sample the spins are exposed to lower field strengths and therefore precess more slowly (Fig. 2.9). Ultimately a NMR spectrum's line-shape will be a product of T_2* and the ω. If ω changes subtlety with position then this information will be apparent in the spectrum.

This forms the basic principles of imaging. Different kinds of gradient can be applied to manipulate the spins in a sample in order to acquire special information. These are slice, phase, and frequency encoding gradients.

Slice selective gradients are linear gradients applied during an RF excitation pulse. As discussed above, this linear gradient alters the precession frequency of the spins depending on their location. By exciting just a small range of frequencies (relating to the desired location) only NMR information from the selected spins will be collected.

Phase discrimination between spins can also be used to acquire spatial information. By applying a phase encoding gradient dephasing can be induced in certain spins: Dephasing will affect all spins other than those perpendicular to the phase encoding gradient. Ultimately the complete dephasing of the other spins will mean that only those spins perpendicular to the phase encoding gradient will contribute to the NMR signal.

The third type of gradient is frequency encoding, as described by Eq. 2.31. Applied after the RF excitation, the resonant frequency of the excited spins will be altered depending on their location as with a slice selective gradient.

By incrementing the gradients, 1D *images* from different locations in the sample can be acquired. Multiple 1D images using different phase encoding gradients can be collected. Ultimately multiple 1D images can be digitally constructed into a two or three-dimensional images.

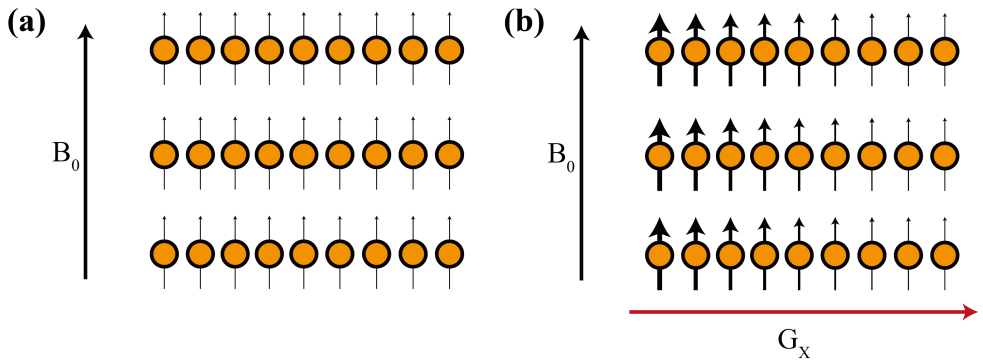

Fig. 2.9 *– Gradient effecting spins over a sample. The direction of the gradients is shown only intended to represent the direction by which the magnetizations of the spins are affected. Magnitudes of magnetization are greatly exaggerated for the purposes of this figure. (**a**) Spins of a sample in the presence of a magnetic field B_0. (**b**) Spins of a sample in the presence of a magnetic field B_0 with a linear gradient, G_X, being applied. Spins on one side of the sample experience a greater magnetic field, and therefore have a greater larmor frequency, while spins on the other side of the sample experience a lesser magnetic field strength resulting in a lower precession frequency.*

2.3.1 Spin-echo MRI

One common imaging sequence is the spin-echo sequence. Spin-echo MRI makes use of 180º pulses in order to re-focus the precession of spins in the transverse plane. The concept of an 'echo' (re-focussing pulse) was first proposed by Hahn [18], and is also used in the CPMG sequence described earlier.

An initial 90º pulse is applied to move the magnetisation into the transverse plan. A phase encoding gradient is then applied over the sample. This causes dephasing of the transverse precession of all spins other than those perpendicular to the phase encoding gradient.

A slice selective gradient is applied. An 180º pulse is applied to excite the spins affected by this gradient. The transverse precession of these spins will therefore re-phase after a given time has passed (τ_E).

Finally a frequency-encoding gradient is applied over the sample. As shown by Fig 2.9 this slightly alters the precession frequencies of the selected spins so that their frequencies are a function of location. This spatially encoding will be retained when the spectrum (a 1D image) is collected.

This process may be repeated with successive 180º pulses with different gradient strengths in order to generate a two or three-dimensional image. The number of repeats will depend on the overall time, which is limited by the time constant T_2 as dephasing due to dipole interactions will not be refocused after a 180º pulse.

Spin-echo imaging has been achieved with hp ^{3}He at low (<0.3 mT) magnetic field strengths (Rapid Acquisition with Refocused Echoes, RARE sequences where used) [19, 20].

One consideration with this imaging modality for hp gas imaging is that a perfect 180° pulse is necessary, otherwise the RF excitation would destroy some of the hp gas polarization. This would result in lower signal from 1D-spectra taken later in the imaging sequence, which is undesirable. Also, each 180° pulse would invert the magnetisation for the next line of the image [21], meaning that each line would have to be phased separately.

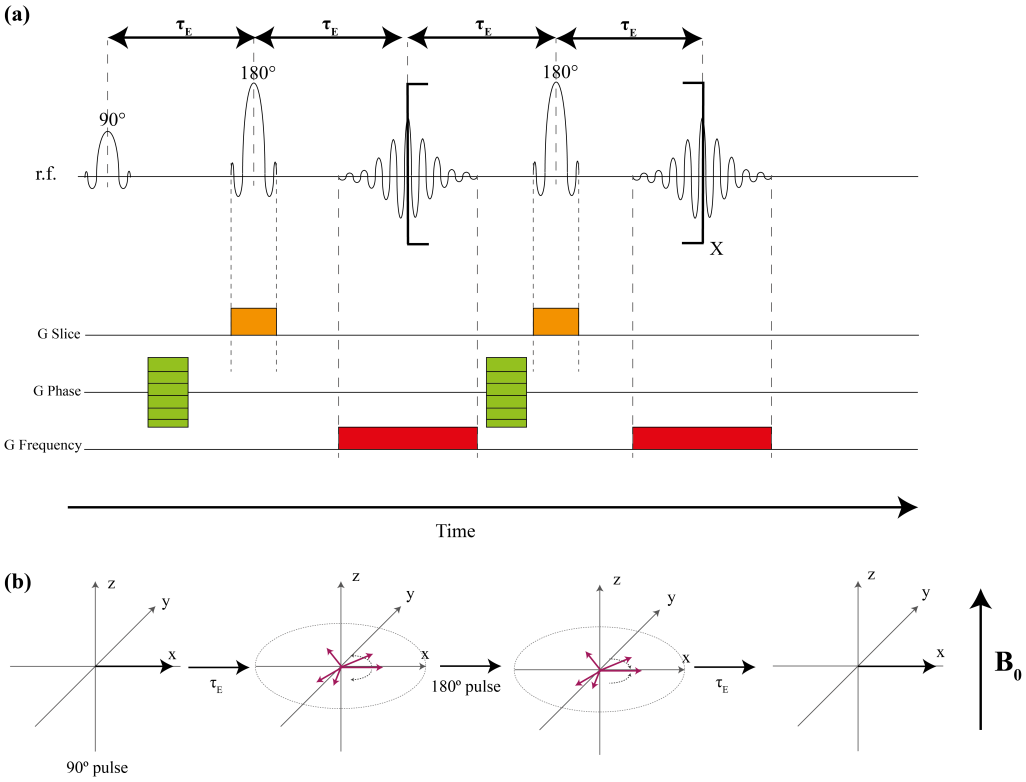

Fig. 2.10 *– **(a)** Spin-echo MRI pulse sequence. 180° pulses are spaced by a time interval $2\tau_E$. There are X + 1 number of pulses, this number is limited by the overall experiment time from after the 90° pulse, which must be less than the time constant T_2. After the time constant T_2 the spin-precessions will have dephased significantly, leading to a low signal intensity. **(b)** Diagram illustrating the position of transverse magnetization of spins at different time intervals. After the initial 90° pulse, spins dephase in the transverse plane. The application of an 180° pulse causes the spins to precess in the opposite direction. After $t = \tau_E$, this means that the spins will be in a position similar to the position that they were in immediately after the initial 90° pulse. Dephasing due to T_2 relaxation will not be refocused by the 180° pulse. This diagram is only an artistic rendition and does not describe the exact position of magnetization.*

2.3.2 Gradient-echo MRI

Gradient-echo MRI works on the same basic principles of spin-echo MRI except a small flip angle *can* be used (shown as *a°* in Fig. 2.11) and there are no 180º refocusing pulses. As no 180º pulses are present to refocus the transverse magnetisation, a frequency-encoding gradient in the opposite direction to the *readout* frequency-encoding gradient is applied in order to reverse the directions of the precessing spins.

Fast Low-Angle SHot (FLASH) gradient-echo imaging was originally developed for proton MRI [22]. It is as a method to acquire T_2*-weighted images (spin-echo being T_2-weighted, although acquiring T_1-weighted spin-echo images is also possible).

In a gradient-echo imaging sequence a variable flip angle can be used. For hp gas imaging, starting with a small flip angle ensures that little polarization is destroyed after each excitation pulse: As a result the numerous excitation pulses required for different gradients can be applied using a single batch of hp gas. Increasing the flip angle for successive iterations of the sequence ensures that each scan has the same relative intensity to the previous one. The flip angle can be calculated by Eq. 2.32 [23].

$$\theta_n = \tan^{-1}\left(\frac{1}{\sqrt{N-n}}\right)$$

[Eq. 2.32]

Where N is the total number of pulses, n is the nth excitation pulse. θ_n is corresponding flip angle.

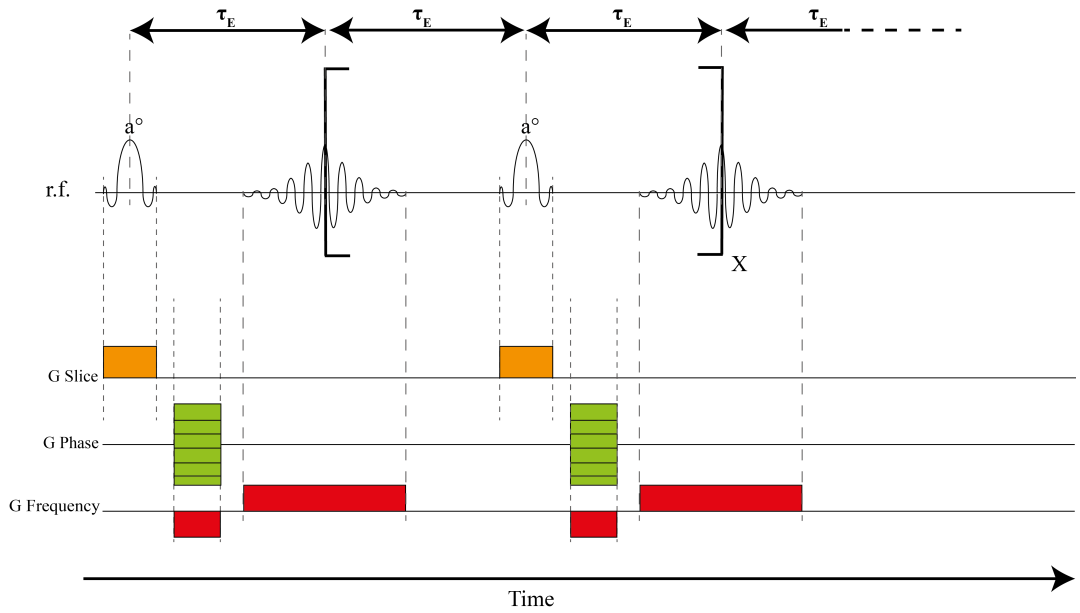

Fig. 2.11 *– Gradient-echo MRI pulse sequence. a° pulses are spaced by a time interval $2\tau_E$. There are X + 1 number of pulse. For a hyperpolarized system a° is variable, with each pulse increasing to compensate for the loss of polarization due to subsequent pulses.*

2.4 References

[1] W. Happer, E. Miron, S. Schaefer, D. Schreiber, W.A. Vanwijngaarden, X. Zeng, Polarization of the Nuclear Spins of Noble-Gas Atoms by Spin Exchange with Optically Pumped Alkali-Metal Atoms, Physical Review A, 29 (1984) 3092-3110.
[2] M.H. Levitt, Spin Dynamics: Basics of Nuclear Magnetic Resonance, John Wiley & Sons, LTD, West Sussex, UK, 2001.
[3] P.T. Callaghan, Principles of Nuclear Magnetic Resonance Microscopy, Oxford University press, New York, 1991.
[4] C.P. Slichter, Principles of Magnetic Resonance, 3rd ed., Heidelberg, 1963.
[5] D.I. Hoult, R. Richards, The signal-to-noise ratio of the nuclear magnetic resonance experiment, Journal of Magnetic Resonance (1969), 24 (1976) 71-85.
[6] J.P. Mugler, B. Driehuys, J.R. Brookeman, G.D. Cates, S.S. Berr, R.G. Bryant, T.M. Daniel, E.E. deLange, J.H. Downs, C.J. Erickson, W. Happer, D.P. Hinton, N.F. Kassel, T. Maier, C.D. Phillips, B.T. Saam, K.L. Sauer, M.E. Wagshul, MR imaging and spectroscopy using hyperpolarized Xe-129 gas: Preliminary human results, Magnetic Resonance in Medicine, 37 (1997) 809-815.
[7] B.M. Goodson, Using injectable carriers of laser-polarized noble gases for enhancing NMR and MRI, Concepts in Magnetic Resonance, 11 (1999) 203-223.
[8] M.V. Romalis, E. Miron, G.D. Cates, Pressure broadening of Rb D-1 and D-2 lines by He-3, He-4, N-2, and Xe: Line cores and near wings, Physical Review A, 56 (1997) 4569-4578.
[9] B.M. Goodson, Nuclear magnetic resonance of laser-polarized noble gases in molecules, materials, and organisms, Journal of Magnetic Resonance, 155 (2002) 157-216.
[10] T.G. Walker, W. Happer, Spin-exchange optical pumping of noble-gas nuclei, Review of Modern Physics, 69 (1997) 629-642.
[11] W.J. Childs, D.R. Cok, L.S. Goodman, Hyperfine structure of the X [sup 2] Sigma [sup +] ground state of Ca [sup 35]Cl and Ca [sup 37]Cl by molecular-beam, laser-rf double resonance, The Journal of Chemical Physics, 76 (1982) 3993-3998.
[12] E. Brunner, Enhancement of surface and biological magnetic resonance using laser-polarized noble gases, Concepts in Magnetic Resonance, 11 (1999) 313-335.
[13] T.E. Chupp, M.E. Wagshul, K.P. Coulter, A.B. McDonald, W. Happer, Polarized, high-density, gaseous ^{3}He targets, Physical Review C, 36 (1987) 2244-2251.
[14] G.D. Cates, R.J. Fitzgerald, A.S. Barton, P. Bogorad, M. Gatzke, N.R. Newbury, B. Saam, Rb Xe-129 Spin-Exchange Rates Due to Binary and 3-Body Collisions at High Xe Pressures, Physical Review A, 45 (1992) 4631-4639.
[15] M.E. Wagshul, T.E. Chupp, Laser Optical-Pumping of High-Density Rb in Polarized He-3 Targets, Physical Review A, 49 (1994) 3854-3869.
[16] M.A. Bouchiat, J. Brossel, L.C. Pottier, Evidence for Rb Rare-Gas Molecules from Relaxation of Polarized Rb-Atoms in a Rare-Gas - Experimental Results, Journal of Chemical Physics, 56 (1972) 3703-3714.

[17] S. Meiboom, D. Gill, Modified Spin-Echo Method for Measuring Nuclear Relaxation Times, The Review of Scientific Instruments, 29 (1958) 688-691.
[18] E.L. Hahn, Phys. Rev., 80 (1950) 580.
[19] C.P. Bidinosti, J. Choukeife, G.v. Tastevin, P.-J. Nacher, A. Vignaud, MRI of the lung using hyperpolarized 3He at very low magnetic field (3 mT), Magnetic Resonance Materials in Physics, Biology and Medicine, 16 (2004) 255-258.
[20] E. Durand, G. Guillot, L. Darrasse, G. Tastevin, P. Nacher, A. Vignaud, D. Vattolo, J. Bittoun, CPMG measurements and ultrafast imaging in human lungs with hyperpolarized helium‚Äê3 at low field (0.1 T), Magnetic resonance in medicine, 47 (2002) 75-81.
[21] E.E. de Lange, J.P. Mugler, J.R. Brookeman, J. Knight-Scott, J.D. Truwit, C.D. Teates, T.M. Daniel, P.L. Bogorad, G.D. Cates, Lung air spaces: MR imaging evaluation with hyperpolarized He-3 gas, Radiology, 210 (1999) 851-857.
[22] J. Frahm, A. Haase, D. Matthaei, Rapid NMR imaging of dynamic processes using the FLASII technique, Magnetic Resonance in Medicine, 3 (1986) 321-327.
[23] L. Zhao, R. Mulkern, C.H. Tseng, D. Williamson, S. Patz, R. Kraft, R.L. Walsworth, F.A. Jolesz, M.S. Albert, Gradient-echo imaging considerations for hyperpolarized Xe-129 MR, Journal of Magnetic Resonance Series B, 113 (1996) 179-183.

Chapter 3

Optimizing the spin-exchange optical pumping process for ^{83}Kr and ^{129}Xe

Acknowledgements

The work presented in this chapter was combined with additional experiments and data analysis not presented in this thesis and was published as *Pathway to Cryogen Free Production of Hyperpolarized Krypton-83 and Xenon-129* in the journal PLoS One [1]. The author list of the publication was Joseph S. Six, **Theodore Hughes-Riley**, Dr. Karl F. Stupic, Dr. Galina E. Pavlovskya, and Prof. Thomas Meersmann.

The experiments in this work were carried out by Joseph S. Six and Theodore Hughes-Riley together; additional experiments were carried out by Joseph S. Six to complete the manuscript for publication but have mostly not been included in this thesis. The exceptions are Fig. 3.3 and Fig. 3.6 that were collected by Joseph S. Six.

Data analysis for the publication was conducted by Joseph S. Six and Dr. Galina E. Pavlovskya. This was used to develop some of the arguments made in this chapter.

Dr. Karl F. Stupic and Dr. Galina E. Pavlovskya designed and built the polarizer used.

The experiments were conceived by Prof. Thomas Meersmann.

3.1 Introduction and background

As discussed in **Chapter 2** (Section 2.1.3) the signal intensity of a hyperpolarized system is proportional to the gyromagnetic ratio (γ) squared, and not cubed as it is for thermally polarized systems. As ^{83}Kr has a significantly lower gyromagnetic ratio to other noble gas nuclei including ^{3}He and ^{129}Xe, it has a correspondingly weaker NMR signal intensity (if the polarizations were equal and at a given field strength).

This is not the only contributing factor to signal intensity. In a perfectly uniform field signal intensity would increase linearly with the magnetic field strength (B_0). Practically speaking a perfectly uniform field does not exist resulting in dephasing due to field inhomogeneity. The strength of this dephasing is also linear with the field strength (Eq. 2.30) and will be less severe for lower gyromagnetic ratio isotopes. This difference has been observed between two Xe isotopes (^{129}Xe and the quadrupolar ^{131}Xe) [3].

^{83}Kr also has a lower natural abundance than ^{129}Xe (11.5% for ^{83}Kr, compared to 26.4% for ^{129}Xe). MR making the use of an isotopically enriched version of the ^{83}Kr isotope would be favourable, as a potential 8-fold signal enhancement can be achieved with enrichment. Due to the limited demand for isotopically enriched ^{83}Kr the gas is not commonly separated from its other isotopes leading to a considerable cost; about € 4000 per litre at 2011 prices. This cost may be prohibitive for the large quantities of gas required in human studies, however if techniques using ^{83}Kr imaging became more widespread the cost would likely come down, as it did significantly with ^{129}Xe. It may also prove possible to recover, clean, and reuse enriched gas, which may significantly reduce the cost of such experiments.

Even with the enhancement offered with enriched gas, it is sensible to first optimize the SEOP process before costly enriched gas is expended. This chapter will detail attempts to improve the polarization of hp ^{83}Kr, and advances made in the SEOP process for ^{129}Xe made in the process.

Previously published work has successfully allowed for the imaging of hp ^{83}Kr in an *ex vivo* rat lung (Fig. 3.1). The image was acquired using a series of sixteen hp gas deliveries, each delivery corresponding to an individual trace, which were then reconstructed. While showing that imaging ^{83}Kr in a lung is possible, as the image was non-slice-selective and took a number of scans to compile, it would be of limited value for clinical and preclinical studies. In order to acquire higher resolution imaging, which allows for slice selection in a single scan, MR signal intensity must be improved.

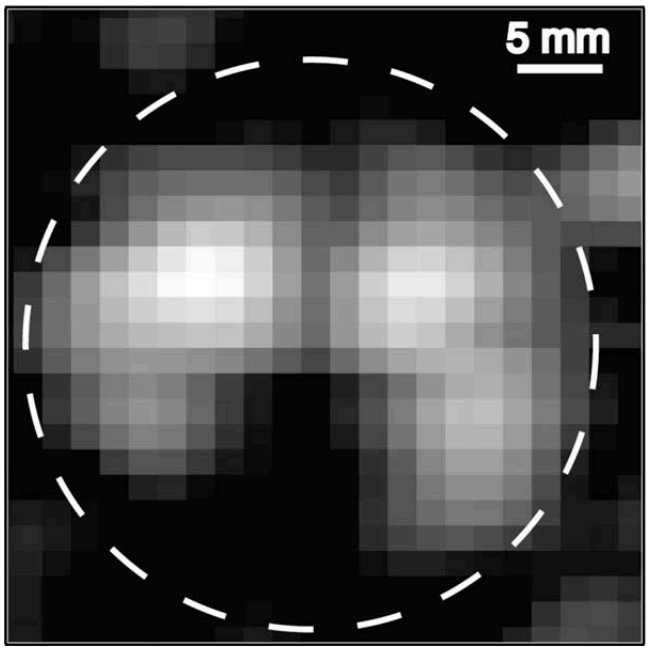

Fig. 3.1 *– ^{83}Kr transverse rat lung image from literature, acquired at 9.4 T. A gradient-echo imaging sequence was used. 16 separate hp gas deliveries and scans were taken, each scan corresponding to signal traces that were reconstructed into an image [2]. Reproduced with permission from Elsevier. © 2008 Elsevier.*

Possible methods to increase the MR signal from hp gas at a given temperature, and gas density is; to increase the detection field strength (signal intensity would increase linearly with B_0), to increase the isotopic enrichment of the gas used, increase the hp gas concentration, or to increase the polarization of the gas. Fig. 3.1 was acquired in a 9.4 T micro-imaging system. This is already a high field strength and significantly higher than the magnetic field strength of a typical medical imager (either 1.5 T or 3 T). Switching to a higher field strength imager would be costly and would only postpone the issue of MR signal intensity in the long run as high field human imaging systems (> 3 T) are not common.

One SEOP parameter that can be adjusted and examined is the concentration of noble gas used. The image in Fig. 3.1 used a mixture containing 25 % Kr. This concentration of Kr is unlikely to provide the highest possible spin-polarization, which would be achieved at lower noble gas densities. A higher concentration of noble gas is necessary because, unlike ^{129}Xe [4, 5], ^{83}Kr cannot be separated from optical pumping gas mixtures using cryogens, as ^{83}Kr has an extremely short T_1 in the frozen state [6, 7]. A consequence of not being able to separate out the hp gas is that it is desirable to use as high concentrations of noble gas isotope. It is therefore necessary to find the balance between noble gas concentration and achievable polarization that leads to the highest SNR.

The unfavourable effect that high concentration of noble gas isotopes have on spin-polarization is shown in Eq. 3.1. The spin destruction for the alkali metal electrons, described by the summation of the relevant rate coefficient (depending on the gas) and its corresponding number density $[M_i]$, is a limiting term in SEOP: this is multiplied by the gas specific rate coefficient κ_A^i. As discussed in **Chapter 2**, the rate coefficients of both Xe and Kr are both orders of magnitude larger than those of the other optical pumping mixture

constituents (N_2 and He) [8, 9]. Therefore spin destruction for the alkali metal electrons can be said to largely depend on noble gas density, [*NG*]. [*NG*] contributes to the total number density term $\sum[M_i]$ shown in Eq. 3.1, along with other number densities such as $[N_2]$ for the nitrogen.

$$P_{NG}(t) = \frac{\gamma_{SE}}{\gamma_{SE} + \Gamma_{NG}} \cdot \frac{\gamma_{OP}}{\gamma_{OP} + \gamma_{trap} + \gamma_{wdW} + \sum \kappa_A^i [M_i]} (1 - e^{-(\gamma_{SE} + \Gamma_{NG})t}) \qquad \text{[Eq. 3.1]}$$

γ_{vdW} is the term dealing with spin-destruction due to the spin-rotation interaction while part of a van der Waals complex. The γ_{trap} term deals with radiation trapping when Rb electrons relax back to their ground state. Both terms will be discussed in greater detail later.

It is known that optimal polarizations are achieved in mixtures with a low concentration of noble gas isotopes [8, 10] (Fig. 3.2a). This is because of the destructive term κ_A^i discussed above, but also because of the spin-exchange term, γ_{SE} that is adversely affected by high noble gas densities. The term γ_{SE} is given by Eq. 2.18 in **Chapter 2**. Higher noble gas densities make the formation of van der Waal complexes in the SEOP cell more difficult, as the presence of a greater number of large atoms makes collisions more frequent. This is more important for ^{129}Xe optical pumping compared to ^{83}Kr because the van der Waals spin exchange is less significant for the ^{83}Kr-Rb system that, even at lower pressures, is mostly driven by binary collisions.

A possible answer would be to optically pump below ambient pressure. This would allow the percentage of noble gas isotopes in a mixture to be high but also keep [*NG*] low (Fig. 3.2c).

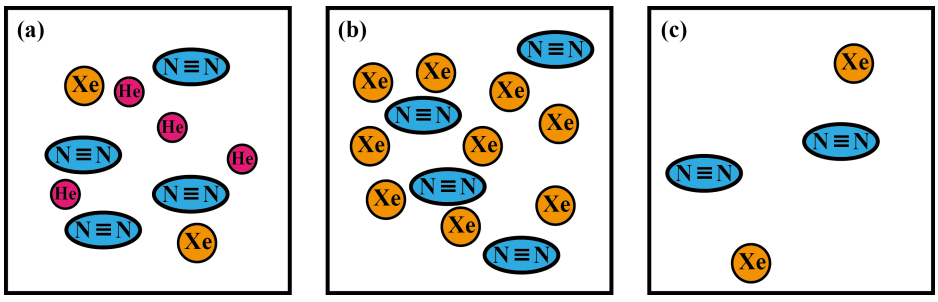

Fig. 3.2 *– **(a)** Mixture with low noble gas concentration. This gives good polarization but the gas needs to be separated. **(b)** High noble gas concentration mixture. Little separation of the gas is needed however the polarization is poor. **(c)** High noble gas concentration mixture at low pressure. Good polarization is achieved, and the gas requires little to no separation. Gas needs to be recompressed to atmospheric pressure before being useable in a clinical study.*

Imai *et al.* have previously explored SEOP at low pressures with ^{129}Xe [11], observing that at low pressures high ^{129}Xe polarization could be achieved (> 12%) at high Xe concentrations. This was using a low Xe concentration mixture, making the separation of the gas a prudent step to obtain the highest potential signal intensity. Imai *et al.* also proved the viability of recompressing a low-pressure gas mixture to ambient pressure with little loss in SNR (as low as 10%). Compressing hp ^{129}Xe was also previous demonstrated by Rosen *et al.* [12].

This method produced a small quantity of hp gas; Imai *et al.* admit that their system is unsuitable for large-scale hp gas production. Imai *et al.* explored both continuous flow and batch mode hp gas production. The continuous flow method was explored for a verity of flow rates; as an example, the maximum explored flow rate was 100 ml/min (0.1 l/min) achieving a polarization of 63 %, however this was only with a 1 % ^{129}Xe mixture. It was shown that at higher Xe concentrations, at a 0.1 l/min flow rate, polarizations were significantly lower (34 % for a 5 % Xe mixture) [11]. Given cryogenic accumulation at the high flow rate (0.1 l/min) the system would only produce 0.3 l/h of Xe.

In contrast Ruset *et al.* have developed a large-scale polarizer that takes advantage of low-concentration hp gas mixtures to produce highly polarized hp Xe in high quantities [13]. Operating their system at around 70 kPa, and freezing out the Xe from the hp gas mixture, polarizations as high as 0.3 l/h are reported. The system is capable of producing as much as 6 l/h, with a reduced polarization of 22 %.

This work explores low pressure optical pumping of ^{129}Xe in high [*NG*] mixtures using a line-narrowed diode laser, with a FWHM of 0.25 nm. The laser used by Imai *et al.* was not line-narrowed. It is likely that the rubidium D_1 transition line was significantly narrower than the laser line width at low pressures, as higher pressures are usually used to broaden this transition [14]. This would result in not all of the laser light exciting the transition and lowering the efficiency of the SEOP. At this stage this system will not be capable of generating the large quantities hp gas, but lays the groundwork for a larger system in the future.

This study will also explore ^{83}Kr SEOP in high [*NG*] mixtures at low pressures. In this case a means to generate highly polarized ^{83}Kr in high concentration mixtures is vital for continuing studies. Various gas mixtures comprising of nitrogen and different concentrations of noble gas (either ^{129}Xe or ^{83}Kr) will be examined.

3.2 Experimental methods and procedures

3.2.1 Optical pumping of noble gas

Both ^{129}Xe and ^{83}Kr were hyperpolarized using batch-mode Rb-SEOP. Circularly polarized light of 23.3 W power irradiated the SEOP cell (length = 120 mm, inner diameter = 28 mm, volume ≈ 75 cm^3) and was generated by a spectrally narrow (0.25 nm line width) diode array laser system (30 W Comet Module, Spectral Physics, Santa Clara, CA, USA). The laser was tuned to 794.7 nm, the D_1 transition of Rb. A spectrum showing the linewidth of the Rb absorption was recorded using an optical spectrometer (HR2000+, Ocean Optics, Dunedin, Florida, USA). As the D_1 transition is pressure dependant the absorption for a range of pressures (9 kPa – 434 kPa) have been recorded.

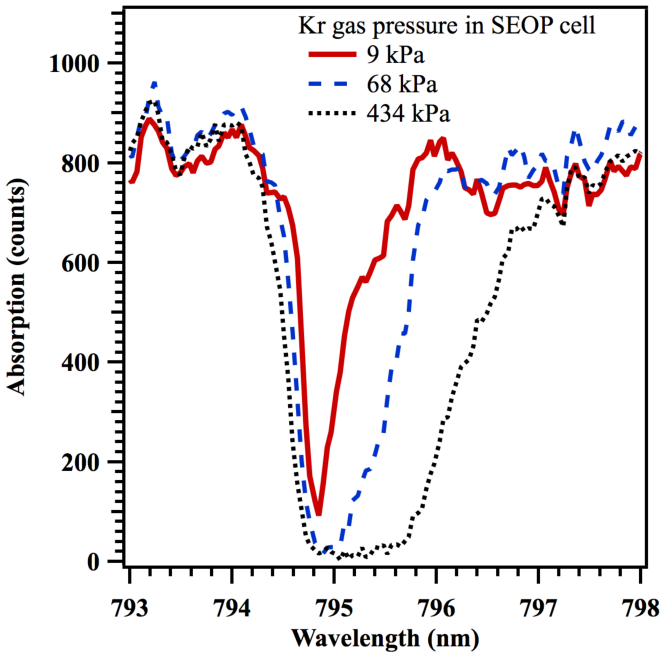

Fig. 3.3 *– Rb absorption linewidth for the D_1 transition. The absorption has been shown in the presences of Kr gas at three different pressures, showing both the effect of pressure broadening and a small shift in wavelength.*

The optical assembly used in these experiments is shown in Fig. 3.4.

SEOP cell pressure was monitored using a pressure transducer between the gas mixture and the SEOP cell, with the valve to the cell being closed approximately two minutes before gas delivery. A gas regulator on the gas tank was used to regulate gas pressures.

3.2.2 Temperature control

The SEOP cell temperature was maintained using a single inlet of heated air into an aluminium oven with quartz windows on either end. Thermocouples were placed at two points on the cell (by the inlet and outlet, see Fig 3.4a). A temperature controller read in the thermocouple values and would increase or decrease the temperature of the air accordingly so that a constant temperature

was maintained. This caused temperatures to vary by up to 5 K over the course of experiments. Typical temperature differences between the thermocouple at the front and back of the SEOP cell were about 10 K, with the higher temperature favouring the side that the laser entered on. Values recorded are of the surface temperature of the SEOP cell only; the internal temperature in the cell was unknown. Unless otherwise specified, SEOP was conducted at 373 K or 433 K for ^{129}Xe and ^{83}Kr respectively.

Temperatures for SEOP using ^{129}Xe were determined experimentally. Optical pumping was conducted over a range of pressures (0.1 kPa – 2.1 kPa) and temperatures (348 K – 398 K). Crude experiments were run before this to get a rough idea of an appropriate range.

Temperature for ^{83}Kr experiments was not explored in depth. The chosen value of 373 K was used as it was close to the value previously used for ^{83}Kr studies (438 ± 5 K [15]).

3.2.3 Gas delivery

Steady state polarization is the state when leaving the gas mixture in the SEOP cell for additional time does not increase the polarization level; this level is known as the maximum polarization, as the polarization will not increase beyond this level without changes to other optical pumping parameters.

For this system steady state polarization was achievable after 6 minutes for ^{129}Xe and 18 minutes for ^{83}Kr. Due to time constraints an optical pumping time of 8 minutes was used for ^{83}Kr, resulting in a polarization 80 % of that of the maximum. This was checked across the appropriate pressure range.

Pressure equalization rapidly transferred the gas into an evacuated 15 mm radius, glass detection cell inside a 9.4 T superconducting magnet (Oxford instruments; Kea 2 spectrometer, Magritek, New Zealand). A pressure transducer after the detection cell was used to determine the pressure. Two custom-built 15 mm probes were used to collect NMR spectra tuned to 110.6 MHz and 15.4 MHz for ^{129}Xe and ^{83}Kr respectively.

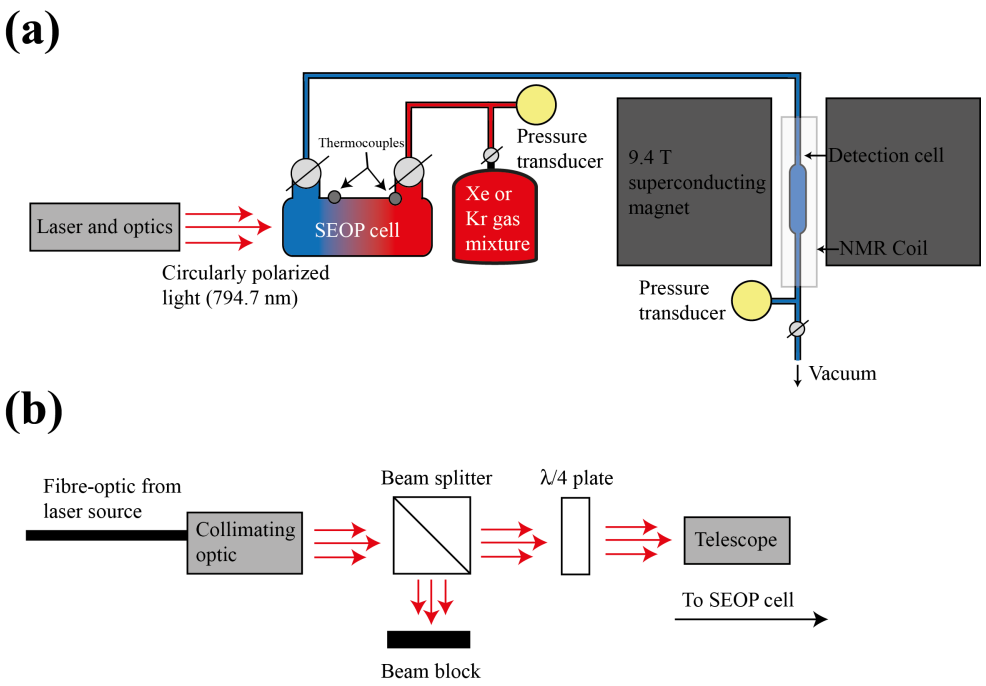

Fig. 3.4 *– **(a)** A typical SEOP set-up. Gas was let into the SEOP cell at a desired pressure and after a given time (typically two minutes before the end of the SEOP cycle) the gas inlet to the SEOP cell was closed. Circularly polarized laser light (tuned to 794.7 nm) was used to excite the outer electrons of the vapour-phase Rb in the cell. Once hyperpolarized, hp gas was vacuum shuttled into an evacuated detection cell inside a 9.4 T superconducting magnet. **(b)** Typical optical set-up for SEOP. Laser light was transferred from the laser source down a fibre-optical cable into collimating optics. It then travelled into a beam splitter were the longitudinal portion of the light (approximately 5%) was separated and discarded. The remaining light then travelled through a quarter-wave plate where it was circularly polarized. Finally the collimated beam was expanded to the size of the SEOP cell (32 mm diameter) before reaching the cell.*

3.2.4 Gas mixtures

Gas mixtures were prepared prior to SEOP experiments using a custom built stainless-steel mixing system. Bottles for gas mixture storage were flushed with N_2 three times and evacuated for over twelve hours before use.

Research grade Xe (99.995% natural abundance, 26.4% ^{129}Xe; Airgas, Rednor, USA), Kr (99.995% natural abundance, 11.5% ^{83}Kr; Airgas, Rednor, USA), N_2 (99.999% pure; Air Liquide, Coleshill, UK), and He (99.999% pure; Air Liquide, Coleshill, UK) were used for the relevant gas mixtures.

3.2.5 Determining polarization values

Actual polarization values were obtained by comparing the integral of the single intensity of the collected hp gas MR signal with that of a thermally polarized sample of the corresponding gas.

Borosilicate glass sample tubes (o.d. = 15 mm, length = 147 mm), similar to the detection cell were used to store the thermal samples. The cells had a threaded head with a cap and an arm with a ground-glass connection; a valve on the threaded head could be used to isolate the volume of the cell from the ground-glass length. Cells were attached to a gas-mixing manifold, and evacuated and flushed with N_2 multiple times. The system was opened to a thermally polarized noble gas supply. For Kr the cell was pressurized to a known pressure and sealed off. For Xe the cell was filled with noble gas, sealed, and then the mixing system was evacuated and filled with a higher pressure of O_2. The cell was opened to this and the second pressure reading was recorded. From this it was possible to calculate the composition of the thermal sample.

For ^{129}Xe a 5 amagat (see Section 3.2.7 for amagat definition) thermal sample was made containing 400 kPa of Xe and 100 kPa of O_2. This was done to reduce the T_1 time to less than 5 second [16]. 120 acquisitions were taken and averaged. Eq. 3.2 was then used to compare the hp signal and thermal signal, accounting for factors such as concentration, pressure, and number of scans.

$$Polarization = \frac{\xi_{hp}}{\xi_{Therm}} \times Scans_{Therm} \times \frac{P_{Therm}}{(P_{hp} \times \%_{NG})} \Big/ SE \qquad \text{[Eq. 3.2]}$$

Where ξ_{hp} is the hyperpolarized signal intensity, ξ_{Therm} is the thermal signal intensity, $Scans_{Therm}$ is the number of thermal scans taken, P_{Therm} is the pressure of noble gas in the thermal sample, P_{hp} is the hyperpolarized gas delivery pressure, $\%_{NG}$ is the percentage of the hyperpolarized mixture made up of the noble gas, and SE is the spin-enhancement factor. The spin enhancement factor is 1121 for ^{129}Xe and 2206 for ^{83}Kr.

Similarly the hp ^{83}Kr signals were compared to a thermal sample pressurized to 560 kPa of Kr (T_1 around 1 minute for pure Kr). An average was taken of 360 scans. The same considerations for ^{129}Xe were taken into account when comparing the hp Kr and thermal Kr signals.

3.2.6 Determining polarization accuracy

Various factors can influence the polarization values obtained from a given SEOP cell. This includes variation due to fluctuations in the cell temperature, contamination, and the distribution of Rb plating on the cells surface. In order

to characterize fluctuations in polarization over time and between SEOP cells a standard mixture (5 % Xe, 5 % N_2, 90 % He at 230 ± 20 kPa and 373 K) was intermittently used to collect polarization values so that one set of data, under a given set of conditions, could be better compared to others. Over a few experiments this value was measured as 44 ± 5 %. This was used as a quality control for a SEOP cell. If the polarization when tested fell outside of this range then the cell was discarded. The experimental error on the standard mixture was obtained by taking multiple polarization readings and then calculating a standard deviation. Multiple readings were not taken for other polarizations: Therefore errors on polarization measurements are given as ± 5 % error of the standard mixture scaled accordingly.

3.2.7 Amagat definition

It should be noted that in this thesis the number density of gas phase atoms, amagat, is defined as being the density of an ideal gas at standard temperature and pressure (101.325 kPa and 273.15 K respectively). This is not the historic definition where it is the density of a specific gas.

3.3 Results

3.3.1 Apparent polarization

The method described by this work produces noble gas mixtures that are diluted with N_2. As no cryogenic separation is employed, it is difficult to directly compare the signal obtainable from this polarized gas compared to gas that has been separated leaving only noble gas. A pressure range of 0.04 kPa to 3.3 kPa was investigated, using gas mixtures containing as little as 5 % noble gas up to 78 % noble gas.

An apparent polarization, P_{APP}, will be defined as the polarization, P, scaled to the equivalent amount of pure noble gas need to produce the same signal intensity (Eq. 3.3 [1]).

$$P_{APP} = P \cdot \frac{[NG]}{\sum_i [M_i]} \approx P \cdot \frac{p_{NG}}{p_{Total}}$$

[Eq. 3.3]

Where $[NG]$ is the noble gas density, $\sum_i [M_i]$ is the sum of all of the gas densities, p_{NG} is the pressure of noble gas, and p_{Total} is the total gas pressure.

3.3.2 Noble gas apparent polarization as a function of SEOP gas pressure

Fig. 3.5a shows apparent polarization for four different mixtures containing ^{83}Kr as a function of SEOP cell pressure (in kPa). Fig. 3.5b shows the apparent polarization for five different gas mixtures containing ^{129}Xe as a function of SEOP cell pressure (in kPa).

Polarization values are shown to increase with the decrease in pressure for all mixtures studied until reaching the sub-55 kPa range. The maximum apparent polarization, P_{APP}^{MAX}, was observed in the 35 – 50 kPa region for mixtures containing ^{83}Kr and the 20 – 35 kPa region for mixtures containing ^{129}Xe. P_{APP}^{MAX} and corresponding optimal pressures p^{MAX} are shown in Table 3.1. Reducing pressure after the maximum polarization was reached caused a rapid drop in polarizations. The reason for the rapid drop in polarization at these pressures will be discussed later.

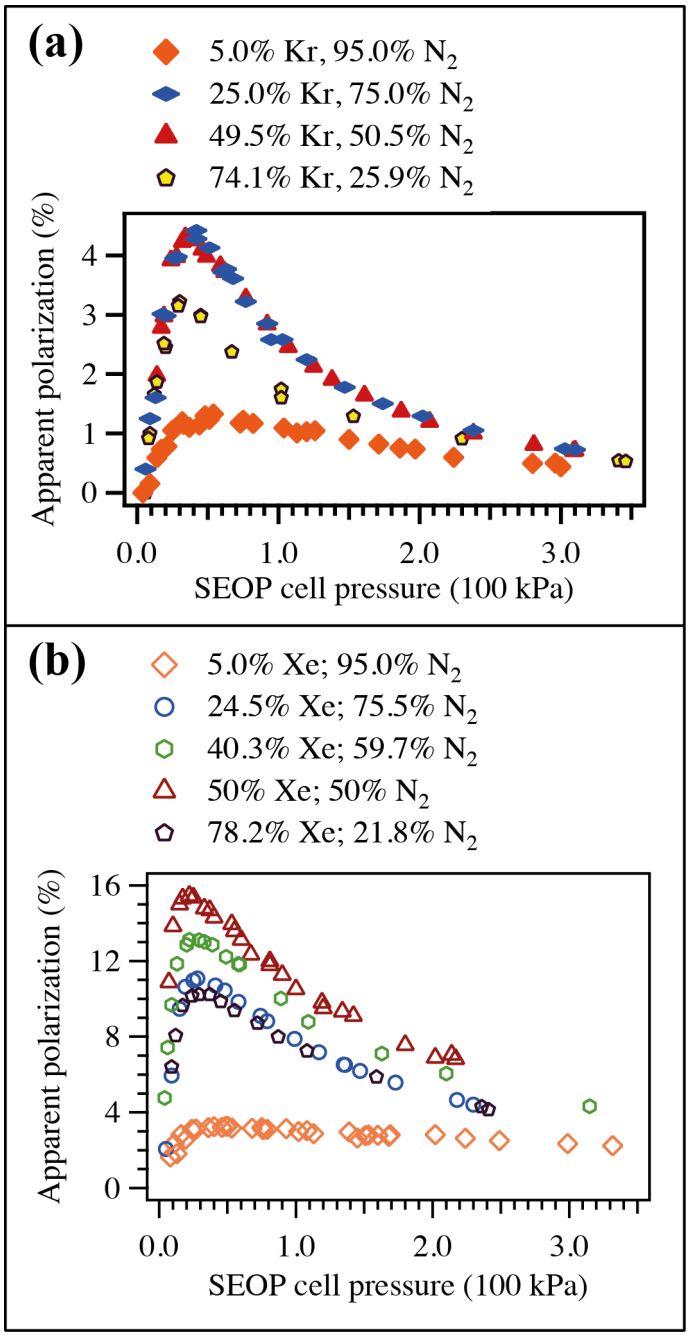

Fig. 3.5 *– **(a)** ^{83}Kr apparent polarizations as a function of SEOP cell pressure (in kPa). Data for four different gas mixtures are shown. The data shows that mixtures with moderate concentrations of Kr (25 % and 50 %) allow for the greatest apparent polarizations to be achieved. Polarizations are shown to be at a maximum in the 35 – 50 kPa range for all mixtures. **(b)** ^{129}Xe apparent polarization as a function of SEOP cell pressure (in kPa). Data for five different gas mixtures are shown. The data shows that mixtures with moderate concentrations of Xe (40 % and 50 %) allow for the greatest apparent polarizations to be achieved. Apparent polarizations are shown to be at a maximum in the 20 – 50 kPa range for all mixtures. ^{129}Xe apparent polarizations are shown to typically be higher than ^{83}Kr polarizations.*

The greatest apparent polarizations are seen with 50.0% Xe, 50.0% N_2 for ^{129}Xe and 25.0% Kr, 75.0% N_2 for ^{83}Kr.

Mixture composition	***Apparent maximum polarization*** P_{APP}^{MAX} (%)	SEOP cell pressure at maximum final polarization p_{APP}^{MAX} (100 kPa)	**Maximum polarization** P^{MAX} **(%)**
5.0 Kr; 95.0 N_2	1.3 ± 0.2	0.54	26.5 ± 3.3
25.0 Kr; 75.0 N_2	**4.4 ± 0.5**	**0.42**	**17.7 ± 2.2**
49.5 Kr; 50.5 N_2	4.3 ± 0.5	0.41	8.6 ± 1.1
74.1 Kr; 25.9 N_2	3.2 ± 0.4	0.30	4.3 ± 0.5
5.0 Xe; 95.0 N_2	3.2 ± 0.4	0.46	64.7 ± 8.0
24.5 Xe; 75.5 N_2	11.1 ± 1.4	0.28	45.2 ± 5.6
40.3 Xe; 59.7 N_2	13.1 ± 1.6	0.22	32.5 ± 4.0
50.0 Xe; 50.0 N_2	**15.5 ± 1.9**	**0.22**	**30.1 ± 3.8**
78.2 Xe; 21.8 N_2	10.2 ± 1.3	0.37	13.1 ± 1.6

Table 3.1 *– Table displaying values maximum apparent polarization, optimal pressure for SEOP, and maximum polarization for the 9 gas mixtures. Greatest apparent polarizations are seen with 25.0 % Kr, 75.0 % N_2 for ^{83}Kr and 50.0 % Xe, 50.0 % N_2 for ^{129}Xe.*

3.3.3 A brief analysis of the pressure dependence of polarization at high pressures

It is beyond the scope of this commentary to fully analyze the pressure dependant polarization relationship observed in this work, a more comprehensive evaluation was conducted by Joseph S. Six and is available in the literature [1]. For the sake of completeness an overview of some of the major contributing factors will be discussed here.

Looking at Eq. 3.1, it can be observed that there is density dependence in the $\sum_i \kappa_{sd}^i [M_i]$ term. This represents part of the spin-destruction experienced of the alkali metal electrons. For the most part the spin-destruction due to noble gas will be far larger than spin destruction from N_2 or He due to the higher rate coefficients (about a factor of 1000; see **Section 2.1.3**).

Under normal optical pumping conditions Rb-Rb spin-destruction can also be negated. While the rate coefficient is high ($\kappa_{Rb} \approx 8.1\times10^{-19}$ m^3s^{-1}) [17] compared to ^{129}Xe and ^{83}Kr ($\kappa_{Xe} \approx 5.2\times10^{-21}$ m^3s^{-1} and $\kappa_{Kr} \approx 1.1\times10^{-21}$ m^3s^{-1}) [8], gas pressures are typically far higher than Rb vapour pressures.

While Rb-Rb relaxation will not contribute heavily to polarizer efficiency under most circumstances due to the small [*Rb*] term, it will contribute under

some conditions when ^{83}Kr is used. Typical SEOP cell temperatures are at the higher temperature of 433 K for ^{83}Kr. As [*Rb*] is a function of temperature [18, 19] this means that more Rb will be in the vapour phase during ^{83}Kr polarization. Additionally, Kr-Rb relaxation is about a factor of 5 less prominent than Xe-Rb relaxation due to the different rate coefficients.

There was also a major additional consideration for the ^{129}Xe polarization relationship. Fig. 3.3 shows the Rb D_1 absorption line width in the presence of Kr gas at various pressures, and Fig. 3.6 shows an absorption line in the presence of Kr compared to an absorption line in the presence of N_2 at similar pressures: Note that the line broadening in the presence of N_2 is less than in the presence of Kr. In the presence of Xe and Xe + N_2 mixtures broadening was seen to be even less. Under all optical pumping conditions experienced for Kr mixtures the Rb absorption line was observed to be broader than the laser linewidth (0.25 nm); this was not true for all Xe mixtures. At low pressures, and in Xe heavy mixtures the laser linewidth was greater than the D_1 transition meaning that not all of the laser light would be absorbed. This loss of photons reduced the efficiency of the optical pumping.

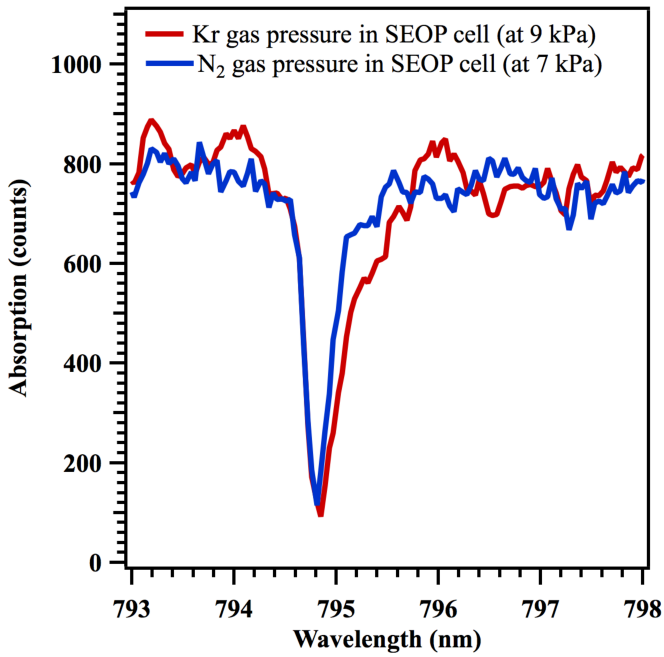

Fig. 3.6 *– Rb absorption linewidth for the D_1 transition. The absorptions have been shown in the presences of N_2 and Kr gas at a similar pressure. Note that the line broadening for Kr is greater than for N_2.*

3.3.4 Considerations for polarization as a function of pressure at lower pressures

Helium is often included in optical pumping mixtures to induce pressure dependent broadening of the D_1 transition. As pressure broadening was not desired in these experiments (due to the use of a narrow-band laser) two gas mixtures including ^{4}He and ^{129}Xe were examined at low pressures. Apparent polarization as a function of SEOP cell pressure (in kPa) is shown in Fig. 3.7.

Gas mixtures with ^{4}He reach their maximum polarization at a higher pressure than those containing greater concentrations of N_2. For example, the maximum polarization for the 48.3% Xe mixture (containing He) is roughly achieved just below ambient pressure; polarization then begins to drop when the SEOP cell pressure is less than 30 kPa.

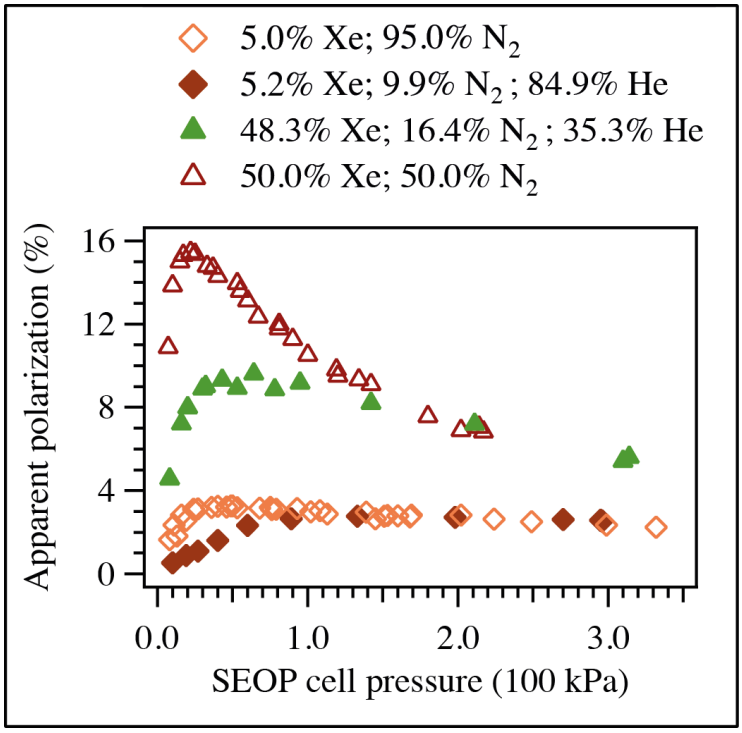

Fig. 3.7 *– ^{129}Xe apparent polarization as a function of SEOP cell pressure (in kPa). Data for four different gas mixtures are shown (two are repeated from Fig. 3.4b as a comparison). Gas mixtures with ^{4}He reach their maximum polarization at higher pressures than those with higher concentrations of N_2.*

3.3.4.1 Drop in polarization below a critical pressure

To explain this rapid drop in polarization, as well as the drop in polarization seen for other mixtures shown in Fig 3.5, florescence must be examined. As discussed in **Section 2.1.3** florescence occurs in a high Rb environment: Optically pumped Rb electrons in the ^{5}P energy level relax back to the ^{5}S level via a radiative emission. This photon is randomly polarized and will be detrimental to the optical pumping of the Rb if the polarization is not the same as the laser light. This is a cumulative effect as the photon may be absorbed by another Rb atom, ultimately leading to the emission of another randomly polarized photon. This is known as radiation trapping and is included in Eq. 3.1 using the term γ_{trap}.

Radiative emissions can be absorbed by N_2. N_2 has a triple bond so when stray radiative emissions are absorbed the energy can be dissipated through the vibrational levels of the molecule [17]. The likelihood of this mode being

chosen is dependent on the D_1 quenching cross section, and therefore is proportional to $[N_2]$.

There will be no florescence when there is adequate N_2 density in the SEOP cell.

D_2 line florescence was observed with an optical spectrometer (HR2000+, Ocean Optics, Dunedin, Florida, USA) as the D_1 florescence (responsible for the Rb relaxation) was obscured by the laser. D_2 florescence should correlate well with the D_1 florescence. D_2 florescence was relatively low under SEOP conditions for the various mixtures up until pressures just before the polarization drops.

Dropping the pressure from this point resulted in the florescence increasing dramatically. This was due to an inadequate N_2 density. It was for this reason that mixtures containing ^{4}He, and therefore far less N_2, reached their maximum polarization at higher pressures than N_2 rich mixtures. By observing the fluorescence of other mixtures it was determined that inadequate N_2 density was a major contributing factor to the polarization drop at very low pressures. This was found by fitting the data and exploring additional terms from Eq. 3.1. This determination is not presented here but is available in the literature [1].

While florescence from inadequate $[N_2]$ is one reason for the polarization drop, other factors do contribute. The work of Wagshul and Chupp is a good source to identify these [17]. Their work shows two other potential reasons for a polarization drop. The first is that excited Rb is optically dense. This might have resulted in an optically dense layer of Rb existing at the front of the SEOP cell, preventing adequate excitation of the Rb further back. Wagshul and Chupp offer a solution, which is to slightly detune the laser, their work showing that this detuning can result in high Rb polarization [17]. This in combination with the method described here might be of interest to future researchers continuing this work.

The increase in the diffusion of the Rb vapour at low pressures may also have been detrimental to Rb polarization. An increased diffusion would result in the Rb coming into more frequent contact with the SEOP cell walls, resulting in greater relaxation: This was observed in low-pressure N_2 by Wagshul and Chupp [17].

A final contributing factor, primarily for ^{129}Xe, may be the depolarization due to van der Waal complexes at lower pressures. While the brief formation of van der Waal complexes is a means of spin-exchange, these formations are only fleeting. Longer lifetime complexes will exist in an environment where collisions are less likely to occur, and depolarization may occur.

3.4 Conclusions

Production of high noble gas concentration hp gas, with high apparent polarizations has been demonstrated using both ^{83}Kr and ^{129}Xe. This paves the way for production of hp ^{83}Kr and ^{129}Xe for practical NMR and MRI applications without the need for cryogenic separation. Apparent polarization of P_{APP}^{MAX} = 4.4 ± 0.5 % is possible with^{83}Kr, producing 2.2 cm^3/min of hp gas. P_{APP}^{MAX} = 15.9 ± 1.6 % is achievable with ^{129}Xe at a rate of 1.8 cm^3/min. Given values are for 80 % of the maximum polarization and steady-state polarization respectively and therefore greater quantities of gas can be produced at the cost of some polarization. Higher quantities may be achieved by up scaling the SEOP cell used providing that laser power is also increased. This will be a necessary step in order to use this SEOP technique for large animal *in vivo* or human studies. Some of the essential considerations will be discussed in **Section 4.5.1**.

In order to make this method viable without cryogenic separation then recompression of the gas is vital. Imai *et al.* have demonstrated that the recompression of ^{129}Xe is possible with the use of a diaphragm pump without major losses to polarization [11]. Continuing work explores recompression further and is discussed in **Chapter 4**.

Data presented have been given a brief qualitative explanation. A far more in-depth theoretical analysis, along with additional experiments, were conducted prior to publication [1]. This has not been included in this thesis as the additional experiments and data analysis were conducted by Joseph Six (the first author of the publication).

3.5 References

[1] J.S. Six, T. Hughes-Riley, K.F. Stupic, G.E. Pavlovskaya, T. Meersmann, Pathway to Cryogen Free Production of Hyperpolarized Krypton-83 and Xenon-129, PLOS ONE, 7 (2012) e49927.
[2] Z.I. Cleveland, G.E. Pavlovskaya, N.D. Elkins, K.F. Stupic, J.E. Repine, T. Meersmann, Hyperpolarized Kr-83 MRI of lungs, Journal of Magnetic Resonance, 195 (2008) 232-237.
[3] K.F. Stupic, Z.I. Cleveland, G.E. Pavlovskaya, T. Meersmann, Hyperpolarized Xe-131 NMR spectroscopy, Journal of Magnetic Resonance, 208 (2011) 58-69.
[4] N.N. Kuzma, B. Patton, K. Raman, W. Happer, Fast nuclear spin relaxation in hyperpolarized solid Xe-129, Physical Review Letters, 88 (2002) 147602.
[5] G. Schrank, Z. Ma, A. Schoeck, B. Saam, Characterization of a low-pressure high-capacity 129Xe flow-through polarizer, Physical Review A, 80 (2009) 063424.
[6] D.F. Cowgill, R.E. Norberg, Pulsed Nmr-Studies of Self-Diffusion and Defect Structure in Liquid and Solid Krypton, Physical Review B, 13 (1976) 2773-2781.

[7] D.F. Cowgill, R.E. Norberg, Spin-Lattice Relaxation and Chemical-Shift of Kr-83 in Solid and Liquid Krypton, Physical Review B, 8 (1973) 4966-4974.
[8] M.A. Bouchiat, J. Brossel, L.C. Pottier, Evidence for Rb Rare-Gas Molecules from Relaxation of Polarized Rb-Atoms in a Rare-Gas - Experimental Results, Journal of Chemical Physics, 56 (1972) 3703-3714.
[9] M.E. Wagshul, T.E. Chupp, Laser Optical-Pumping of High-Density Rb in Polarized He-3 Targets, Physical Review A, 49 (1994) 3854-3869.
[10] W. Happer, Optical-Pumping, Reviews of Modern Physics, 44 (1972) 169-249.
[11] H. Imai, J. Fukutomi, A. Kimura, H. Fujiwara, Effect of reduced pressure on the polarization of Xe-129 in the production of hyperpolarized Xe-129 gas: Development of a simple continuous flow mode hyperpolarizing system working at pressures as low as 0.15 atm, Concepts in Magnetic Resonance Part B-Magnetic Resonance Engineering, 33B (2008) 192-200.
[12] M.S. Rosen, T.E. Chupp, K.P. Coulter, R.C. Welsh, S.D. Swanson, Polarized Xe-129 optical pumping/spin exchange and delivery system for magnetic resonance spectroscopy and imaging studies, Review of Scientific Instruments, 70 (1999) 1546-1552.
[13] I.C. Ruset, S. Ketel, F.W. Hersman, Optical pumping system design for large production of hyperpolarized Xe-129, Physical Review Letters, 96 (2006) 053002.
[14] M.V. Romalis, E. Miron, G.D. Cates, Pressure broadening of Rb D-1 and D-2 lines by He-3, He-4, N-2, and Xe: Line cores and near wings, Physical Review A, 56 (1997) 4569-4578.
[15] Z.I. Cleveland, T. Meersmann, Binary-collision-induced longitudinal relaxation in gas-phase Kr-83, Journal of Chemical Physics, 129 (2008) 244304.
[16] C.J. Jameson, A.K. Jameson, J.K. Hwang, Nuclear-Spin Relaxation by Intermolecular Magnetic Dipole Coupling in the Gas-Phase - Xe-129 in Oxygen, Journal of Chemical Physics, 89 (1988) 4074-4081.
[17] M.E. Wagshul, T.E. Chupp, Optical-Pumping of High-Density Rb with a Broad-Band Dye-Laser and Gaalas Diode-Laser Arrays - Application to He-3 Polarization, Physical Review A, 40 (1989) 4447-4454.
[18] T.J. Killian, Thermionic phenomena caused by vapors of rubidium and potassium, Physical Review, 27 (1926) 578-587.
[19] C.B. Alcock, V.P. Itkin, M.K. Horrigan, Vapor-Pressure Equations for the Metallic Elements - 298-2500-K, Canadian Metallurgical Quarterly, 23 (1984) 309-313.

Chapter 4

Extraction and compression of low pressure hyperpolarized gases

Acknowledgements

The work presented in this chapter contains a combination of material used for two published articles. *Cryogenics free production of hyperpolarized ^{129}Xe and ^{83}Kr for biomedical MRI applications* was published in the Journal of Magnetic Resonance [1]. The author list was **Theodore Hughes-Riley**, Joseph S. Six, David M.L. Lilburn, Karl F. Stupic, Alan C. Dorkes, Dominick E. Shaw, Galina E. Pavlovskaya, and Thomas Meersmann.

The second publication was *Pulmonary MRI contrast using Surface Quadrupolar Relaxation (SQUARE) of hyperpolarized ^{83}Kr* and was published in Magnetic Resonance Imaging [2]. The author list consisted of Joseph S. Six, **Theodore Hughes-Riley**, David M.L. Lilburn, Alan C. Dorkes, Karl F. Stupic, Dominick E. Shaw, Peter G. Morris Ian P. Hall, Galina E. Pavlovskaya, and Thomas Meersmann.

This work presents two out of four compression units investigated. Dr. Karl F. Stupic primarily designed the balloon extraction-compression device, its forerunner, and a compression device that used a moving column of water. The piston extraction-compression device was designed by Theodore Hughes-Riley with input from Prof. Thomas Meersmann and Mr. Alan C. Dorkes. This design was chosen after an extensive literature search (also by Theodore Hughes-Riley). Mr. Alan C. Dorkes fabricated compression devices.

The exaction-compression gas delivery methodology used and presented in this work was devised by Theodore Hughes-Riley; in the case of the balloon extraction-compression unit this was based on preliminary experiments conducted by Theodore Hughes-Riley, Joseph S. Six, and Dr. Karl F. Stupic.

The MR spectroscopy experiments conducted and presented in this work were preformed by Theodore Hughes-Riley under the guidance of Prof. Thomas Meersmann. These experiments sometimes required a second person to run the spectrometer, in which case Joseph S. Six or Dr. David M.L. Lilburn would assist. Theodore Hughes-Riley prepared the figures in this chapter.

Imaging experiments required three people to run (these being Theodore Hughes-Riley, Joseph S. Six and Dr. David M.L. Lilburn). Dr. David M.L. Lilburn was responsible for lung extractions (assisted by Theodore Hughes-Riley). Typically Theodore Hughes-Riley would run the gas delivery system, Joseph S. Six would be responsible for the polarizer, and Dr. David M.L. Lilburn would run the spectrometer (using a sequence written by Dr. Galina E. Pavlovskaya) and process the image, although jobs were occasionally exchanged.

4.1 Introduction and background

Hyperpolarization of ^{83}Kr and ^{129}Xe via SEOP at low pressures has been seen to be a valid and useful technique to obtain highly polarized hp mixtures with a high content of noble gas [3]. This process has the advantage of eliminating the need for cryogens used in a typical ^{129}Xe SEOP set-up; where a dilute noble gas mixture is used and the hp ^{129}Xe is cryogenic separated from the other gases before being used [4, 5]. Removing the freeze/thaw cycle is desirable when working in a typical clinical setting where access to cryogens or suitably trained staff may not be available.

Rapid quadrupolar-driven T_1 relaxation in the frozen state [6, 7] prevents the separation of Kr from other gases in this manner without substantial loses in polarization. Therefore low-pressure SEOP is essential for the production on high-polarization, high noble gas concentration mixtures for MRI studies.

A vital step in order to be able to use low-pressure hp gas in lung studies is to be able to extract as much gas as possible from the SEOP cell, and then compress it so that the gas can be delivered at ambient pressure. This has previously been demonstrated for ^{129}Xe by Imai *et al.* [8] using a diaphragm pump and batch mode SEOP, where only minimal losses in the SNR (as low as 10%) were observed.

A number of compression techniques have been heavily utilized by groups using metastability-exchange optical pumping (MEOP) with ^{3}He, as the low pressure regime produce optimal polarization with this method [9]. A literature review of previous work in this area will be detailed in **Section 4.2**.

This work utilizes two bespoke extraction-compression systems. The systems were manufactured in-house from low cost materials and is significantly simpler (and presumably cheaper) than recompression systems used for ^{3}He presented in the literature [10-16], were ultra-high vacuum conditions are usually required. Methods for recompressing hp gas mixtures have been described: These techniques have been applied to a mixture containing ^{83}Kr. The extraction-compression process has been demonstrated with 24.8 % Kr and 75.2 % N_2 gas mixture over a range of pressures of interest. For the most suitable technique, at the optimal SEOP cell pressure (49 kPa) 85 % of polarization survives the extraction-compression process leading to an apparent polarization of 2.9 ± 0.0 %.

The extraction-compression techniques described were also shown to be a valid method for a variety of Xe containing mixtures over a range of SEOP cell pressures. For a 39.6 % Xe, 60.4 % N_2 mixture this method led to an insignificant drop in polarization at SEOP cell pressure exceeding an atmosphere, and a survival of 95 % of the polarization at the optimal SEOP cell pressure, leading to an apparent polarization of 14.0 ± 0.2 %.

Images using recompressed hp ^{129}Xe with a 370 x 470 μm resolution in excised rat lungs have been presented. Images using both naturally abundant and isotopically enriched Xe are shown. Structural details of the lung, such as the

major airways, are apparent. The improved image clarity due to higher polarizations achieved using the low pressure optical pumping method is noticeable.

Coronal images using recompressed hp ^{83}Kr have also been presented. Images have been collected using mixtures including both naturally abundant quantities of the ^{83}Kr isotopes, as well as mixtures included isotopically enriched ^{83}Kr (en ^{83}Kr). All images clearly show structural features of the lung. Enriched ^{83}Kr imaging has allowed for slice selective images to be acquired, and for the first time spatially resolved T_1 contrast in the lung.

4.2 Hyperpolarized gas compression in the literature

Previous work has investigated the compression of hyperpolarized noble gases, most of which relates to the compression of low-pressure hp ^{3}He generated by Metastable Exchange Optical Pumping (MEOP).

The first example of polarized noble gas compression comes from Timsit *et al.* who developed a means to compress ^{3}He [12]. A Toepler pump was constructed from aluminosilicate glass with liquid mercury used as the moving column. The height of the mercury in the pump was controlled by pressurized argon gas.

MEOP was conducted at about 130 Pa (1 Torr) achieving a polarization of 4 % prior to compression. Gas was compressed into a storage cell over multiple ^{3}He excitations. Once compressed to near 13 kPa polarization remained at around 4 %. Polarization was checked again once the gas was compressed to 29 kPa, here it had dropped to 3 %. This is attributed to relaxation in the storage cell, as some gas would have been in the cell for 4 hours at this point. High pressures were not achieved as fatigue caused the pump to break after this point.

The entire apparatus was surrounded by a uniform magnetic field of a few gauss.

A similar compressor was replicated by Eckert and coworkers [17]. The compressor apparatus was constructed from Pyrex with moving column of mercury. The final storage cell was made from Supermax glass (aluminosilicate glass) with contained hp ^{3}He having a T_1 time of 3.5 h. The ^{3}He should have had a far higher T_1 in the cell; the authors speculate that this was either due to magnetic impurities being pulled into the cell during the experiments, or simply a result of variations in the glass (^{3}He T_1 times have been seen to vary between 3 and 17 hours for cells constructed from the same Supermax glass). The apparatus was contained within a 10 G magnetic field.

A 1 L MEOP cell was used; at 130~260 Pa polarizations of 50 % could be achieved (pressures between 150 Pa and 240 Pa was maintained for the compression experiments).

Compression cycle times were limited to a minimum time of ~30 seconds. The turbulence of the mercury and formation of bubbles induced mechanical stresses on the compressor and there was concern that it would break. Compressor cycle times and the final target pressure was calibrated to allow for a low (minimally fluctuating) MEOP cell pressure.

A maximum polarization of 30 % in the 120 cm^3 storage cell, at 91 kPa was achieved after 2.5 hours. Polarization losses were identified as being due to a frit (i.e. a porous filter made of glass particles) that the hp ^{3}He had to pass through (the T_1 was estimated as being close to 1 s). Another potential source of relaxation was thought to be due to ferromagnetic impurities on the surface of the mercury. At the end of the compression cycle there would be a high surface-to-volume ratio, with the ferromagnetic impurities making up a larger percentage of the surface that the hp ^{3}He would be in contact with.

An improved system using a titanium piston was developed; however results were omitted from this paper, and was published later by Becker *et al.* [18]. Unlike the work preceding it Becker *et al.* utilized a pneumatically driven titanium piston to compress hp ^{3}He (again generated by MEOP). Losses of up to 80 % of the achievable polarization were observed leading to a thorough study of the potential causes of the relaxation. The compression chamber, storage cell (where NMR detection would occur), and the line between the two (the transfer region) were identified as the areas where relaxation might occur.

T_1 measurements were obtained and it was concluded that the large surface-to-volume ratios of the values in the transfer region were most detrimental to polarization. Further quantitative analysis showed that relaxation of gas moving towards the storage cell, after multiple compression cycles, accounted for 78 % losses. Some relaxation in the compression chamber and storage volume was also incurred.

Various pressures were examined during this study. Pressures in the optical pumping cell were measured from being just over 25 Pa to 200 Pa, however around 100 Pa was typically used.

The titanium piston was replicated by Surkau *et al.* [19]. In order to achieve the desired compression ratio Surkau *et al.* utilized two of these compressors in series with one another, creating a two-stage compressor. ^{3}He was polarized at ~100 Pa.

The system was held within an 80 G magnetic field. The field had a very small gradient, minimizing T_1 relaxation due to diffusion within the gradient. Polarization losses are not discussed in detail, instead referring to the work by Becker *et al.* [18] Polarization in the MEOP cell was reported as being 64 %. Polarization in a storage cell located after compression, at 100 kPa L, was reported as 53 %. Compression of up to at least 320 kPa was possible.

Later Heil *et al.* used two piston compressors [14] identical to that used by Becker *et al.* [18]. MEOP was conducted at 100 Pa and polarization within the MEOP cell was reported in the region of 72 – 74 %. For Heil *et al.*'s

application pressures exceeding 100 kPa were required. Polarization values between 50 – 60 % were observed when gas was compressed to between 90 kPa and 500 kPa.

Gentile *et al.* developed a design for a simple two-stage compressor based on a modified commercial diaphragm pump (KNF Neuberger Inc., New Jersey, USA) [10]. Modifications were made to the drive train of the compressor where magnetic components were replaced with bespoke non-magnetic parts. The compressor itself was motor-less and was driven be a DC motor attached by a shaft. The entire apparatus, with the exception of the motor, was confined within a uniform magnetic field generated by a Helmholtz pair.

The final outlet pressure of the compressor was 110 kPa. With the storage cell immersed in liquid N_2 this resulted in a storage cell pressure of 400 kPa at room temperature. MEOP was conducted at between 200 Pa, with the pressure rising during the filling of the storage cell to 600 Pa. This is because the outlet pressure of the second stage of the compressor increased over time (from zero to about 100 kPa). This was non-ideal for MEOP where the optimal pressure was about 100 Pa. The authors suggested that a third compression stage could mitigate some of this problem, however that would also reduce polarization due to increased relaxation.

Polarization after compression was recorded as 15 %. Almost a $1/3^{rd}$ loss of polarization after compression wa reported.

A later paper by Gentile *et al.* further detailed their two-stage diaphragm-pump compressor [11]. Various parameters were explored. It is noteworthy that the storage cell was located within a Helmholtz pair.

Relaxation in the system was identified as the cause of the polarization loss; it was desirable to reduce time in the compressor in order to minimize polarization losses. However, a fast flow reduced the time that the noble gas spends in the MEOP cell, leading to lower polarization. Gentile *et al.* calibrated the system so that about 75 % of the polarization survived between the MEOP cell and storage cell (this distance included the compressor).

Further polarization optimizations were also mentioned. The optimal pressure for MEOP was previous found to be 50 Pa, far lower than the 250 Pa used in the presented apparatus. The authors have previously identified that higher polarizations at this pressure can be achieved using ^{3}He-^{4}He optical pumping mixtures [20].

Gentile has a US patent relating to this system to compress polarized gas [21].

Hussey and co-worker built a two-stage compressor based on two titanium pistons [15]. The pistons were driven by a pneumatic drive cylinder.

Polarizations of about 71 % were typical at a 100 Pa MEOP cell pressure. However, when using the compressor the maximum polarization was ~65 %. Polarization losses due to the use of the compression system was seen to allow

an 81 % polarization survival; therefore a final compressed polarization of ~52 % should have been achievable.

The paper probed the relaxation values for ^{3}He in the various main components of the system and simulated the estimated polarization survival based solely of T_1 times. This gave a theoretical polarization survival limit of 83 %, suggesting that all polarization loss was indeed caused by relaxation. The author states the glass tubes connecting the compression systems components, that had a very high S/V ratio, were the main cause of T_1 relaxation in the system.

In a report by Snow [16] it is stated that the polarizer-compressor apparatus available at Indiana University (presumably a modified version of an apparatus described elsewhere [15]) that polarizations of 60 % were achieved in the MEOP cell(s) and that 87 % of polarization was retained after compression.

Another method to compress hp gas was described by Fichele [22] at the University of Nottingham, where the use of a two-roller peristaltic compressor was explored. While this design was able to compress the hyperpolarized ^{3}He there were limitations introduced by the compression ratio of the compressor. Further work by Mada [23] investigated a four-roller peristaltic pump that delivered a higher compression ratio. This did allow for greater acquired signal intensity, however this leveled off at 8 kPa. A subsequent experiment identified that a higher rate of compression and a storage cell that would allow for a greater relaxation time would be needed to acquire suitable levels of gas (both adequate polarization and quantity) for lung imaging, which was the purpose of this work. Ultimately the design was adapted into a two-stage compression system where the second stage employed a pneumatically driven piston. In its final configuration a bespoke piston (length = 150 mm, diameter = 70 mm) was employed. The peristaltic pump was used to fill a storage cell from the optical pumping cell, and the piston used to compress the gas from the storage cell into a bag for inhalation (with a final pressure of 35 kPa).

In a patent by Nacher the use of a peristaltic compressor is discussed further [24]. It was proposed that a flexible tube (or tubes) could be placed within a chamber that would be below atmospheric pressure. Another tube would be placed into a pressurized fluid. The tubes would then be placed over rollers attached to a peristaltic rotor. The pressure differential within the tube with pressurized fluid at one end would cause the rotor to rotate; the rotation would cause the flexible tubes to be compressed, resulting in the gas moving forward. In order to operate at the very low pressures required for typical MEOP it was proposed that the compressor could be operated in a vacuum chamber so that the pressure in hp gas tube would always be at an overpressure, preventing the tube(s) from collapsing.

Nacher speculated that this could have applications for other noble gases, in particular ^{129}Xe. He also highlighted that methods do exist that can allow MEOP at pressures between 1 – 10 kPa, and in these cases a lower compression factor would be required (which was reported in another patent; French Patent 2744932).

Compression has also been explored for hp ^{129}Xe generated by Rb-SEOP. Rosen *et al.* describe a polarizer and delivery system [25] previously used to obtain *in vivo* ^{129}Xe rat brain images [26]. Batch mode Rb-SEOP was conducted on a gas mixture of approximately 230 kPa Xe and 20 kPa N_2 (~92% Xe, ~8% N_2). Xe was cryo-accumulated (typically) over multiple cycles, where vacuum was used to remove the N_2.

After the desired number of cycles the accumulated Xe was expanded for delivery into a syringe-like cell. The outer cell was constructed with coated (octadecyltrichlorosilane) Pyrex. The cell contained a Teflon piston. One side of the cell was evacuated or filled with Xe, whereas the other side was evacuated or pressurized with N_2: The Teflon piston created a sufficiently gas tight seal with the Pyrex cell. The piston started at the back of the cell, and the front of the cell was evacuated. The front of the cell was then pressurized with Xe. The back of the cell was pressurized with N_2 providing a constant backpressure so that the hp Xe for the delivery system was at a constant pressure.

The T_1 time in the cell was reported as being 18 minutes; moving the piston showed that this time was independent of the surface-to-volume within the cell. The apparatus was within the stray field of a 2 T magnet. Final polarization was dependent on the number of cryo-accumulations of Xe, however under typical conditions a polarization of 7.5 % was quoted.

Imai *et al.* explored SEOP of ^{129}Xe at low optical pumping pressures [8]. A simple diaphragm pump was used to supply hp gas to the NMR detection region at atmospheric pressure. While investigating batch mode gas production the diaphragm pump was tested to ascertain its effect on the NMR SNR. The decrease in SNR was seen to be as low as 10 % presumably due to depolarization of the gas while in the diaphragm pump.

Hp ^{83}Kr compression has not previously been described in literature.

4.3 Experimental methods and procedures

4.3.1 Optical pumping of ^{83}Kr and ^{129}Xe

4.3.1.1 Polarizers

The low-pressure batch-mode Rb-SEOP method used in these experiments have been described in detail in **Chapter 3** and elsewhere [3], and a similar set-up was used for these experiments.

Two different SEOP polarizers were used. Most of this study was conducted using a system that utilized a line-narrowed (0.25 nm line width) diode array laser system (30 W Comet Module, Spectral Physics, Santa Clara, CA, USA) to generate laser light to 794.7 nm. Light was circularly polarized and had a

power of 25 W once it reached the SEOP cell (Fig. 4.1) for most experiments. The stray field of a 9.4 T superconducting magnet provided the magnetic field required for optical pumping (about ~500 G at the SEOP cell), and was aligned parallel with the laser light (within 0.5°).

A slightly different SEOP apparatus was utilized for the imaging experiments as well as experiments looking at polarization losses in the piston extraction-compression device for ^{129}Xe. In these studies 30 W of circularly polarized laser light reached the front of the SEOP cell, and a field of 70 G generated by a pair of double Helmholtz coils were used to allow for optical pumping as opposed to the stray field described above. These differences did not show a dramatic change in polarization for the ^{83}Kr imaging experiments.

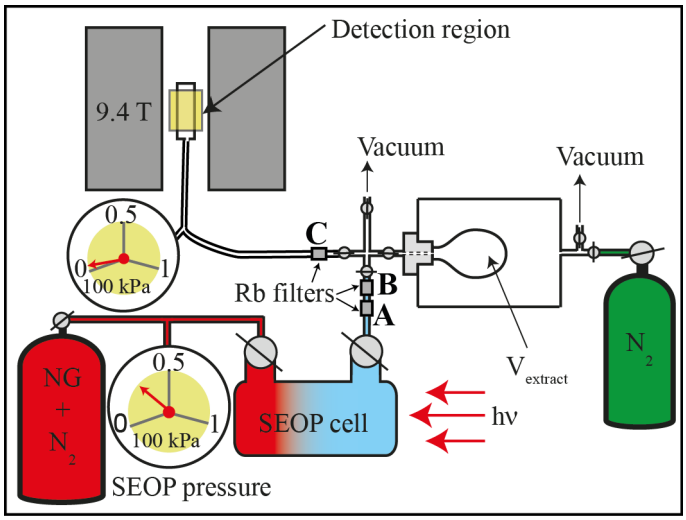

Fig. 4.1 - Apparatus required for the production and delivery of hp noble gas, including the extraction and compression of hp gas. *Noble gas-nitrogen gas mixtures were hyperpolarized in the SEOP cell. For direct polarization measurements the extraction unit was closed to the SEOP cell and hp noble gas was transferred to a glass detection cell via pressure equalization. Optional Rb vapour filters (**A**-**C**) are also shown.*

4.3.1.2 SEOP cell construction and preparation

The bespoke SEOP cells were made from borosilicate glass (typically; length = 120 mm, inner diameter = 28 mm, volume ≈ 65 cm^3) and were fabricated by specialist glass blowers (Michael Olsen or Clive Dixon). A length of borosilicate glass was first cut (~ 120 mm long). Two commercial valves had ground glass connection pieces attached and where added to the top of the tube (Part No. CG-511, Chemglass Life Sciences, Vineland, NJ, USA); one at either end ~ 10 mm from the cut. Optically transparent glass flats were then typically attached to the end of each tube. There were variants on this SEOP cell design; often rounded end pieces were used instead of flats, also some version of the cells had an unused condenser. A typical cell is shown in Fig. 4.2.

Fig 4.2 – Photograph of a typical SEOP cell. *A length of borosilicate glass tube had two commercial glass valves added, and optically transparent windows on either end. Note that in this case rounded windows have been used; also this variant of the SEOP cell has a condenser.*

Before Rb was loaded, cells were baked overnight in a vacuum oven (temperature > 100°C). Cells where then rapidly transferred into the vacuum chamber of an inert (N_2) environment glove box (Labconco, Kansas City, USA). The vacuum chamber was evacuated (16 kPa) and then refilled to roughly an atmosphere of N_2. This process was repeated eight times to ensure that any contaminants (mainly H_2O and O_2) where purged from the chamber and SEOP cells before transferring the SEOP cells into the main glove box. A storage ampoule containing Rb (99.75%; Alfa Aesar, Heysham, UK) was heated using a hot air blower (Tesco PLC, Cheshunt, UK) until the Rb liquefied. A glass pipette was then heated and used to carefully transfer a small amount of Rb (~ 1 g) into the SEOP cell. The correct amount of Rb to transfer was calibrated by filling a pipette with a 1 g ampoule. The height that the Rb reached on the pipette was measured (83 mm from the base) and this was the target height for all subsequent fillings. While not a wholly accurate method large variations in achievable polarization were not seen with cells with quite different quantities of Rb (± 20 %). Once filled the glove box was pressurized above one atmosphere and the SEOP cell/cells were capped off.

In the next stage in the preparation process the SEOP cell was transferred out of the glove box and evacuated. The cell was then 'primed' by heating it using a hot air gun (Steinel, Herzebrock-Clarholz, Germany) to 523 K until a thin layer of Rb had coated the outer walls of the cell. This typically took 15 minutes. It should be noted that care was taken to avoid Rb coating on either window of the SEOP cell. When this occurred the window in question would be heated to 603 K briefly until the Rb layer dissipated. Once the cell had cooled it would be re-filled with N_2 before being transferred to the polarizer.

4.3.1.3 Polarizer operation

SEOP cells were housed in an aluminium oven, with quartz windows, and a single hot-air inlet. Air temperature was regulated by a temperature controller, which was attached to two IR-shielded thermocouples on the surface of the SEOP cell. The internal SEOP cell temperature is unknown. The operating temperature was set on the temperature controller to 433 K for ^{83}Kr and 373 K for ^{129}Xe, with this value varying by ± 10 K over the course of most experiments.

A pressure transducer was used to monitor SEOP cell pressure. Pressure was regulated by throttling the valve between the gas mixture regulator and the SEOP cell inlet, until the desired pressure is reached.

A near-steady-state polarization was achieved for ^{83}Kr after 8 minutes (approximately 80% of the full build value) and a steady-state polarization for ^{129}Xe after 6 minutes for spectroscopy experiments. A build time of 12 minutes was used for Kr imaging experiments (approximately 90% of the full build value).

4.3.2 Gas mixtures

In addition to the gases listed in **Chapter 3** two isotopically enriched gases were utilized in this study; isotopically enriched Kr (enriched to 99.925 % ^{83}Kr; Chemgas, Boulogne, France), and isotopically enriched Xe (99.995 % pure; enriched to 83 % ^{129}Xe; Nova Gas Technologies, Charleston, SC, USA.

4.3.3 Determining polarization accuracy and values

Polarizations for natural abundance gas mixtures were determined by comparing the hp signal to the signal from a sealed thermal sample and described in **Section 3.2.5** in the previous chapter.

Polarizations for enriched gas images take the polarization values measured for non-enriched noble gas mixtures of the same type at the relevant pressure. Therefore no enriched thermal sample was used in these experiments. For ^{83}Kr the longer build (of 12 minutes) and higher laser power (30 W at the SEOP cell) are not accounted for when polarization values are quoted. Therefore it is likely that the actual polarizations are slightly higher than those quoted.

A standard mixture (5 % Xe, 95 % N_2) was used before the start of Xe experiments to ensure that the SEOP cell was producing adequate polarization. For Kr the polarization was checked for the one mixture used (24.8 % Kr, 75.2 % N_2). Polarization for an SEOP cell was checked with these mixtures at 230 ± 20 kPa. If a polarization of less than 40 % was observed for Xe or 3.5 % for Kr then the cell would be replaced.

Multiple SEOP cells were used in these experiments over a number of days. This introduced a source of error as different SEOP cells (while otherwise almost identical) produced different polarizations depending on thermocouple placement, rubidium distribution, or rubidium contamination (such as from CO_2, H_2O, or O_2). To negate this effect as much as possible, Xe polarization values were scaled depending on the polarization value of the standard mixture at the start of experiments. The highest standard mixture polarization was acquired before the collection of the 25.0 % Xe 75.0 % N_2 curves; therefore these polarization values have not been scaled. Kr polarization values were not scaled as only one mixture was used for the recompression experiments.

With the polarizations scaled (up to a factor of 1.2) the greatest remaining source of error in the polarization values were due to changes in the SEOP cell over the course of experiments. It is believed that these fluctuations are caused by external contaminants (such as CO_2 or O_2) leaking into the SEOP cell, changes in distribution of Rb, and minor changes in the cell temperature.

To try and prevent these polarization fluctuations from affecting the observed relationship, polarization values at significant SEOP cell pressure were taken at least four times. An average of these values are presented along with a standard deviation. On one occasion this was not possible for Kr as the SEOP cell became notably contaminated before a full set of repeats could be taken. The error given in the Kr measurements at 50 kPa are taken from a repeat experiment not presented in this work.

Error values quoted for points not repeated four times take the standard deviation from its relevant curve, scaled according to the polarization value.

4.3.3.1 Processing of piston extraction-compression polarization losses values for ^{129}Xe

The different polarizer apparatus utilized when looking at losses in polarization for ^{129}Xe using the piston extraction-compression method made reaching the exact SEOP cell pressure for repeat experiments difficult. As a consequence there are differences in the SEOP cell pressures for the direct polarization and extraction-compression polarization measurements (± 1 kPa) once the pressure was below 50 kPa. In this regime a change in pressure like this causes noticeable differences in polarization. To better determine the losses observed the direct polarization values below 50 kPa are fit to a polynomial (n = 3) and this is used to find a good estimate of what the direct polarization values would have been at the pressures where extraction-compression polarization values were found. These values were then used to calculate polarization survival.

4.3.4 The extraction-compression units

The extraction-compression units were unique to these experiments. The first unit, or the balloon extraction-compression unit (Fig. 4.3), had two main parts: The gas extraction volume ($V_{extract}$), and the chamber around it. The volume

($V_{extract}$) was made from a simple latex balloon and as such was a highly elastic, gas tight polymer bag (Cofalu Kim'Play, La Brède, France). The body of the chamber was built from an acrylic tube (length: 200 mm, inner diameter: 100 mm) with a single acrylic screw cap connecting the balloon to the body of the chamber (vacuum tested to 0.1 kPa, pressure tested to 300 kPa); the caps internal volume has been minimized to reduce loss of gas. When screwed into the body of the chamber it created a gas-tight seal between the cap and the surrounding chamber allowing for either vacuum to be pulled or gas to be pushed into the chamber to either expand or contract the gas extraction volume ($V_{extract}$).

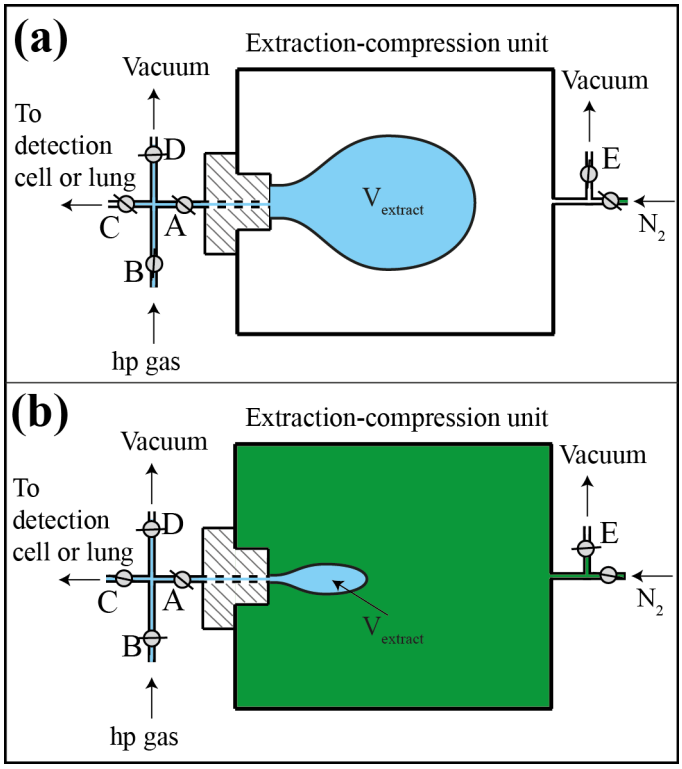

Fig. 4.3 – Balloon extraction-compression unit. ***(a)*** *For extraction-compression experiments the volume $V_{extract}$ and the volume of the surrounding chamber were evacuated by opening the two vacuum values (valves **D** and **E**). Once both volumes were evacuated to a pressure of 1-2 mBar in $V_{extract}$, vacuum valve **D** was closed. With the valve to the detection cell or lung (valve **C**) closed $V_{extract}$ was opened to the SEOP cell. $V_{extract}$ was an elasticized volume and the pressure differential between $V_{extract}$ and its surrounding chamber, as well as $V_{extract}$ and the SEOP cell results in a transfer of gas from the SEOP cell and $V_{extract}$. $V_{extract}$ expanded during this process.* ***(b)*** *Valve **B** to the SEOP cell and vacuum valve **E** was closed. The N_2 valve was opened filling the surrounding chamber of the extraction unit with 3 bar of N_2. This collapsed $V_{extract}$ and compressed the hp gas. Valve **C** was opened and the hp gas was transferred to either a lung or the detection cell. Sealing valve **A** allowed the extraction unit to be moved while filled with hp gas. This was useful if the polarizer and imaging system were a significant distance apart.*

NMR spectroscopy experiments used to determine the losses in polarization experienced by hp gas after an extraction-compression cycle required two

parts. Direct polarization measurements (P_{direct}) were taken where hp gas was transferred to a pre-evacuated detection cell by opening it to the SEOP cell.

The pressure differential would result in a gas transfer. Under these circumstances the extraction-compression unit was closed to the system (valve **A** closed).

Polarization values after an extraction-compression cycle ($P_{ex\text{-}com}$) were also required. Here, $V_{extract}$ was opened to vacuum (valve **D**) until only about 1-2 mBar of gas remained, valve **E** was then be opened exposing the surrounding chamber to vacuum. It was important to evacuate both volumes for 60 seconds prior to experiments so that the volume $V_{extract}$ would fully collapse prior to an hp gas delivery.

Valves **C** + **D** were closed prior to hp gas delivery. Valve **B** was opened, creating a clear path between the SEOP cell and the volume $V_{extract}$. Due to the pressure differential hp gas transferred to $V_{extract}$, which physically expanded. Depending on the SEOP cell pressure, $V_{extract}$ would not always reach its maximum size. The gas transfer would slow down as the pressure differential between $V_{extract}$ and the SEOP cell grew smaller. Long residence times in $V_{extract}$ as well as the lines between the SEOP cell and the extraction-compression unit resulted in hp gas relaxation, and therefore it was desirable to minimize these times. Ultimately it was decided that gas transfer times should be limited to 5 seconds to keep such losses to a minimum.

After gas extraction valve **B** to the SEOP cell was closed, followed by the vacuum valve **E** and the surrounding chamber was pressurized with ~300 kPa of N_2, collapsing $V_{extract}$ and compressing the hp gas. Once compressed valve **C** to the pre-evacuated detection cell was opened, transferring the hp gas to the cell. Extraction-compression was conducted in the same fashion for lung imaging experiments; hp gas delivery to the lungs will be discussed in greater detail later (**Section 4.3.8**).

In a typical experiment the extraction-compression unit was positioned such that the field strength over the unit was close to 50 G. Crude experiments were run to roughly test the stray fields effect on polarization retention. Gas was delivered to the chamber (in these cases the piston extraction-compression device) and the chamber was moved outside of the stray field for a time (5 minutes for ^{129}Xe and 30 seconds for ^{83}Kr). The chamber was then returned and a polarization measurement was taken. These polarization values where compared to when the chamber was not move, but gas was left in the chamber for the same amount of time.

This showed that the presence of an external field appeared to have little effect on ^{129}Xe polarization (polarization change was within the polarization fluctuation), and a minor effect on ^{83}Kr polarization (~1/5 loss) although the severity of the effect was inconclusive. Additional repeats would be needed to fully characterize this behaviour.

The piston extraction-compression unit was constructed from an acrylic tube (length: 450 mm, inner diameter: 58 mm, outer diameter: 70 mm) with acrylic screw caps attached to the tubing and fitted with an O-ring that seals the device (vacuum tested to 0.1 kPa, pressure tested to 300 kPa). The extraction volume ($V_{extract}$) of the unit was 790 cm^3 (Fig. 4.4a).

The extraction unit in this work only needed to attain vacuum condition of less than 0.2 kPa prior to hp gas extraction from the SEOP cell and then compress the extracted hp gas to ambient pressure. Therefore, the unit operated at a high-pressure differential and an O-ring seal equipped acrylic piston (length: 150 mm) provided gas tight isolation of the two compartments of the extraction unit. The extraction-compression unit was encompassed by a solenoid coil (N = 110 turns, length = 27 cm) driven by 10.16 amperes (Sorensen DLM 60-10, San Diego, CA, USA) creating a static magnetic field of 0.005 T. The magnetic field aimed to reduce the relaxation of the hp ^{83}Kr inside the extraction unit (Fig. 4.4) [27].

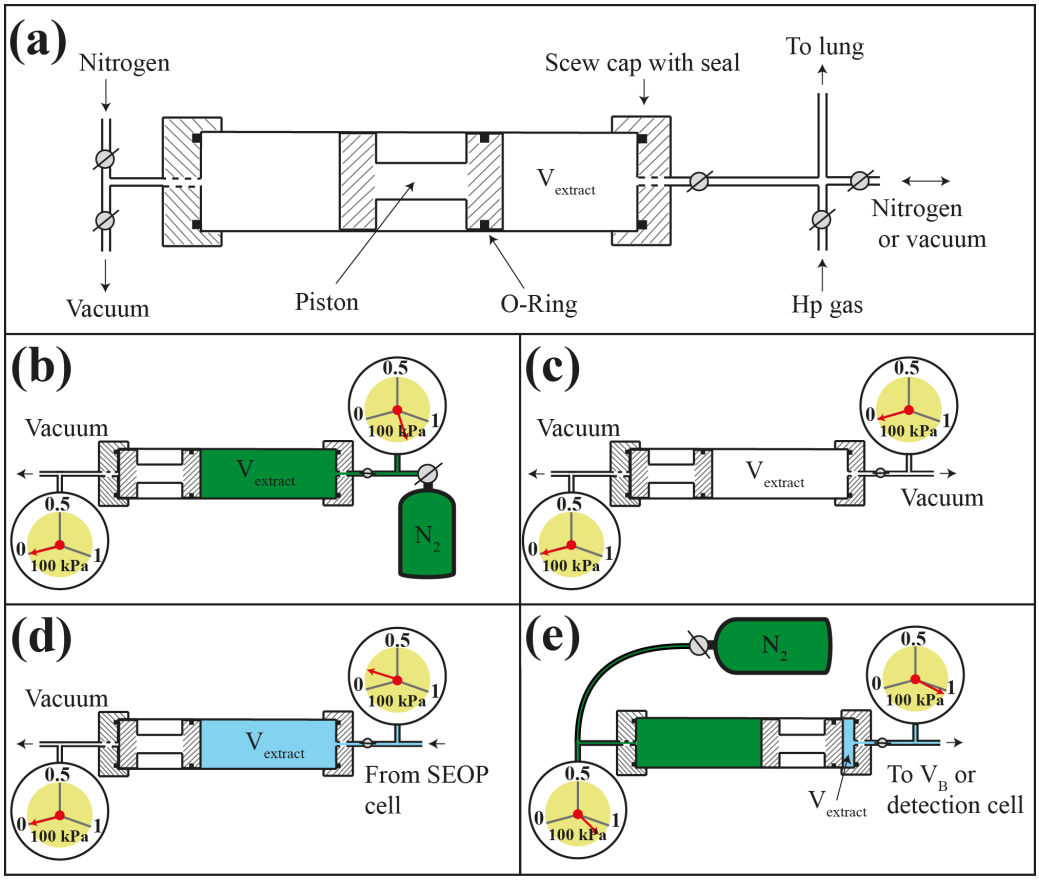

Fig. 4.4 - The piston extraction-compression unit. ***(a)*** *Diagram of the two-chamber extraction-compression unit with the front chamber ($V_{extract}$) to accommodate the hp gas. The back chamber can be either evacuated or pressurized in order to drive the piston. The two chambers were isolated from each other by a single O-ring equipped piston. The stabilizer of the piston was included to keep the piston aligned.* ***(b)*** *The piston was pushed to the back position through the pressurization of $V_{extract}$ with N_2 and evacuation of the back chamber.* ***(c)*** *$V_{extract}$ was evacuated to prepare for hp gas extraction from the SEOP cell.* ***(d)*** *Hp gas extraction from SEOP cell was now complete and $V_{extract}$ was filled with low-pressure hp gas.* ***(e)*** *The volume $V_{extract}$ was sealed by a valve and the back chamber was pressurized with N_2 forcing the piston to move forward thus compressing the hp gas. Once the hp gas in $V_{extract}$ was slightly above ambient pressure, $V_{extract}$ opened to the delivery line and the hp gas was driven into either a glass detection cell or the storage volume (V_B) as detailed in Fig. 4.5.*

Extraction and compression of hp gas using the piston required multiple steps as described in Fig. 4.4b-e. Initially the piston was retracted by pressurizing $V_{extract}$ with 300 kPa N_2 while simultaneously pulling a vacuum on the back of the piston (Fig. 4.4b). Once in this position $V_{extract}$ was evacuated to below 0.2 kPa (Fig. 4.4c). $V_{extract}$ was subsequently opened to the SEOP cell for 5 seconds. This limited pressure equalization to about 80% between $V_{extract}$ and the SEOP cell, however this loss of gas was deemed acceptable to limit relaxation in the chamber and gas lines: Therefore only ¾ of the gas from the SEOP cell are transferred. In a typical imaging experiment this resulted in a pressure of 6 kPa in $V_{extract}$ (Fig. 4.4d). Hp gas was compressed by pushing 300

kPa of N_2 behind the piston, driving it forwards (Fig. 4.4e). The extraction-compression unit was then opened to either a detection cell or the storage volume (V_B) in for lung imaging.

4.3.5 Spectroscopy experiments

NMR spectroscopy utilized bespoke 15 mm saddle probes tuned to 110.5 MHz and 15.4 MHz for ^{129}Xe and ^{83}Kr experiments respectively. Polarization measurement experiments, with the notable exception of the ^{129}Xe piston extraction-compression study, were preformed with a vertical bore (89 mm inner diameter) 9.4 T superconducting magnet (Oxford Instruments) and a Magritek Kea 2 spectrometer (Wellington, New Zealand). All other experiments used the 400 MHz Bruker Avance III microimaging system described in the *Imaging protocol* section.

4.3.6 Imaging protocol

MRI experiments were performed with a vertical wide bore (30 mm with gradients, 89 mm inner diameter) 9.4 T Bruker Ultrashield superconducting magnet and Bruker Avance III microimaging system (Bruker Corporation, Billerica, Massachusetts, USA). A bespoke 25 mm birdcage probe tuned to 110.7 MHz and a Bruker 30 mm double saddle probe tuned to 15.40 MHz were used for ^{129}Xe or ^{83}Kr lung imaging respectively. The 25 mm ^{129}Xe birdcage probe was also used for T_1 experiments in the lung.

Images were acquired by means of a variable flip angle (VFA) FLASH protocol [28]. ^{129}Xe imaging experiments utilized 64 phase encoding gradient increments with T_E = 214.5 ms and T_R = 2.61 ms, this imaging protocol results in a total acquisition time of 13.8 s. The presented coronal images are acquired into 128 × 64 matrices resulting in a field of view (FOV) of 46.9 mm in the longitudinal (frequency encoding) and 30.0 mm in the transverse (phase encoding) directions, respectively. Sinc-shaped soft pulses of 1 ms were utilized for excitation. Fig. 4.9a-d selectively excite a 4 mm central coronal slice of the lung, resulting in a nominal resolution of 0.37 × 0.47 × 4 mm^3.

Two imaging protocols were used for ^{83}Kr imaging; both employed 32 phase encoding gradient increments and are acquired into 64 × 32 matrices. For the images in Fig. 4.10a-b T_E = 17.9 ms and T_R = 4.9 ms, with a total acquisition time = 0.57 s. 0.8 ms Gaussian soft pulses of variable power levels were used for excitation. The resulting FOV was 51.0 mm in the longitudinal and 38.1 mm in the transverse directions. Similarly, the image in Fig. 4.10c used a T_E = 4.2 ms and T_R = 19.2 ms, with a total acquisition time = 0.615 s. 0.2 ms sinc-shaped pulses of variable power levels were used for excitation. The resulting FOV was 50.9 mm in the longitudinal and 40.7 mm in the transverse directions. The slice selective images in Fig. 4.11 also utilized a 2 ms sinc-shaped soft pulses of variable power to selectively excite a 3 mm central coronal slice of the lung.

T_1 weighted images (Fig. 4.11b-d) were attained by placing a time delay before the start of the imaging sequence (t_d). Four different time delays were explored, allowing for the creation of a T_1 map (Fig. 4.11e).

Image processing was conducted using Prospa (v. 3.06, Magritek, Wellington, New Zealand). The T_1 map was constructed by further analyzing the four T_1 weighted images using IGOR Pro (v. 6.01, Wavemetrics, Lake Oswego, OR, USA), where T_1 was calculated for each voxel. Values outside of the actual lung were discarded.

4.3.7 Preparation of excised rat lungs

Male Sprague-Dawley rats (Charles River, Margate, UK) weighing 360 - 450 g were used in this study. These weights of rat were chosen as they roughly corresponded to the maximum lung size that would fit into the ventilation chamber (Fig. 4.5, described later). Larger rats (400 – 450 g) were used in the Kr imaging experiments as a larger RF coil was available, allowing for the use of a large ventilation chamber (outer diameter = 30 mm, inner diameter = 28 mm), compared to the chamber used in Xe experiments (outer diameter = 25 mm, inner diameter = 23 mm).

Rats were humanely euthanized by overdose of pentobarbital (Sigma-Aldrich ltd, Gillingham, UK) in accordance with A(SP)A 1986 (Animals for Scientific Procedures Act 1986). The lungs were inflated with around 3 ml of air and the trachea clamped; then the lungs, heart, and connective tissue were extracted *en bloc*. Additional organs, such as the thymus, were removed, as they were not necessary for this study.

After extraction, the lung's trachea was cannulated and a syringe was used to ventilate the lungs. This was primarily done to ensure that the lungs retained gas and were not damaged during their removal. Lungs found to leak were discarded.

Lungs would be inflated with 3 – 10 ml of air (depending on their size) and then sealed off. Lungs were stored in chilled glucose solution (5 % glucose in water, Baxter Healthcare Ltd, Thetford, UK) until needed.

4.3.8 Ventilation chamber and lung inhalation

Excised rat lungs were inserted into a bespoke, sealable, ventilation chamber (described earlier), which filled the entire coil region. The trachea of the rat lung was cannulated with an adaptor that was attached to the top of the ventilation chamber. The ventilation chamber was filled to about 2/3 of its total volume with a 5% glucose solution (Baxter Healthcare Ltd, Thetford, UK).
Similar to the ventilation chamber used in previous work [29], the chamber had two gas inlets. One connected to the trachea and was where hp gas was inhaled. The second gas inlet was connected to the remaining unfilled portion of the ventilation chamber.

Hp gas was delivered to the storage volume V_B after compression (described the Extraction schemes detailed elsewhere). The hp gas in the volume $V_{extract}$ was driven into the storage volume V_B, displacing the existing gas. The volume was open to ambient, preventing it from exceeding atmospheric pressure. When suction was applied through the inhalation syringe pressure equalization forced the lungs to expand (Fig. 4.5b). This acted in a similar fashion to the thoracic diaphragm, as the expansion of the lungs caused it to inhale gas from the volume V_B. The volume pulled did not directly correlate to the inhalation volume of the lung. Calibration experiments have shown that an inhalation of 10 ml used for Kr imaging experiments correlated with an uptake of 8 ml of gas to the lungs. An inhalation of 5 ml used in the Xe experiments roughly corresponded to the lung up-taking 3 ml of gas (described in Fig. 4.5).

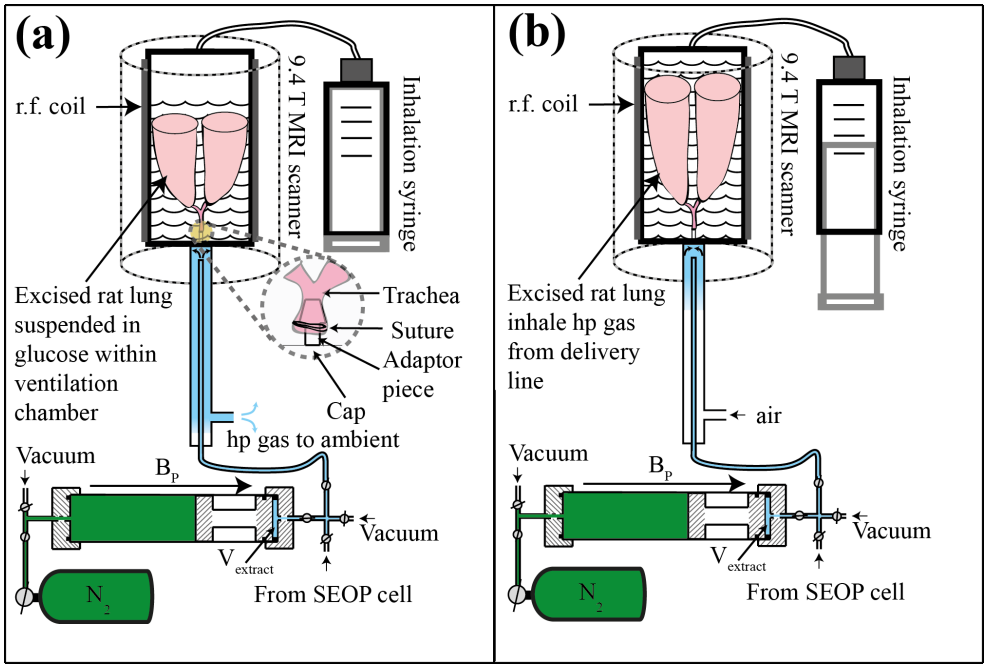

Fig. 4.5 - Experimental setup of the piston extraction-compression unit, ambient pressure storage volume (V_B) and lung ventilation chamber. *This figure displays the piston extraction-compression unit. Not depicted here, the balloon extraction-compression unit was attached to the delivery line in the same way.* ***(a)*** *Hp gas was extracted form the SEOP cell, compressed to ambient pressure, and delivered into the storage volume V_B as described in Fig. 4.4. The hp gas displaced the existing gas in V_B that exhausted through a vent port from the storage volume to ambient. The trachea of the excised lung was sutured to an adaptor inside the ventilation chamber and suspended in glucose solution. The ventilation chamber connected to the ambient pressure storage volume for hp gas delivery to the lungs.* ***(b)*** *The inhalation syringe was pulled to a given volume. This pulled a slight vacuum on the glucose suspending the lung, forcing the lung to expand. This resulted in the lung up-taking hp gas from the delivery line.*

For hp ^{83}Kr lung imaging, the gas delivery line and recompression chamber were connected by a series of untreated glass pieces to ensure that the hp ^{83}Kr gas would relax less quickly during gas transfer [30]. It was also observed that

the stray field gradient had an adverse effect on ^{83}Kr polarization depending on the positioning of the lines within said gradient. This was a particular issue when the experiments were near an actively shielded magnet. To avoid the effect of the gradients, the lines were carefully positioned and fixed in place; the valve assembly for the delivery of hp gas was surrounded by a Helmholtz pair generating a weak magnetic field (less than 5 G).

Relaxation within the piston extraction-compression unit (Fig. 4.4a, $V_{extract}$) was also believed to be longer in the presence of a magnetic field, evidenced by the crude experiment described earlier where the chamber was removed from the 50 G stray field. Work from the literature has shown that ^{83}Kr T_1 has a dependence on the magnetic field [27], however this work suggests that the T_1 dependence on the magnetic field would break down at the low magnetic field strengths used in this experiment. The reason for this observed dependence will be discussed further in the results section. Therefore a solenoid coil was used to surround the chamber, providing a magnetic field of 50 G. This apparatus is shown in Fig. 4.6.

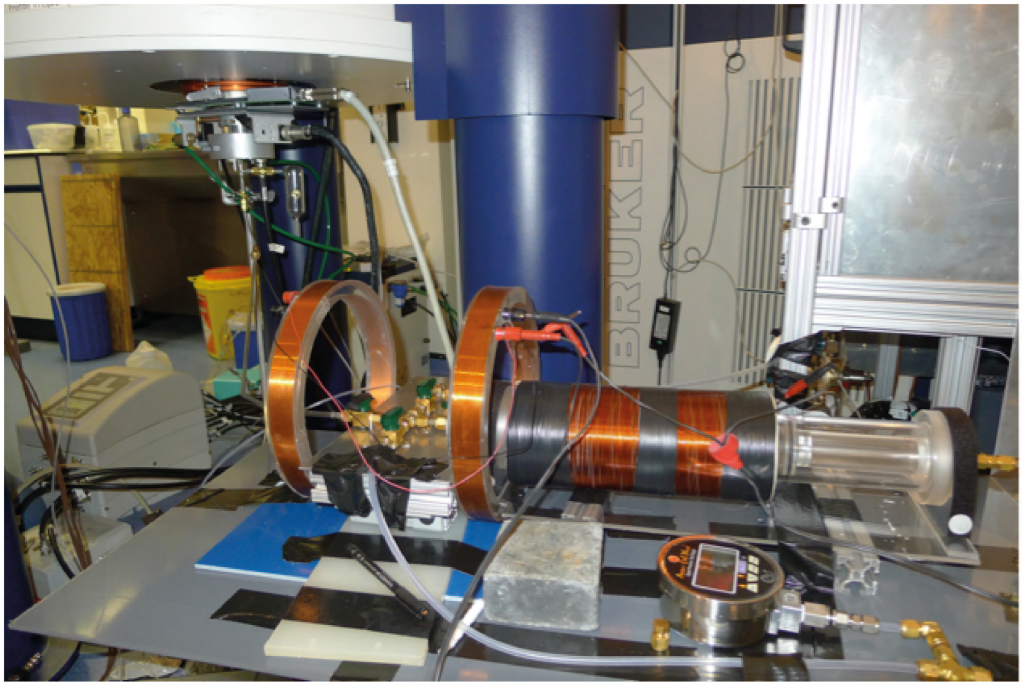

Fig 4.6 – Photograph of the extraction-compression chamber and delivery system (prototype). *The extraction volume, $V_{extract}$, is surrounded by a solenoid coil. The valve assembly and glass connecting pieces are enclosed by a Helmholtz pair.*

Prior to the start of an experiment a 50 ml syringe of air was ventilated through the lung. This was done to feed the lung O_2 with the aim of keeping the tissue alive for the duration of the experiment.

For ^{83}Kr imaging experiments a typical SEOP cell pressure of 90 – 100 kPa was used. Experimenting with different SEOP cell pressures showed that this provided more than an adequate amount of gas to fill the delivery system and the lungs. The minimum SEOP cell pressure required using this apparatus was 80 kPa.

The forward volume of the piston chamber ($V_{extract}$) was pre-evacuated. Hp gas was then delivered into the volume $V_{extract}$ as described in **Section 4.3.4**. Closing its valve isolated $V_{extract}$ and the valve assembly in front of the recompression chamber was evacuated of gas. The back of the extraction-compression unit was opened to a high pressure (~3 Bar to ensure fast compression) N_2 supply, driving the piston and reducing the size of the volume ($V_{extract}$). The volume $V_{extract}$ was opened to the delivery line, filling the storage volume (V_B) with hp gas.

10 ml was pulled on the inhalation syringe causing the hp gas to be transferred from the gas delivery line to the lung. Residence times of Kr in the delivery line were minimized to reduce potential relaxation.

The magnet was equipped with water-cooled gradient coils keeping the bore at a temperature of 12 °C throughout the experiments.

For hp ^{129}Xe lung imaging experiments the balloon extraction-compression unit was used. The reasoning for this will be discussed in greater depth in the results section.

The ventilation chamber was connected to an acrylic and perfluoroalkoxy (PFA) gas delivery line. The delivery line was of a similar design to the glass one used for Kr. Glass was not used for Xe experiments as surface induced relaxation was less of a concern and the glass lines were fragile and difficult to repair. The recompression chamber was attached to the gas delivery line with thin PFA tubing (i.d. = 1.5 mm). This required significantly less gas to fill than the complex glass system used for ^{83}Kr. Subsequently less hp gas was required, allowing for optical pumping to be conducted at a lower pressure.

As with the Kr experiments lungs were ventilated with 50 ml of air to help keep the tissue alive. In addition, just prior to the start of an experiment (about a minute in advance) the lung would also be ventilated with a 50 ml syringe of research grade N_2 to remove excess O_2, as the highly paramagnetic O_2 severely reduces ^{129}Xe T_1 times [31].

SEOP experiments were conducted at about 50 kPa for Xe. After the extraction-compression cycle described in **Section 4.3.4** this gave approximately 18 ml of recompressed hp gas (at a 50 kPa SEOP cell pressure), delivered into the storage volume V_B. Through iterations it was found that this was approximately the minimum amount of gas required to adequately displace existing gas in the delivery line and to fill the lung.

Once the hp gas was transferred to the storage volume, 5 ml was pulled on the inhalation syringe (inhaling about 4 ml of gas into the lung). Relaxation in the gas delivery line was believed to be minimal for the residence times of the noble gas in the line.

4.3.9 Rubidium filters

Rubidium in the vapour phase occurs when the Rb in the SEOP cell is heated to allow for SEOP. This is typically removed from hp Xe during the cryogenic separation of the Xe and other gas mixtures [4, 5]. As this methodology omits such a step it is important to determine the quantity of Rb, if any, that travels with the hp gas during extraction from the SEOP cell and in the final gas inhaled by the rat tissue after compression.

To investigate whether significant rubidium was present in the hp gas filters were inserted into the system (identified in Fig. 4.1, and corresponding to Table 4.4). Rubidium filters were made from 60 mm of Teflon tubing (outer-diameter = 9.4 mm, inner-diameter = 6.4 mm; Swagelok, Warrington, UK) with 100 g of glass wool (Corning glass wool, Corning, NY, USA) loosely packed inside. After a number of extraction-compression events the glass wool was extracted and placed in a small glass vial. 1 ml was introduced and the pH of this water was taken using chemical indicator paper (Whatman plc, Maidstone, UK).

For this part of the study, ^{83}Kr SEOP conditions where used, as a greater quantity of Rb was in the vapour phase due to the associated higher optimal SEOP temperatures for ^{83}Kr (in this case 170 ± 10 K).

4.4 Results

4.4.1 Low-pressure extraction-compression curves for ^{83}Kr

Fig. 4.7 shows near steady-state (i.e. after 8 minutes) apparent polarization (apparent polarization after 8 minutes, ~80 % of full steady state polarization build) as a function of SEOP cell pressure for a Kr-N_2 gas mixture, with a corresponding curve showing the polarization values at various SEOP cell pressures after the gas has been extracted and compressed. Apparent polarization has been discussed in detail in **Chapter 3**, and is given by Eq. 3.3. Two extraction-compression modalities have been shown in Fig. 4.7; with the piston extraction-compression unit and with the balloon extraction-compression unit.

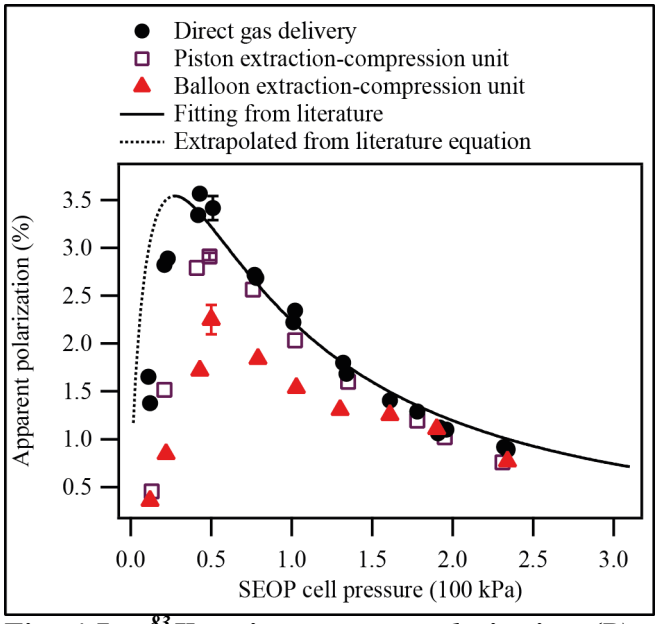

Fig. 4.7 – ^{83}Kr spin apparent polarization (P) as a function of SEOP cell pressure and corresponding extraction-compression polarization values for two recompression modalities. *^{83}Kr apparent spin polarization as a function of total gas pressure in the SEOP cell for a 24.8 % Kr, 75.2 % N_2 gas mixture with corresponding values (see legend) for both extraction-compression modalities. The piston extraction-compression method clearly shows less polarization losses. Maximum apparent polarization and maximum apparent polarization after extraction-compression ($P_{ex\text{-}com}$) values are stated in Table 4.1 for both modalities. Data analysis will be discussed in* ***Section 4.4.6*** *but is not presented on the figure. Instead an appropriately scaled fitting from literature [32] with a scaled fitting extrapolated from Eq. 4.1 (discussed later) are presented. This shows that the data presented is in good agreement with the literature over the pressure range that the fitting was conducted.*

Greater losses in polarization occur when the balloon extraction-compression unit is used. This is likely due to the surface-dominated nature of ^{83}Kr T_1 relaxation [33-35] and will be discussed further later. Important polarization values for Kr containing mixtures have been displayed in Table 4.1.

Table 4.1 *– Maximum Kr apparent polarization (P*) along with its corresponding polarization. Maximum Kr apparent maximum polarization after extraction-compression $P^*_{ex\text{-}com}$ as well as polarization after extraction-compression are also given. Gas pressures are extracted from Fig. 4.7. Values are given for the two extraction-compression modalities used.*

Mixture composition	***Apparent maximum polarization*** P^* **(%)**	Maximum apparent polarization after an extraction-compression $P^*_{ex\text{-}com}$ (%)	SEOP cell pressure at maximum final apparent polarization $p^*_{ex\text{-}com}$ (100 kPa)	**Maximum polarization (%)**	Maximum polarization after an extraction-compression (%)
24.8 % Kr; 75.2 % N_2 **Balloon extraction-compression unit**	*3.4 ± 0.1*	2.2 ± 0.2	0.50	**13.8 ± 0.5**	9.1 ± 0.6
24.8 % Kr; 75.2 % N_2 **Piston extraction-compression unit**	As above	2.9 ± 0.0	0.49	As above	11.7 ± 0.2

Apparent polarization values are not in complete agreement with values previously reported (**Chapter 3**) due to minor differences in the SEOP set-up. Fitting the data to Eq. 4.1 shows that the relationship is in agreement with previous work [32]. This is discussed further in Section 4.4.6.

Both extraction-compression modalities induce losses in polarization. Potential reasons for polarization loss in both extraction-compression units (due to T_1 relaxation) will be discussed below.

Above 150 kPa polarization losses due to the extraction-compression process appear to be negligible for both systems, with loses only occurring with the piston extraction-compression unit at pressures below 75 kPa. This is possibly because not all of the gas is expelled from the extraction-compression unit. Gas relaxing on the surface of the volume may not mix correctly with the hp gas at the centre of the reservoir in this pressure regime. Therefore gas that has relaxed due to the surface may not be contained in, or only make up a small fraction, of the gas expelled into the detection cell. Therefore losses due to relaxation may not be observed. Alternatively it could purely be due to pressure dependant T_1 relaxation. The pressures in the two units are different at the same SEOP cell pressures, due in part to the maximum volume of gas that can be extracted from the SEOP cell. The pressures in the piston extraction-compression unit will typically be less, leading to longer pressure dependant T_1 times.

Intrinsic gas phase relaxation for ^{83}Kr is known to be linearly dependant on the krypton density [*Kr*] [36, 37]. This is primarily due to the linearity of the dependence between pressure and the frequency of binary collisions. The

relaxation rate has also been shown to have a dependence on the composition of the gas mixture used [36]. While there will be a contribution to relaxation from the formation of Kr-Kr van der Waals molecules, this has previously been observed experimentally to be density independent [38].

Due to its low gyromagnetic ratio ^{83}Kr is largely insensitive to the presence of paramagnetic O_2 [29] (discussed in **Chapter 5**). Thorough evacuation of the system prior to use should remove O_2 adequately to not have to consider paramagnetic T_1 relaxation for this system.

Relaxation due to free diffusion within the field gradient may prove to be significant for ^{83}Kr containing mixtures due to its high diffusivity at low pressures. At the lowest pressures experienced in the balloon it is plausible that the effect of magnetic field gradients on Kr relaxation is comparable to the effects experienced by He at atmospheric pressure in the same gradient. However the fairly uniform solenoid coil used around the piston recompression chamber in imaging studies should remove most of this effect (Hussey et al. [15] mounted their chamber in a Helmholtz pair to minimize this relaxation). Experimentally it was seen that the presence of a field had a small effect on the recoverable polarization after the extraction-compression process. The presence of a ~7.5 mT magnetic field increased the efficiency of polarization recovery by ~20 %; although further work would to needed to fully characterize this effect. This suggests that free diffusion within the field gradient does contribute T_1 relaxation, and therefore to polarization loss.

Previous work has characterized a relationship between the surface component of the T_1 relaxation as a function of surface-to-volume ratio within packed glass bead samples. As expected a greater surface-to-volume ratio led to increased T_1 relaxation [33]. This relationship was not linear as expected, and in this system would be further complicated by the complex dependency between the surface area and volume on the pressure of the gas delivered.

T_1 relaxation due to nuclear electric quadrupolar interactions during brief surface absorptions are often the dominant form of relaxation for quadrupolar nuclei, such as ^{83}Kr. This appears to be the case for the systems described in these experiments.

Polarization losses are significantly greater for the balloon extraction-compression unit. This led to the creation of the piston extraction-compression unit, as it seemed likely that polarization losses were primarily due to ^{83}Kr surface relaxation as the balloon at its smallest volume still had a significant surface area. In the piston design surface area was minimised at all stages of compression. It is also possible that the material of the balloon relaxed the ^{83}Kr to a greater extent than the acrylic of the piston. This cannot be determined without a study into how ^{83}Kr relaxes on these surfaces.

When the optimal SEOP cell pressure was used (0.5 kPa), the T_1 in the piston recompression chamber was found to be 38 seconds.

4.4.2 Low-pressure extraction-compression curves for ^{129}Xe

Fig. 4.8 shows steady-state apparent polarization as a function of SEOP pressure for two Xe-N_2 optical pumping mixtures. A third mixture was examined but has not been shown here for the sake of clarity. Complimenting this are the same curves displaying SEOP as a function of pressure of gas that has undergone an extraction-compression cycle.

Fig. 4.8b shows the polarization value after an extraction-compression cycle ($P_{ex\text{-}com}$) divided by the non-recompressed polarization value (P**)** for the three Xe gas mixtures as a function of pressure; losses relating to the piston extraction-compression device for a 25 % Xe mixture is also presented. The data show that polarization survival is independent of [*NG*].

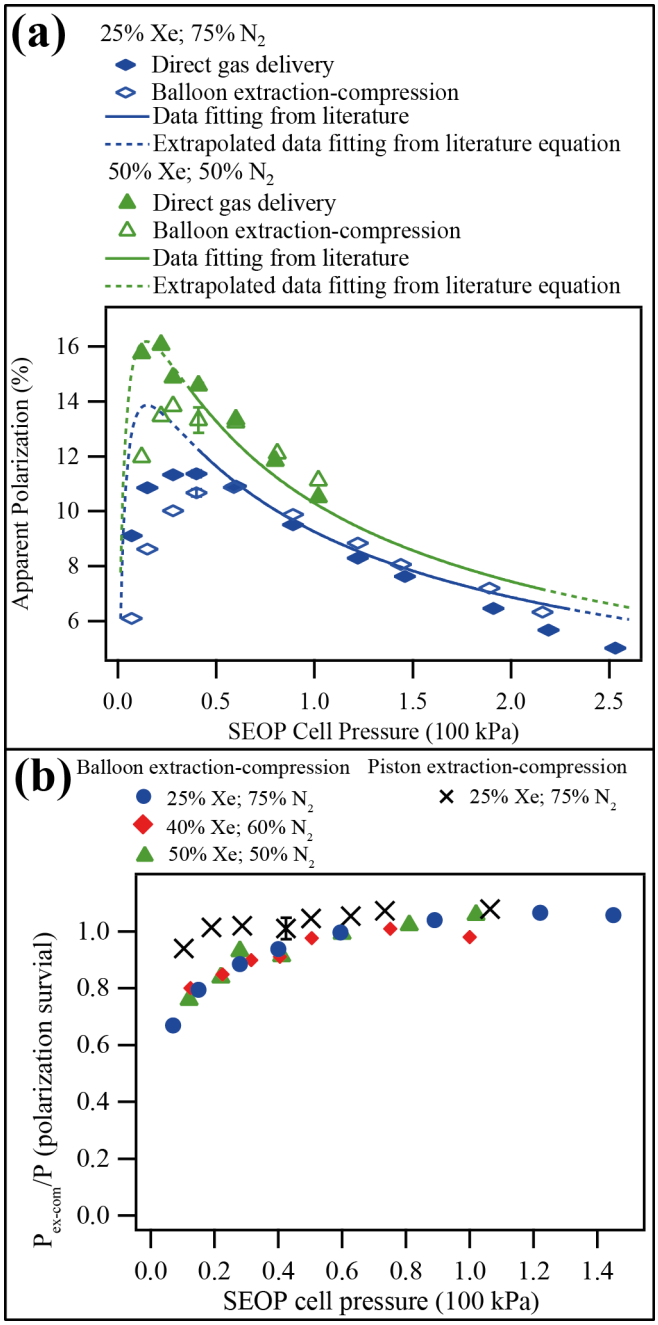

Fig. 4.8 - (a) ^{129}Xe apparent spin polarization (P) as a function of SEOP cell pressure and corresponding extraction-compression polarization values. *^{129}Xe apparent spin polarization as a function of the total gas pressure in the SEOP cell for two different Xe containing gas mixtures (see legend; closed icons). Corresponding recompression values are also shown (open icons). Maximum apparent polarization and maximum apparent polarization values after an extraction-compression cycle are given in Table 4.2. As with ^{83}Kr, a scaled fitting from literature [32] and a corresponding scaled fitting extrapolated from Eq. 4.1 (discussed later) are presented. This shows that both data sets presented are in agreement with the literature over the pressure range that the fitting was conducted. [Continued overleaf]*

(b) Fraction of the polarization surviving after an extraction-compression cycle as a function of SEOP cell pressure. *Fraction of ^{129}Xe spin polarization surviving as a function of the total gas pressure ($P_{ex\text{-}com}/P$) in the SEOP cell for three different Xe containing gas mixtures (see legend) and two extraction-compression modalities. The polarization survival ratio is shown to be independent of [Xe]. Less polarization losses are observed with the piston extraction-compression modality.*

The maximum achievable apparent polarization (P^*) along with its corresponding polarization, as well as the maximum apparent polarization after recompression ($P^*_{ex\text{-}com}$) with the SEOP cell pressure where this occurs ($p^*_{ex\text{-}com}$) and the related polarization, are taken from Fig. 5.8a and are displayed in Table 4.2. Note that P^* and $P^*_{ex\text{-}com}$ may not occur at the same pressure, as discussed later. Data for a 39.6 % Xe, 60.4 % N_2 gas mixture are also presented.

Table 4.2 *– Maximum ^{129}Xe apparent polarization P* along with its corresponding polarization. Maximum ^{129}Xe apparent polarization after a balloon extraction-compression cycle and corresponding apparent maximum polarization after are also given. With the exception of the 39.6 % Xe, 60.4 % N_2 gas mixture, Gas pressures are extracted from Fig. 4.8a.*

Mixture composition	***Apparent maximum polarization*** P^* **(%)**	Maximum apparent polarization after an extraction-compression $P^*_{ex\text{-}com}$ (%)	SEOP cell pressure at maximum final polarization $p^*_{ex\text{-}com}$ (100 kPa)	**Maximum polarization (%)**	Maximum polarization after an extraction-compression (%)
25.0 % Xe; 75.0 % N_2	*11.4 ± 0.1*	10.9 ± 0.1	0.59	**45.5 ± 0.5**	43.5 ± 0.5
39.6 % Xe; 60.4 % N_2	*14.7 ± 0.2*	14.0 ± 0.2	0.50	**37.1 ± 0.4**	35.4 ± 0.6
50.0 % Xe; 50.0 % N_2	*16.1 ± 0.1*	13.8 ± 0.5	0.28	**32.1 ± 0.2**	27.7 ± 1.0

As previously reported, polarization increases as pressure decreases until a maximum is reached. Although different values were found given differences of the SEOP set-up; the scaled data fitting from literature shows that the relationship is in agreement previous work [32]. Agreement with earlier work is discussed in further detail in Section 4.4.6.

The piston extraction-compression unit experienced almost no losses at SEOP cell pressures exceeding 20 kPa. The balloon extraction-compression unit resulted in minimal losses in the pressure regime where SEOP was conducted for imaging (~ 40 kPa), at lower pressures there was not a sufficient quantity of gas: Therefore both units where suitable for imaging studies. An advantage of the balloon extraction unit was its simplicity and durability. Other compression modalities with mechanical components (discussed in **Section 4.2**) are known to fail after multiple compression events. The piston extraction-compression device would operate for between 500 – 1000 extraction-compression events before the outer chamber required replacement due to fractures along the

surface that impeded the movement of the piston. Fractures where caused by pressure (up to 300 kPa) and the motion of the piston itself. Manufacturing the unique body for the piston extraction-compression unit was both costly (on the order of £150 excluding labour) and time consuming. While failure of the balloon also occurred, typically after 1000 extraction-compression events, failure of the balloon itself that was cheap (less than £1) and easy to replace (taking less than a minute).

As both units were adequate for imaging studies, full characterization was only conducted with the balloon extraction-compression unit.

Above 50 kPa it was seen that the polarizations for recompressed gas mixtures either matched or exceeded the polarizations for directly shuttled gas mixtures for both units. This is possibly because the SEOP cells for these experiments included an (unused) air-cooled condenser at the outlet of the cell. This volume did not contain rubidium and was not irradiated by the laser light. Therefore most of the dark gas, non-hyperpolarized gas, will likely be from near the SEOP cell outlet and any additional gas taken from the SEOP cell is likely to be polarized. The total polarization of the gas detected will be higher when extraction-compression is used at higher pressures.

Due to the distribution of the dark gas within the SEOP cell, better mixing of the gas after leaving the SEOP cell may lead to higher polarization values. Vacuum shuttling does not fully mix the gas leaving the SEOP cell over the distances involved in these experiments: Low pressure storage in $V_{extract}$ for either unit will allow for far better gas mixing.

As a result, despite the highest polarizations being achieved below 50 kPa for the balloon extraction-compression unit, the highest polarization values after an extraction-compression cycle are observed to be at SEOP cell pressures equal to higher or than 50 kPa.

For the balloon extraction-compression unit, polarization losses are incurred when the SEOP cell pressure was below 50 kPa due to extraction-compression of the hp gas. Polarization loss is due to T_1 relaxation occurring within the extraction-compression unit (T_1 relaxation in the detection cell is known to be significantly longer than the times required to apply the RF pulse). Factors that contribute to longitudinal relaxation are intrinsic gas-phase relaxation, relaxation due to paramagnetic molecules (in practice O_2), diffusion through field inhomogeneity, and wall relaxation.

Intrinsic gas-phase relaxation occurs upon the formation of Xe dimers. These are most commonly transient and formed by three body collisions. Persistent dimers also exist, where Xe-Xe van der Waals molecules are formed and relaxation is incurred due to spin-rotation coupling (Van der Waal contribution can likely be negated, as they are very slow). Chann *et al.* [39] show that intrinsic gas-phase relaxation is independent of pressure, but has dependence on [*NG*]. Therefore these components of relaxation can be discounted, as a significant cause of polarization loss during an extraction-compression cycle

for this system as Fig. 4.8b, plotting the polarization survival as a function of pressure for the various mixtures, shows no dependence on [*NG*].

Dipole-dipole interactions between Xe and O_2 are known to cause fast Xe T_1 relaxation Xe [31] (discussed in **Chapter 5**), however as the parts of the system that come into contact with hp gas are evacuated of O_2 prior introduction of hp gas these contributions can be said to be negligible.

Motion of a spin-active isotope, such as Xe, in the presence of a magnetic-field gradient can induce T_1 relaxation. As the extraction-compression unit was typically used within the fringe field of a superconducting magnet this factor must be considered [40]. As pressure decreases Brownian motion due to free diffusion within the gradient will increase, decreasing the relaxation time (T_1) at lower pressures [41]. Experimental work using ^{3}He at ~101 kPa by Zheng *et al.* [42] has shown that motion within a magnetic-field gradient can cause significant relaxation in ^{3}He, but highlight that these problems will be significantly less for ^{129}Xe, mainly due to its significantly smaller free diffusion coefficient (Xe-Xe free diffusion coefficient taken from work by Mair *et al.* [43]). The free diffusion coefficient will change depending on gas mixture and therefore, if magnetic-field gradient induced T_1 relaxation is significant; the relaxation observed will be [*NG*] dependant. Fig. 4.8b shows that survival of polarization is not effected by [*NG*], so relaxation has no dependence on the gas mixture composition and therefore magnetic-field gradient induced T_1 relaxation is not significant for this system. This is further supported by earlier crude experiments were the chamber was removed from the magnetic field for some time and returned, whereupon no polarization losses were not observed.

The final relaxation consideration, and the likely cause of most of the relaxation, is relaxation due to the surfaces in the extraction-compression units. However, even this contribution to relaxation will be negligible in the piston extraction-compression unit over the range of pressures explored (as shown in Fig 4.8b).

Considering the balloon extraction-compression unit, assuming that the quantity of Xe gas dissolved in the balloon is minimal when compared to the gas phase Xe, a model proposed by Jacobs *et al.* [44] can be used; where the T_1 relaxation due to the surface is a function of the surface-to-volume ratio. This was a model adopted by Möller *et al.* [45] in their detailed paper characterizing T_1 relaxation for ^{129}Xe in a deflating polymer bag. Unlike this work their polymer bag was not elasticized and only pressures near 1.2 kPa were explored. The study by Möller *et al.* showed that surface relaxation increased linearly with volume and that the relaxation rate ($1/T_1$) increased linearly with the surface-to-volume ratio. It was also established that under their experimental conditions, surface relaxation was the dominating form of relaxation.

For this system surface area and volume are both dependent on the pressure of the gas delivered, as the balloon is stretchable both surface and volume are dependant on the SEOP cell pressure. Elastic resistance in the balloon ensures

that the surface area and volume do not increase at the same rate. At very low pressures the gas pressure is not sufficient to cause the balloon to stretch. From this point the surface area is no longer dependant on pressure (this occurs when the SEOP cell pressure is roughly 0.3 kPa). Similarly the balloon has a maximum size where the surface area will no longer increase. This maximum size is imposed by the size of the extraction-compression unit and not the size of the balloon, which has a greater maximum volume than the extraction-compression unit.

Fig. 4.8b shows that the recoverable polarization, which is directly related to the T_1 relaxation, decreases with SEOP cell pressure. The exact relationship is difficult to characterize for the balloon extraction-compression unit. Given existing literature however it seems likely that surface relaxation is the dominant form of relaxation; the non-linear relationship being due to the complex nature of the surface area and volume pressure dependence.

Future devices based on the balloon extraction-compression devices can avoid this issue by increasing the size of the SEOP cells used, thus increasing the available gas volume at lower SEOP cell pressures. Potentially improvements could also be made to the piston extraction-compression unit by constructing the chamber from a material that is less of a relaxant to Xe such as coated glass [30].

Compression did not always bring the gas in the delivery region up to 100 kPa with either unit, however this was a limitation imposed by the volume of the detection region of this apparatus. In principle up scaling the SEOP cell volume would not incur any additional polarization losses.

4.4.3 *Ex vivo* ^{129}Xe lung imaging

Fig. 4.9 shows eight coronal VFA FLASH images (x, *z*) with a 46.9 x 30.0 mm^2 FOV using a 128 x 64 matrix, 64 gradient increments. Anatomical features can be observed in all images with varying clarity. The alveolar region is visible and major airways (the bronchi) can be distinguished. Fig. 4.9a-d show images with a 4 mm slice. Fig. 4.9e-h display non-slice selective images. Figs. 4.9a+d used research grade ^{129}Xe (26.4 % ^{129}Xe); images are taken with a signle scan. This provided the poorest quality images; background noise is clearly visible. As expected averaging over four scans (Figs. 4.9b+f) resulted in an improved image quality. Theory suggests that this should improve signal-to-noise by a factor of two. Figs. 4.9c,d,g,f use isotopically enriched Xe (83 % ^{129}Xe) which should improve signal-to-noise by a factor of 3.1 over Figs. 4.9a+e. Figs. 4.8c+g used the balloon extraction-compression unit, whereas Figs. 4.9d+h used the piston extraction compression unit. There is little noticeable difference between the images showing that the balloon extraction-compression unit is adequate for ^{129}Xe imaging experiments. Figs. 4.9c,d,g,h produce images with the highest signal-to-noise, as expected.

Imaging with a single scan has few benefits in the *ex vivo* model as lungs remain viable for many hours and the inhalation can be easily controlled. Not

having to average multiple scans does have advantages exist if this method were to be applied to an *in vivo* system. Primarily this method is faster, with a bolus of hp gas being available every 6 minutes. Single scans also negate artefacts from pulsatile flow, cardiac, and respiratory motion apparent in an *in vivo* systems which are sometimes present when images have been averaged. While not employed, this method allows for the production of enough gas for multiple inhalations (at the expense of some polarization) in a single 6-minute build. By taking more scans and averaging them, this potentially allows for further improvements in the image resolution for a 6-minutes experiment.

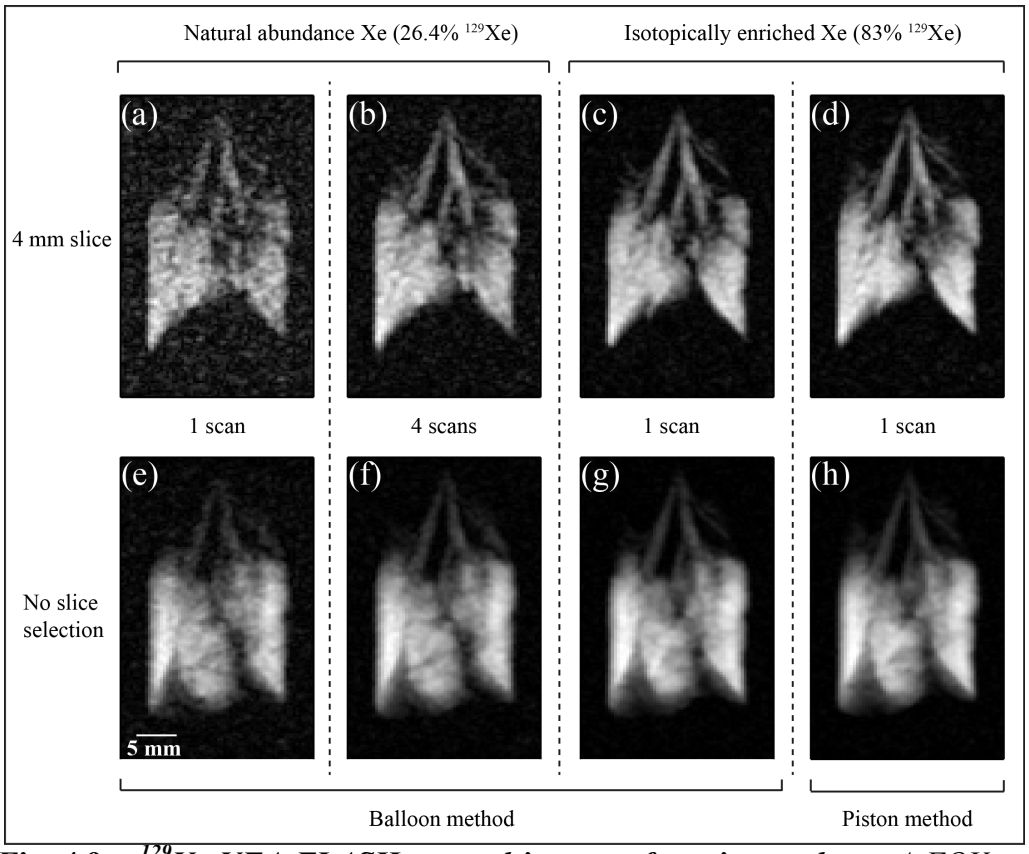

Fig. 4.9 – *^{129}Xe VFA FLASH coronal images of ex vivo rat lung.* *A FOV = 46.9 x 30.0 mm^2 and a 128 x 64 matrix was used. Anatomical structures such as the alveolar region and bronchi can be distinguished on all images. All images except for (d) and (h) used the balloon extraction-compression unit. (a) A single ^{129}Xe rat lung image with a 4 mm central slice. (b) Four images similar to (a) over different inhalation cycles where averaged together to improve the SNR (SNR should improve by a factor of 2). (c) A single ^{129}Xe rat lung image with a 4 mm central slice where isotopically enriched Xe (83% ^{129}Xe) has been used. The use of enriched gas gives a factor of 3 improvement in signal intensity over the Xe (26.4% ^{129}Xe) in A. An improvement in the SNR between (a) and (c) is apparent. (d) A repeat of (c) using the piston extraction-compression unit. Images (c) and (d) are almost identical showing that the simple balloon extraction-compression unit is adequate for ^{129}Xe imaging experiments. (e-h) Non-slice selective images corresponding to (a-d).*

4.4.4 *Ex vivo* ^{83}Kr lung imaging

Fig. 4.10 displays three coronal images taken using ^{83}Kr in *ex vivo* rat lungs. For the first time images that display anatomical features can be recorded in a single scan. A 32-increment gradient-echo imaging sequence was used. The bulk of the lung and its shape (the alveolar region) are visible in all images, and the major airways (trachea and bronchi) are clearly visible for the image using enriched gas (Fig. 4.10c).

Fig. 4.10a uses research grade ^{83}Kr (11.5 % ^{83}Kr) resulting in a lower signal-to-noise than when enriched gas is used (enriched to 99.925 % ^{83}Kr). The use of enriched gas should have improved the signal-to-noise by a factor of 8.7. While an improvement is clear, a signal spectrum NMR experiment showed that the signal only improved by a factor of 5.5. It is likely that the improvement is reduced due to degradation in the SEOP cell between the initial tests of the SEOP cell and taking the enriched ^{83}Kr image as a number of hours passed in between. This is being investigated further, but is beyond the scope of this thesis.

As a result of the observed SEOP cell degradation, the polarization value expected for Fig. 4.10c would be overestimated. As with ^{129}Xe, averaging over four scans (Figs. 4.10b) resulted in an improved image quality (estimated as a factor of two).

An almost two-fold improvement can still, in principle, be achieved for ^{83}Kr without major improvements to the apparatus. Maximum apparent polarization shown in Fig. 4.7 is lower than the maximum polarization achieved earlier in the work (**Chapter 3**). Higher-than-necessary SEOP cell pressures were also used in this study. Reducing the size of the transfer lines (and therefore the necessary volume of gas) would decrease the minimum SEOP cell pressure. With these two considerations in mind an apparent polarization after recompression of $P_{ex\text{-}com}$ = 3.8% should be achievable with no significant improvements to the system.

Hp gas can be delivered after 8 minutes (~80% of the full build) however for imaging typically 12 minutes are used for imaging experiments (~90% of the full build).

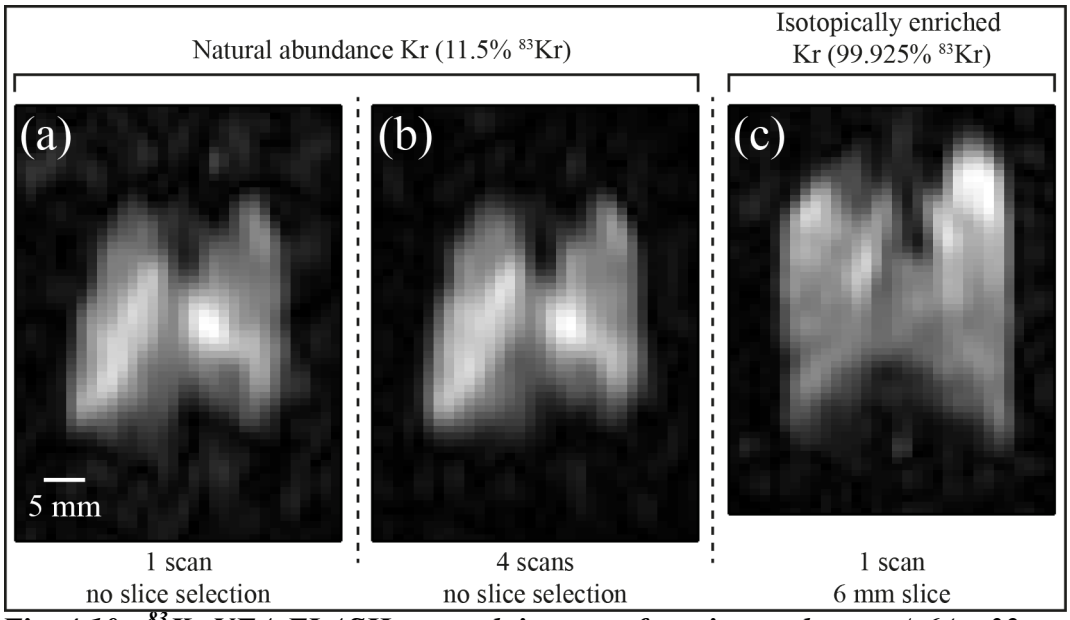

Fig. 4.10 - ^{83}Kr VFA FLASH coronal, images of ex vivo rat lung. *. A 64 x 32 matrix was used, with zero filling in the direct dimension. (**a**) A single non-slice selective ^{83}Kr rat lung image. The alveolar space of the two distinct lungs is visible. FOV = 51.0 x 38.1 mm^2. (**b**) Four images similar to (a) over different inhalation cycles where averaged together to improve the SNR (SNR should improve by a factor of 2). (**c**) A single 6 mm (central) slice selective ^{83}Kr rat lung image using isotopically enriched Kr (^{83}Kr). The use of enriched gas gives a factor of almost 9 improvement in signal intensity over the Kr (11.5 % 83Kr) in A. Major airways are now visible. A different set of rat lungs was used in (c) than (a) and (b). FOV = 50.9 x 40.7 mm^2.*

4.4.5 T_1 weighted *ex vivo* ^{83}Kr lung imaging

Slice selective imaging allows spatially resolved T_1 relaxation measurements within the lung. Fig. 4.11 shows four slice-selective images. Fig. 4.11a was acquired with no delay time before the sequence was run. Each subsequent image was run after a stated delay. Fig. 4.11e shows a plot of the T_1 values calculated for each pixel inside of the lung.

Using Fig. 4.11e a samples of T_1 values could be extracted to acquire the T_1 values for different regions in the lung. It was seen that the major airways had the longest T_1 times, with ^{83}Kr in the trachea having a T_1 of 7.4±2.6 seconds and the bronchus having a T_1 time of 4.2±0.4 seconds. The ^{83}Kr in the bulk of the alveolar space had a T_1 time of 1.1±0.2 seconds. This seems to agree with Fig. 4.11c+d. T_1 times at the periphery of the lung were slightly shorter with the ^{83}Kr T_1 being 0.9±0.1 seconds. This relationship makes sense as the ^{83}Kr should not relax as quickly in regions where there is a small surface-to-volume ratio (the large airways) compared to regions with a large surface to volume (the alveolar space). Previous work looking at spatially unresolved ^{83}Kr T_1 *ex vivo* are in agreement with the values presented here [29].

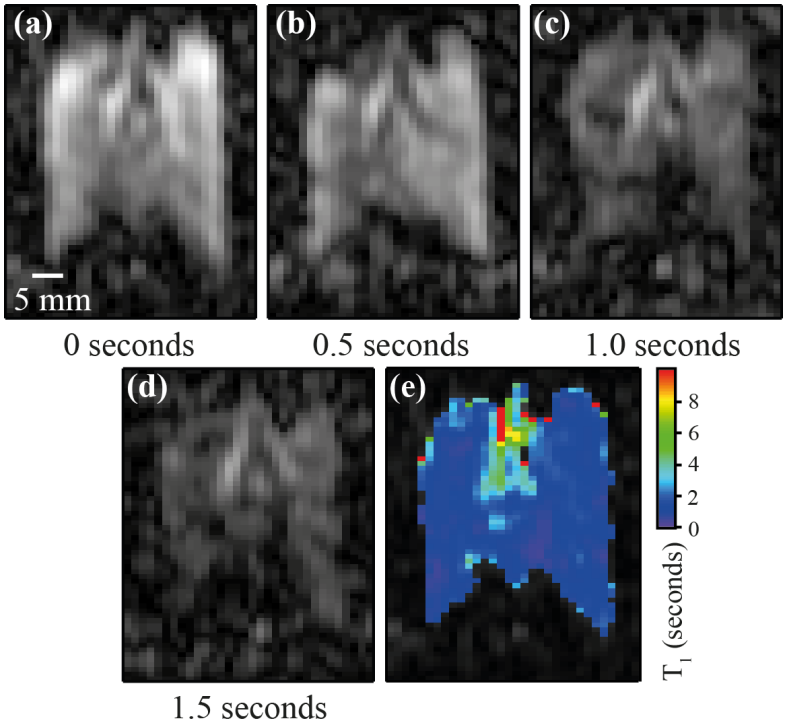

Fig. 4.11 – Ex vivo coronal rat lung images of hp ^{83}Kr at different time increments (t_d). *32 gradient increments and 3 mm slice selection used. Anatomical structures such as the alveolar region and bronchi can be distinguished.* ***(a)*** *Single scan after a delay time t_d = 0 seconds* ***(b)*** *t_d = 0.5 seconds. Overall signal intensity has weakened over the entirety of the lung.* ***(c)*** *t_d = 1.0 seconds. Additional reductions in the overall signal are visible, in particular in the peripheries and at the base of the lung.* ***(d)*** *t_d = 1.5 seconds. Signal in the major airways was similar to (a) however there is now little signal from the alveolar region.* ***(e)*** *T_1 map of lung. Signal intensities for each pixel inside of the lung taken from the four images were used to calculate T_1 times. T_1 times in the major airways are clearly longer than those in the alveolar region.*

4.4.6 Polarization as a function of SEOP cell pressure data fittings

To further qualify that the presented data is in agreement with literature values, a range of data points for the 24.8 % Kr, 75.2 % N_2 and 25.0 % Xe, 75.0 % N_2 curves from Fig. 4.7 and Fig. 4.8a have been fit to Eq. 4.1. The plots of these fittings are not presented in this work.

$$P = f \cdot \frac{c^{Rb} \cdot \gamma_{SE}^{calc}}{c^{Rb} \cdot \gamma_{SE}^{calc} + \Gamma(p)} \cdot \frac{\gamma_{op}}{\gamma_{op} + \gamma_{trap} + \gamma_{vdW} + \sum_{i \neq Rb} \kappa_{sd}^{i}[M_i] \cdot c^{Rb}[Rb]}$$

[Eq. 4.1]

Many of the terms in this equation have been discussed previously in **Chapter 3**, relating to Eq. 3.2. γ_{op} was used as a fitting parameter for both Kr and Xe.

γ_{vdW} was also a fitting parameter for Xe, and $\gamma_{trap}^{[N_2]=0}$ a fitting parameter for Kr. Fitting was conducted to allow for a comparison between this data and the values collected by Six *et al.* where the same analysis was carried out [3]. Analysis has been conducted exactly as described in that paper and uses all of the same literature values for rate constants. The values given in Table 4.3 are in agreement with the literature values within the error boundaries. The large errors (especially on γ_{vdW} for ^{129}Xe) are due to fewer data points being collected for the two curves for this study. Fitting data points over a greater range of pressures also contributed to high error values.

Table 4.3 *- Fitting parameter γ_{op} for both Kr and Xe. Other fitting parameters γ_{vdW} for Xe, and $\gamma_{trap}^{[N_2]=0}$ for Kr are also given. Parameters extracted by fitting experimental values of Kr and Xe apparent polarization as a function of SEOP cell pressure to Eq. 4.1.*

Mixture	γ_{op} $(10^3\ s^{-1})$	γ_{vdW} $(10^3\ s^{-1})$	$\gamma_{trap}^{[N_2]=0}$ $(10^3\ s^{-1})$
24.8 % Kr; 75.2 % N_2	2.38 ± 0.12	-	97 ± 18
25.0 % Xe; 75.0 % N_2	18.7 ± 1.3	1.9 ± 1.5	-

4.4.7 Rb vapour removal

A potential issue with the gas delivery method outlined in this work is Rb contamination of the gas mixtures. Other methods that employ cryogens do not experience this problem, as Rb vapour will plate out onto the storage container when the gas is cooled. After the storage step, the gas will not be warmed sufficiently for the Rb to re-enter the vapour phase. As this technique omits a cryogenic step it is important to determine the quantity of Rb that is present in the final gas mixture. Here some crude experiments have been conducted to try and roughly determine the quantity of Rb present and explore the use of glass wool filters to remove present Rb. While this is sufficient for *ex vivo* studies a more rigorous investigation will be required before the technique can be employed *in vivo*. **Section 4.4.8.2** discusses potential future experiments to both determine Rb concentration, and methods that could be employed to remove Rb from gas mixtures.

4.4.7.1 Rb vapour removal and evaluation experiments

A series of filters where installed into the delivery system to explore the Rb concentration present in the hp gas mixture (as described in **Section 4.3.9** and **Fig. 4.1**). The greatest observed change in the water pH due to the introduction of a used Rb filter was +2.5. This was observed after 40 cycles and with the most *extreme* conditions experienced in terms of potential transfer of Rb vapour. The piston extraction-compression unit was used, which extracted more gas than its balloon counterpart, and also increased the increased the gas

transfer rate due to the greater pressure differential when the SEOP cell is opened.

Filter positioning, as well as the different conditions under which experiments were conducted, and associated pH change values are detailed in **Table 4.4**. This includes looking at the system with two filters installed: Preliminary results suggest that a single filter of the design described is not adequate to completely remove Rb vapour.

A pH change as little as +2.5 is unlikely to be physiologically damaging to excised rodent lungs after a few extraction-compression events without the presence of a filter (as experienced in this work).

Preliminary results have also observed that 88 % of ^{83}Kr polarization survives when a filter containing 200 g of glass wool at position **A** is used.

Table 4.4 *– pH change of distilled water when a used Rb vapour filter is introduced. pH change values are presented as well as the number of extraction-compression cycles responsible for the change, the filter(s) position(s), the extraction-compression modality, and other relevant notes. Filter positions are described in Fig. 4.1.*

Number of extraction-compression cycles	***Extraction-compression modality***	Filter 1 position	Filter 2 position	**pH change for filter 1**	**pH change for filter 2**	**Notes**
10	*Balloon*	**C**	N/A	0	N/A	N/A
20	*Balloon*	**C**	N/A	+1	N/A	N/A
30	*Balloon*	**C**	N/A	+1	N/A	N/A
5	*Balloon*	**A**	N/A	+2	N/A	N/A
10	*Balloon*	**A**	N/A	+2	N/A	N/A
40	*Piston*	**A**	**B**	+2.5	+1	N/A
5	*Balloon*	**A**	N/A	+1	N/A	200 g of glass wool used in each filter, only 0.5 ml of water introduced to wash
30	*Balloon*	**A**	**C**	+1	+1.5	200 g of glass wool used in each filter, only 0.5 ml of water introduced to wash

4.4.7.2 Potential further work to remove Rb vapour

As evident from the experiments above, further work in removing Rb vapour is required before this methodology can be applied to an *in vivo* system. A very simple improvement that could be implemented is the use of an electronic pH

meter instead of universal indicator paper. Indicator paper is really only accurate to ± 0.5 pH and even then readings are somewhat subjective. Even a cheap pH meter can have an accuracy of ± 0.01 pH and provides a result that is not biased by the experimenter's interpretation. A repeat of the study above using a pH meter, rather than indicator paper will not likely come to a different conclusion, but should have more accurate results.

Further to this, a more accurate method to determine exactly how much Rb was leaving the SEOP cell would be to take the weight of the cell itself. By taking the weight of the empty SEOP cell, the SEOP cell after it is filled with Rb but before experiments are conducted, and then taking the weight after experiments. This would not take into account any additional weight potentially introduced by contaminants entering the SEOP cell, however significant contamination should be visibly observable. This method will also only give a maximum indicator of the Rb entering the lung or delivery cell. It is likely that much of the Rb will condense onto transfer lines between the SEOP cell outlet and the lung.

While other techniques may make determining Rb concentration in the delivery system more accurate, it is of greater interest to find a method of removing Rb from the gas delivered. One extraction-compression device investigated in the preliminary experiments of this study involved using a moving column of water to compress the gas (a bit like a Toepler pump with water replacing mercury). This had the advantage of completely removing the Rb as it would react with the column of water. Unfortunately this design was discarded due to polarization losses and the fact that it was technically difficult to operate. It is possible that a simple glass wool filter soaked in water may prove to be effective enough to remove the Rb in the delivery system. Experiments should be conducted to investigate whether complete Rb removal is achieve, as well as to see if polarization losses are incurred by said filter.

Another possible solution would be to introduce a 'cold trap' into the system (i.e. a piece of glass delivery line that passes through liquid N_2). Rb might plate out completely given the significant temperature difference. This is not ideal, as it reintroduces a cryogenics step into an otherwise 'cryogen free' procedure (and for ^{129}Xe it might be argued that if cryogens are re-introduced then the isotope should be frozen out completely to increase the apparent polarization). There is also a possibility that the ^{83}Kr will sublime under these temperatures, resulting in rapid quadrupolar relaxation [6, 7]. Regardless, further work should investigate the viability of this method if a wet glass filter is insufficient.

4.5 Conclusion

This work shows that compression of a low-pressure hp ^{83}Kr gas mixtures is possible using a simple extraction-compression apparatus. After an extraction-compression cycle an apparent polarization of 2.9 ± 0.0 % is possible using 24.8 % Kr, 75.2 % N_2 and the piston extraction-compression apparatus. Other, even simpler, extraction-compression methodology has been explored

thoroughly with ^{129}Xe where an apparent polarization of 14.7 ± 0.2 % is possible after an extraction-compression cycle with a 39.6 % Xe, 60.4 % N_2 gas mixture.

The methods described in this work allow for the generation of high polarization, high noble gas concentration gas mixtures at the pressure necessary for lung studies (101 kPa).

The technique has further been used to obtain *ex vivo* rat lung images: FOV = 46.9 x 30.0 mm^2 in a 128 x 64 matrix achieved using 64 gradient increments for ^{129}Xe. All images show structural details of the lungs. Averaging a number of scans or using isotopically enriched ^{129}Xe is shown to increase the signal-to-noise ratio as expected.

Ex vivo ^{83}Kr rat lung images have been presented with both isotopically enriched, and non-isotopically enriched gas used. ^{83}Kr imaging using the technique described has, for the first time, allowed the acquisition of slice-selective coronal images; these images were each acquired with a single scan and 32 gradient increments. Slice selective imaging has been used to show spatially resolved T_1 measurements in excised rat lungs.

A brief study using simple Rb filters has shown that the quantity of Rb reaching the excised lung is minimal. A simple glass-wool filter (allowing 88 % of ^{83}Kr polarization to survive) can remove most of the Rb vapour, although further work will be needed before cryogen-free hp gas production can be use in an *in vivo* system.

Further improvements are still desirable for ^{83}Kr recompression where about a sixth of polarization is still lost around the optimal SEOP cell pressure. This may be avoided by using materials that are known to not significantly shorten ^{83}Kr T_1 times in the construction of the recompression apparatus. Continuing work will investigate modifying the bespoke axial piston pump.

4.5.1 Further work to allow for human *in vivo* studies

Another step to overcome before this system can be used for larger animals or human *in vivo* studies is the limited volume of hp gas produced. In a typical breath-hold experiment 1 l of gas might be inhaled. ^{129}Xe can be stored for a few hours, or frozen allowing for longer storage times; in this interval additional gas deliveries can be accumulated offering at least a partial solution to the issue of volume. This will not be adequate for ^{83}Kr studies due to rapid quadrupolar surface relaxation; therefore the final system will ideally need to produce 1 l of hp gas (at or slightly above 101 kPa) in a single batch. In principle an up scaling of the SEOP system would require a larger polarizer and extraction-compression chamber.

For most of the work described in this thesis 23.3 W of laser power is employed. Far more powerful line-narrowed diode lasers do exist, and the use of a more powerful laser with a bigger telescope optic could allow for SEOP

cells with a larger diameter. Longer cells could be investigated also, however the presence of an optically thick layer of Rb at the front of the SEOP cell [46] might make a long-cell design less efficient (see **Section 3.3.4.1**). It is likely that practical limitations will necessitate the use of multiple *large* cells, optically pumped using a number of lasers, to generate sufficient gas.

Physically larger cells will require the constituent glass to be thicker if the same range of operating pressures is still desired. Thicker glass introduces two potential problems. The first is that the heating dynamics may not be the same: although re-calibration of the optimal temperature should negate that. The second more serious issue is that a significant amount of laser light may be scattered entering the cell due to the presence of additional glass. It may be necessary to increase the flux density of the laser used to achieve the same results as with a cell made of thinner glass.

Another set of calibration experiments that will be crucial when using larger SEOP cells is to ascertain the optimal quantity of Rb. The quantity of Rb necessary was only briefly explored in this thesis, finding that any more than 1 g seemed to make little difference. Larger cells will require a greater amount of Rb.

The final consideration is gas handling, which is discussed throughout this chapter. A larger piston extraction-compression unit would likely prove to be the most efficient device, as the larger surface-to-volume ratio would reduce the T_1 relaxation experienced by the gas. The exact size of the chamber would depend on the SEOP pressure used, and size of cells employed, however given optimal pressures of about 50 kPa for ^{83}Kr, and the need for the final volume of gas to be ~1 l, a piston extraction-compression device may need a volume as large as 20 l to extract sufficient gas. Practically it might be difficult to fabricate such a large unit (and control pneumatically). Individual compression units corresponding to individual SEOP cells could be employed, compressing gas into a joint reservoir. The major disadvantage to this method is the time taken to transfer all of the gas (relative to the short T_1 time of ^{83}Kr). Automation of the extraction-compression units could allow for them to compress simultaneously, avoiding this problem.

4.6 References

[1] T. Hughes-Riley, J.S. Six, D.M.L. Lilburn, K.F. Stupic, A.C. Dorkes, D.E. Shaw, G.E. Pavlovskaya, T. Meersmann, Cryogenics free production of hyperpolarized 129Xe and 83Kr for biomedical MRI applications, Journal of Magnetic Resonance, 237 (2013) 23-33.
[2] J.S. Six, T. Hughes-Riley, D.M.L. Lilburn, A.C. Dorkes, K.F. Stupic, D.E. Shaw, P.G. Morris, I.P. Hall, G.E. Pavlovskaya, T. Meersmann, Pulmonary MRI contrast using Surface Quadrupolar Relaxation (SQUARE) of hyperpolarized 83Kr, Magnetic Resonance Imaging, 32(1) (2014) 48-53.
[3] J.S. Six, T. Hughes-Riley, K.F. Stupic, G.E. Pavlovskaya, T. Meersmann, Pathway to cryogen free production of hyperpolarized krypton-83 and xenon-129, Plos One (in press), 8(8) (2012) e73468.

[4] N.N. Kuzma, B. Patton, K. Raman, W. Happer, Fast nuclear spin relaxation in hyperpolarized solid Xe-129, Physical Review Letters, 88 (2002) 147602.
[5] G. Schrank, Z. Ma, A. Schoeck, B. Saam, Characterization of a low-pressure high-capacity 129Xe flow-through polarizer, Physical Review A, 80 (2009) 063424.
[6] D.F. Cowgill, R.E. Norberg, Pulsed Nmr-Studies of Self-Diffusion and Defect Structure in Liquid and Solid Krypton, Physical Review B, 13 (1976) 2773-2781.
[7] D.F. Cowgill, R.E. Norberg, Spin-Lattice Relaxation and Chemical-Shift of Kr-83 in Solid and Liquid Krypton, Physical Review B, 8 (1973) 4966-4974.
[8] H. Imai, J. Fukutomi, A. Kimura, H. Fujiwara, Effect of reduced pressure on the polarization of Xe-129 in the production of hyperpolarized Xe-129 gas: Development of a simple continuous flow mode hyperpolarizing system working at pressures as low as 0.15 atm, Concepts in Magnetic Resonance Part B-Magnetic Resonance Engineering, 33B (2008) 192-200.
[9] F.D. Colegrove, L.D. Schearer, G.K. Walters, Polarization of He^{3} Gas by Optical Pumping, Physical Review, 132 (1963) 2561-2572.
[10] T.R. Gentile, G.L. Jones, A.K. Thompson, R.R. Rizi, D.A. Roberts, I.E. Dimitrov, R. Reddy, D.A. Lipson, W. Gefter, M.D. Schnall, J.S. Leigh, Demonstration of a compact compressor for application of metastability-exchange optical pumping of 3He to human lung imaging, Magnetic Resonance in Medicine, 43 (2000) 290-294.
[11] T.R. Gentile, D.R. Rich, A.K. Thompson, W.M. Snow, G.L. Jones, Compressing spin-polarized [3]He with a modified diaphragm pump, National Institute of Standards and Technology, Gaithersburg, MD, ETATS-UNIS, 2001.
[12] R.S. Timsit, J.M. Daniels, E.I. Dennig, A.K.C. Kiang, A.D. May, An Experiment to Compress Polarized 3He Gas, Canadian Journal of Physics, 49 (1971) 508-516.
[13] G. Eckert, W. Heil, M. Meyerhoff, E.W. Otten, R. Surkau, M. Werner, M. Leduc, P.J. Nacher, L.D. Schearer, A dense polarized 3He target based on compression of optically pumped gas, Nuclear Instruments and Methods in Physics Research Section A: Accelerators, Spectrometers, Detectors and Associated Equipment, 320 (1992) 53-65.
[14] W. Heil, K. Andersen, D. Hofmann, H. Humblot, J. Kulda, E. Lelievre-Berna, O. Schärpf, F. Tasset, 3He neutron spin filter at ILL, Physica B: Condensed Matter, 241-243 (1997) 56-63.
[15] D.S. Hussey, D.R. Rich, A.S. Belov, X. Tong, H. Yang, C. Bailey, C.D. Keith, J. Hartfield, G.D.R. Hall, T.C. Black, W.M. Snow, T.R. Gentile, W.C. Chen, G.L. Jones, E. Wildman, Polarized ^{3}He gas compression system using metastability-exchange optical pumping, Review of Scientific Instruments, 76 (2005) 053503-053512.
[16] W.M. Snow, Neutron Polarizers Based on Polarized 3He, in, 2005, pp. Medium: ED.
[17] G. Eckert, W. Heil, M. Meyerhoff, E.W. Otten, R. Surkau, M. Werner, M. Leduc, P.J. Nacher, L.D. Schearer, A Dense Polarized He-3 Target Based on Compression of Optically Pumped Gas, Nuclear Instruments & Methods in Physics Research Section A-Accelerators Spectrometers Detectors and Associated Equipment, 320 (1992) 53-65.

[18] J. Becker, W. Heil, B. Krug, M. Leduc, M. Meyerhoff, P. Nacher, E. Otten, T. Prokscha, L. Schearer, R. Surkau, Study of mechanical compression of spin-polarized ^{3}He gas, Nuclear Instruments and Methods in Physics Research Section A: Accelerators, Spectrometers, Detectors and Associated Equipment, 346 (1994) 45-51.
[19] R. Surkau, J. Becker, M. Ebert, T. Grossmann, W. Heil, D. Hofmann, H. Humblot, M. Leduc, E.W. Otten, D. Rohe, K. Siemensmeyer, M. Steiner, F. Tasset, N. Trautmann, Realization of a broad band neutron spin filter with compressed, polarized 3He gas, Nuclear Instruments and Methods in Physics Research Section A: Accelerators, Spectrometers, Detectors and Associated Equipment, 384 (1997) 444-450.
[20] E. Stoltz, M. Meyerhoff, N. Bigelow, M. Leduc, P.J. Nacher, G. Tastevin, High nuclear polarization in ^{3}He and ^{3}He-^{4}He gas mixtures by optical pumping with a laser diode, Applied Physics B, 63 (1996) 629-633.
[21] T.R. Gentile, Method and apparatus for compression of polarized gas, in, The United States of America, as represented by the Secretary of Commerce, United States, 2000, pp. 6.
[22] S. Fichele, Hyperpolarised 3He Gas Production for Magnetic Resonance Imaging of the Human Airways, in: School of Physics and Astronomy, The University of Nottingham, Nottingham, 2002.
[23] M.O. Mada, Application of Hyperpolarised Helium-3 in Lung Functional Magnetic Resonance Imaging, in: School of Physics and Astronomy, University of Nottingham, Nottingham, 2009.
[24] P.J. Nacher, Peristaltic compressors suitable for relaxation-free compression of polarized gas, in, Centre National de la Recherche Scientifique CNRS, United States, 2003.
[25] M.S. Rosen, T.E. Chupp, K.P. Coulter, R.C. Welsh, S.D. Swanson, Polarized Xe-129 optical pumping/spin exchange and delivery system for magnetic resonance spectroscopy and imaging studies, Review of Scientific Instruments, 70 (1999) 1546-1552.
[26] S.D. Swanson, M.S. Rosen, B.W. Agranoff, K.P. Coulter, R.C. Welsh, T.E. Chupp, Brain MRI with laser-polarized Xe-129, Magnetic Resonance in Medicine, 38 (1997) 695-698.
[27] Z.I. Cleveland, G.E. Pavlovskaya, K.F. Stupic, C.F. LeNoir, T. Meersmann, Exploring hyperpolarized 83Kr by remotely detected NMR relaxometry, Journal of Chemical Physics, 124 (2006) 044312.
[28] L. Zhao, R. Mulkern, C.H. Tseng, D. Williamson, S. Patz, R. Kraft, R.L. Walsworth, F.A. Jolesz, M.S. Albert, Gradient-echo imaging considerations for hyperpolarized Xe-129 MR, Journal of Magnetic Resonance Series B, 113 (1996) 179-183.
[29] K.F. Stupic, N.D. Elkins, G.E. Pavlovskaya, J.E. Repine, T. Meersmann, Effects of pulmonary inhalation on hyperpolarized krypton-83 magnetic resonance T-1 relaxation, Physics in Medicine and Biology, 56 (2011) 3731-3748.
[30] Z.I. Cleveland, K.F. Stupic, G.E. Pavlovskaya, J.E. Repine, J.B. Wooten, T. Meersmann, Hyperpolarized ^{83}Kr and ^{129}Xe NMR Relaxation Measurements of Hydrated Surfaces: Implications for Materials Science and Pulmonary Diagnostics, Journal of the American Chemical Society, 129 (2007) 1784-1792.

[31] C.J. Jameson, A.K. Jameson, J.K. Hwang, Nuclear-Spin Relaxation by Intermolecular Magnetic Dipole Coupling in the Gas-Phase - Xe-129 in Oxygen, Journal of Chemical Physics, 89 (1988) 4074-4081.
[32] J.S. Six, T. Hughes-Riley, K.F. Stupic, G.E. Pavlovskaya, T. Meersmann, Pathway to Cryogen Free Production of Hyperpolarized Krypton-83 and Xenon-129, PLOS ONE, 7 (2012) e49927.
[33] K.F. Stupic, Z.I. Cleveland, G.E. Pavlovskaya, T. Meersmann, Quadrupolar Relaxation of Hyperpolarized Krypton-83 as a Probe for Surfaces, Solid State Nuclear Magnetic Resonance, 29 (2006) 79-84.
[34] G.E. Pavlovskaya, Z.I. Cleveland, K.F. Stupic, T. Meersmann, Hyperpolarized Krypton-83 as a New Contrast Agent for Magnetic Resonance Imaging, Proceedings of the National Academy of Sciences of the United States of America, 102 (2005) 18275-18279.
[35] Z.I. Cleveland, K.F. Stupic, G.E. Pavlovskaya, J.E. Repine, J.B. Wooten, T. Meersmann, Hyperpolarized Kr-83 and Xe-129 NMR relaxation measurements of hydrated surfaces: Implications for materials science and pulmonary diagnostics, Journal of the American Chemical Society, 129 (2007) 1784-1792.
[36] Z.I. Cleveland, T. Meersmann, Binary Collision Induced Longitudinal Relaxation in Gas-Phase 83K, Journal of Chemical Physics, submitted (2008).
[37] D. Brinkmann, D. Kuhn, Nuclear Magnetic-Relaxation of Kr-83 in Krypton Gas, Physical Review A, 21 (1980) 163-167.
[38] Z.I. Cleveland, T. Meersmann, Density-independent contributions to longitudinal relaxation in Kr-83, Chemphyschem, 9 (2008) 1375-1379.
[39] B. Chann, I.A. Nelson, L.W. Anderson, B. Driehuys, T.G. Walker, Xe-129-Xe molecular spin relaxation, Physical Review Letters, 88 (2002) 113201.
[40] R.L. Gamblin, T.R. Carver, Polarization and Relaxation Processes in He^{3} Gas, Physical Review, 138 (1965) A946-A960.
[41] L.D. Schearer, G.K. Walters, Nuclear Spin-Lattice Relaxation in Presence of Magnetic-Field Gradients, Physical Review, 139 (1965) 1398-1402.
[42] W. Zheng, Z.I. Cleveland, H.E. M√∂ller, B. Driehuys, Gradient-induced longitudinal relaxation of hyperpolarized noble gases in the fringe fields of superconducting magnets used for magnetic resonance, Journal of Magnetic Resonance, 208 284-290.
[43] R.W. Mair, D.G. Cory, S. Peled, C.-H. Tseng, S. Patz, R.L. Walsworth, Pulsed-Field-Gradient Measurements of Time-Dependent Gas Diffusion, Journal of Magnetic Resonance, 135 (1998) 478-486.
[44] R.E. Jacob, B. Driehuys, B. Saam, Fundamental mechanisms of He-3 relaxation on glass, Chemical Physics Letters, 370 (2003) 261-267.
[45] H.E. Möller, Z.I. Cleveland, B. Driehuys, Relaxation of hyperpolarized 129Xe in a deflating polymer bag, Journal of Magnetic Resonance, 212 109-115.
[46] M.E. Wagshul, T.E. Chupp, Optical-Pumping of High-Density Rb with a Broad-Band Dye-Laser and Gaalas Diode-Laser Arrays - Application to He-3 Polarization, Physical Review A, 40 (1989) 4447-4454.

Chapter 5

Exploring T_1 relaxation as a function of oxygen density on model surfaces

Acknowledgements

Of the work presented in this chapter some was included in the published Journal of Magnetic Resonance [1] *Cryogenics free production of hyperpolarized ^{129}Xe and ^{83}Kr for biomedical MRI applications*. The author list was **Theodore Hughes-Riley**, Joseph S. Six, David M.L. Lilburn, Karl F. Stupic, Alan C. Dorkes, Dominick E. Shaw, Galina E. Pavlovskaya, and Thomas Meersmann.

Experiments were carried out by Theodore Hughes-Riley, Joseph S. Six, and David Lilburn.

The high-pressure mixing apparatus in this work was designed and built by Theodore Hughes-Riley with assistance from Dr. Karl F. Stupic**.** Theodore Hughes-Riley optimized the mixing methodology. The piston extraction-compression device used for low pressure mixing was designed by Theodore Hughes-Riley with input from Prof. Thomas Meersmann and Mr. Alan C. Dorkes. Mr. Alan C. Dorkes physically constructed the unit. As before, Theodore Hughes-Riley developed the mixing methodology.

Some of the MR spectroscopy experiments where conducted solely by Theodore Hughes-Riley, although occasionally assistance was given by either Joseph S. Six or Dr. David M.L. Lilburn, who would run the spectrometer. Data would be processed by Theodore Hughes-Riley. The pulse sequence used for the experiments presented in this chapter was written by Dr. Karl F. Stupic and processed using a macro written by Dr. Karl F. Stupic and Theodore Hughes-Riley. Dr. Karl F. Stupic and Theodore Hughes-Riley also wrote another sequence for a different spectrometer (a Magritek Kea 2) used in a number of the preliminary experiments (not shown here).

Imaging experiments involved three people: Theodore Hughes-Riley, Joseph S. Six and Dr. David M.L. Lilburn. Dr. David M.L. Lilburn was responsible for lung extractions (normally assisted by Theodore Hughes-Riley). Theodore Hughes-Riley would run the gas delivery system and perform most of the data processing. Joseph S. Six would be responsible for the polarizer, and Dr. David M.L. Lilburn would run the spectrometer. (While this was how experiments were normally conducted there was some flexibility in the roles people took).

Theodore Hughes-Riley prepared the figures in this chapter.

5.1 Introduction and background

Understanding the relaxation rates of hyperpolarized gas is important for *in vivo* MRI studies: An aspect of this is to understand the gas phase relaxation in the presence of O_2, a vital component of any *in vivo* gas mixture. Molecular oxygen has two unpaired electrons and is therefore paramagnetic. As a result of this O_2 is often the dominant cause of longitudinal relaxation for some nuclei (e.g. ^{3}He, ^{129}Xe; both $I = 1/2$) even in modest concentrations [2, 3]. As a consequence this has been explored by some groups as a form of contrast for hp ^{3}He MRI [4-9]. The possibility of developing ^{129}Xe O_2 mapping has also been examined [10].

Due to the non-thermal polarization of the noble gas, O_2 dominated relaxation will limit the lifetime of the hyperpolarization of ^{129}Xe. Therefore it is important to understand T_1 relaxation as a function of O_2 concentration in the lung. It is also important to be able to quantify such relaxation behaviour when mixing and storing breathable gas mixtures. The behaviour of ^{3}He was characterized by Samm *et al.* [3] where relaxation rate increased linearly with O_2 concentration, a relationship described by Jameson *et al.* for intermolecular dipolar relaxation [2] such as this.

Jameson *et al.* previously applied this theory to their study of ^{129}Xe in the presence of oxygen [2]. Relying on the thermal polarization signal of various high-pressure samples, Jameson *et al.* experimentally explored the T_1 relaxation of ^{129}Xe in the presence of oxygen. This dependence, which was observed to be linear, was examined at different temperatures and magnetic field strengths allowing for the various factors contributing to the intermolecular relaxation mechanism to be characterized and scrutinised. Samples were stored within glass, meaning that surface relaxation of the ^{129}Xe was negligible and that oxygen was the dominating cause of relaxation even when in scarce quantities.

Kraayvanger *et al.* re-examined this relationship using a hyperpolarized system [11]. While their experiments were conducted at a lower magnetic field (74 mT) than either of those explored by Jameson *et al.* (4.7 T and 9.4 T) this result did in principle agree with previous findings.

Experiments have also been run to determine how the ^{129}Xe T_1-O_2 dependence changes under different circumstances (i.e. not in the gas phase). Wolber *et al.* [12] have explored ^{129}Xe T_1 relaxation with various O_2 densities is when both gases are dissolved in blood. This work demonstrated that the relationship in this case is non-linear at high O_2 concentrations. The authors identify one possibility for the non-linearity being due to chemical changes in the haemoglobin that occur when the oxygen binds with it. This affects a paramagnetic Fe ion that would induce ^{129}Xe relaxation; therefore deoxyhaemoglobin relaxes ^{129}Xe more rapidly than oxyhaemoglobin (in an earlier work [13], Wobler *et al*. observe a ^{129}Xe T_1 in 96.3 % oxygenated haemoglobin as 6.42 ± 0.50 s as opposed to a T_1 = 3.71 ± 0.22 s in 67.2 % oxygenated haemoglobin).

It is believed that when in the presence of a surface, or structure, the relationship between the O_2 density and T_1 relaxation should not change. Indeed, while studying Xe diffusion within glass bead samples, Mair *et al.* measured their ^{129}Xe T_1 as a function of O_2 density for their system in a free gas sample [14] (which was in agreement with Jameson *et al.*). This relationship was then used to determine pO_2 in glass-bead containing cells. High-pressure thermally polarized ^{129}Xe was used in this study. Confirmation that the relationship held true in samples containing glass beads was not resolved.

At the time that this research was conducted [15], little work in the literature had examined the effect of a porous medium on the T_1-O_2 dependence. Pasquier *et al.* have taken ^{129}Xe T_1 values for two O_2 concentrations in a type of porous glass (Vycor) [16]. Values where only taken in the absence of O_2 and with 10 % O_2. While this seemed to give a relationship similar those previously reported, the relationship cannot be fully characterized without additional data points. It is also quite possible that this is not an adequate indicator of the T_1 dependence of ^{129}Xe in the presence of O_2 in a lung or similar material.

It is therefore of interest to examine the ^{129}Xe T_1 relaxation as a function of O_2 in porous media, in particular in excised lungs, at high O_2 densities. Both Xe and O_2 are known to readily dissolve: For example in porous structures, such as the lung where 1 % of Xe will dissolve into the tissue. Different molecular interactions in the dissolved phase may lead to very different T_1 times. Given exchange of Xe between the dissolved tissue phase and gas phase, it is possible that different relaxation times in the dissolved phase may alter the gas phase T_1 value if the gas exchange is fast enough, and difference in T_1 times significant. Confirming this characterization will be useful for future work exploring T_1 mapping in the lungs with ^{129}Xe.

An *ex vivo* model will be utilized in this work as it offers two advantages over an *in vivo* model. Firstly, it allows for breath holds on the order of minutes, which is necessary to determine the longer T_1 times at very low O_2 densities. The *ex vivo* model also allows for the use of low quantities of O_2 without the need for additional ethical clearances.

The T_1 relaxation of ^{83}Kr in the presence of O_2 is largely unexplored. Some T_1 measurements in the literature have studied T_1 relaxation in the presence of O_2 in desiccated and excised tissue [17, 18]. In both cases the T_1 of ^{83}Kr is shown to be fairly insensitive to the presence of O_2 (the largest change being a 20 % drop in T_1 time in the presence of 20 % O_2). This is unsurprising as, due to its nuclear-electric quadrupole moment, the T_1 of ^{83}Kr is dominated by surface interactions [18]. ^{83}Kr also possess a lower gyromagnetic ratio than ^{129}Xe resulting it in being less sensitive to paramagnetism (shown in Eq. 5.3 below). Lung tissue has a large surface, and will be responsible for the short T_1 times experienced by ^{83}Kr in the lung (with O_2 contributing little). However, the contribution of O_2 in bulk gas phase has not been studied quantitatively and is of interest as the mixing of the hp ^{83}Kr and O_2 will be an important step prior to *in vivo* studies.

This work will re-examine the relaxation of ^{129}Xe as a function of O_2 densities. Once a technique to adequately mix the hp gas and oxygen is developed, the T_1 time as a function of O_2 density will be determined in both an artificial porous medium and in excised rat lungs. Further to this, ^{83}Kr T_1 relaxation as a function of O_2 density in the gas phase will be characterized.

The piston extraction-compression apparatus described in **Chapter 4** has also been to pre-mixing hp noble gas with O_2. Low density gas mixing allows for the thorough mixing of high volumes of hp gas and high volumes of O_2 at low densities. Gas mixing occurs quickly due to the long mean-free-path of the gases at low densities, and the gas can be allowed to mix for longer without the fear of significant relaxation, as despite being at significant concentrations (i.e. 20 %) O_2 density (which effects T_1 time [2]) is still low. This is of significant interest for potential ^{129}Xe T_1-O_2 mapping studies (a natural evolution of ^3He T_1-O_2 mapping and related studies [4-6, 19-21]), where it is vital to achieve good gas mixing as well as to know the exact concentrations of O_2 present in the gas mixture.

5.2 Method

5.2.1 Optical pumping of noble gas

Methods for production of hyperpolarized ^{129}Xe and ^{83}Kr using stop-flow Rb-SEOP has previously been reported [22] and are discussed in detail in **Chapter 3** and **Chapter 4**, so only details relevant to these experiments will be discussed here.

For experiments using the high-pressure mixing method the two optical pumping mixtures were used in this study; 25% Xe and 75 % N_2 and 50 % Kr and 50 % N_2. SEOP cell pressures were kept around 120 kPa. Typical apparent polarizations under these conditions were assumed to be ~30 % for ^{129}Xe and ~4 % for ^{83}Kr. These assumed values are based on occasional polarization measurements taken during this study and work detailed in **Chapter 3**. SEOP cells were replaced periodically to ensure that an adequate polarization was obtained.

For the low-pressure mixing method SEOP was conducted at 220 kPa; 25% Xe and 75 % N_2 and 25 % Kr and 75 % N_2 optical pumping mixtures were used (a different Kr mixture was used as this was all that was available at the time the experiments were conducted).

5.2.2 Gas delivery and mixing for high-pressure gas mixing

Mixtures of N_2 and O_2 (99.999 % pure; Air Liquide, Coleshill, UK) containing various concentrations of the two constituent gases were mixed in a storage tank (1400 ml, Fig. 5.1) and left for at least six minutes to mix. Storage tank

pressures typically started at 230 kPa and would provide enough gas for five repeat measurements.

The hp noble gas mixture was vacuum shuttled into the pre-evacuated mixing volume (45 ml) by opening it to the SEOP cell. Gas transfer was stopped once the pressure in the mixing volume was approximately 50 kPa. After the gas transfer the remainder of the system was evacuated. The N_2-O_2 mixture from the storage tank was then transferred to the mixing volume via pressure equalization and the gases where allowed to mix for a short time (~ 5-10 seconds). The rest of the system was evacuated during this time, as there was concern that gases would not mix correctly in the tubing of the mixing system.

The gas in the mixing volume was then transferred into either a syringe, or into a detection cell (either glass or acrylic) depending on the experiment being run.

Small quantities of noble gas isotope where used for two reasons. First, it reduced errors from incomplete gas mixing between the hp gas mix and N_2-O_2 mixture. Because of fast ^{129}Xe relaxation in the presence of O_2, prolonged mixing times will have adverse effects on the signal to noise ratio of the measurements By using a very small *probe* amount of hp gas mixture (with a high hp gas to N_2 ratio), adding the hp gas mixture to an already well mixed N_2-O_2 will have little effect on the overall O_2 density.

Small quantities of noble gas will also reduce the intrinsic NG-NG relaxation, although this is unlikely contribute significantly in the presence of O_2.

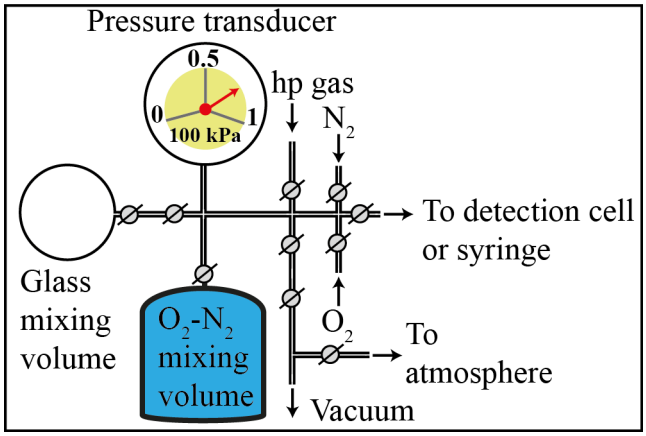

Fig. 5.1– High-pressure O_2 gas mixing system. *Many minutes before experiments were conducted a quantity of O_2 was transferred into a pre-evacuated O_2-N_2 mixing volume. The volume was closed, the system evacuated, and N_2 was used to pressurize the O_2-N_2 mixing volume using a high-pressure N_2 supply (~ 300 kPa). The mixing volume was closed again and the gas lines were evacuated. After the O_2 and N_2 had been left to mix for some time (typically for the duration of the SEOP of the noble gas), a small amount of hp gas was vacuum shuttled into the glass mixing volume, which was then closed. The gas lines were evacuated again and the O_2-N_2 mixture was used to pressurize the glass mixing volume. The system was evacuated again and the gas in the glass mixing volume (now a mixture of O_2-N_2 and hp gas) was shuttled into an evacuated detection cell or syringe. For experiments not using a lung, after the shuttle was complete, the system was vented to atmosphere to ensure that ambient pressure was achieved in the detection cell.*

5.2.3 Gas delivery and mixing for low-pressure gas mixing

The piston extraction-compression unit described in **Chapter 4** was utilized to mix hp gas with a selected concentration of O_2. Initially a vacuum of 0 ± 10 Pa in the volume $V_{extract}$ was obtained. SEOP conducted at 220 kPa resulted in a pressure of close to 11 kPa in $V_{extract}$ after opening $V_{extract}$ to the SEOP cell for 5 seconds. The valve at the front of the volume is closed and the connecting lines were evacuated: These lines were then pressurized with O_2. The volume $V_{extract}$ was re-opened to the gas lines and the new total pressure was recorded; from this the oxygen density was delivery could be calculated. The volume $V_{extract}$ was re-sealed and the connecting lines were evacuated again. Finally the back of the extraction chamber was pressurized driving the piston forwards and the hp gas is delivered as described earlier.

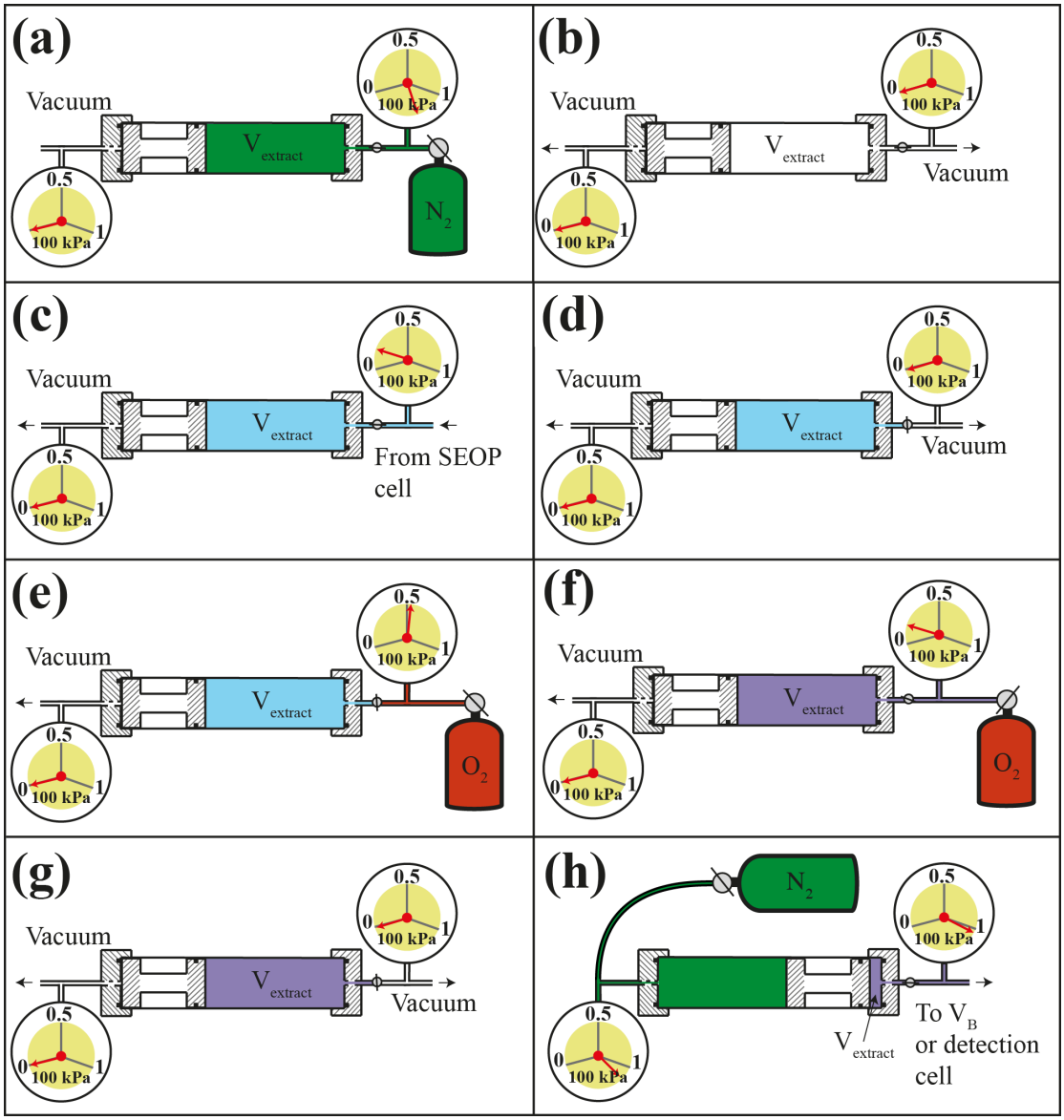

Fig 5.2 – Description of the mixing and delivery of hp gas and O_2 for T_1 measurements. ***(a)*** *The piston was pushed to the back position through the pressurization of $V_{extract}$ with N_2 and evacuation of the back chamber.* ***(b)*** *$V_{extract}$ was evacuated to prepare for hp gas extraction from the SEOP cell.* ***(c)*** *Hp gas extraction from SEOP cell was now complete and $V_{extract}$ was filled with low-pressure hp gas.* ***(d)*** *The volume, $V_{extract}$, was isolated from the gas lines with a valve and the gas lines were evacuated.* ***(e)*** *The gas lines were pressurized with O_2.* ***(f)*** *$V_{extract}$ was opened to the gas lines, resulting in an equalization of pressure between the gas lines and $V_{extract}$. $V_{extract}$ was at very low pressure so the gas transfer was always O_2 into the volume.* ***(g)*** *The volume, $V_{extract}$, was isolated from the gas lines with a valve and the gas lines were evacuated of excess O_2. The hp gas and O_2 were given 5 seconds to mix during this time.* ***(h)*** *The back chamber was pressurized with N_2 forcing the piston to move forward thus compressing the hp gas-O_2 mixture. The gas is then delivered as described earlier.*

5.2.4 NMR instrumentation

Experiments were conducted on a Bruker Avance 400 MHz micro imaging system in a 9.4 T wide bore superconducting magnet as described previously. The magnet was equipped with water-cooled gradient stack keeping the bore at a temperature of 285 K (12 °C) throughout the experiments. NMR spectra were obtained using three custom built probes tuned to 110.6 MHz and 15.4 MHz for ^{129}Xe and ^{83}Kr measurements respectively. The probes used to acquire spectra in the bulk gas phase or porous media were 15 mm saddle coils; the coil for measurements in excised rat lungs was a 25 mm birdcage coil.

T_1 relaxation values were calculated using a nonlinear least-squares fitting of NMR signal intensity as a function of time (Eq. 5.1) [23], of sixteen evenly spaced medium flip angle (12°) RF pulses. Signal intensities were normalized to the intensity at t = 0. Fittings accounted for spin-destruction due to RF pulses.

$$f(t) = \cos\theta^{t/\tau} e^{-\frac{t}{T_1}}$$

[Eq. 5.1]

Where θ is the flip angle of each pulse, τ is the time interval between pulses and T_1 is the longitudinal relaxation time.

5.2.5 Detection cells

Two types of detection cell where used in this study. An acrylic detection cell with a vacuum tight screw top for inserting the porous media was used for the ^{129}Xe experiments using high-pressure gas mixing that did not involve rodent lungs. The cell was a few millimeters longer than the detection region of the coil.

For ^{83}Kr and ^{129}Xe experiments using low-pressure gas mixing experiments a glass detection cell was used. The glass cell was designed to fill the coil region. Untreated borosilicate glass was chosen for ^{83}Kr as the T_1 time in this type of glass in known to be long [24]; given the lower signal intensity afforded by ^{83}Kr (compared to ^{129}Xe) it was desirable to retain as much of the polarization as possible.

Spin-destruction of the hp gas occurs as a result of RF pulses. Due to the size of the acrylic container it was possible that diffusion of gas from the unexcited region or the gas delivery line (also outside of the window of RF excitation) could alter T_1 times if too large a flip angle was used. Fitting the natural log of the integrated signal should provide a linear fit as a function of time (Eq. 5.2 [23]).

$$f(t) = \cos\theta^{t/\tau} e^{-\frac{t}{T_1}}$$

[Eq. 5.2]

Experimentation determined that a flip angle of 12° was small enough that diffusion did not have a bearing on the results over the longest timescale required for these experiments.

5.2.6 Preparation of porous medium

A foam porous medium (pores sizes approximately 0.3 mm – 1 mm) provided by Nestle Foam Industries (Indore, Madhya Pradesh, India) was used in this study. Subsequently, the exact make-up and the manufacturing processes involved in the medium's construction where not revealed.

The medium was baked overnight in a vacuum oven at over 370 K prior to use to remove any moisture. The porous medium was then placed under vacuum between experiments. A minute prior to the start of any experiment the acrylic cell holding the medium would be placed under N_2 and then evacuated a number of times to remove leftover O_2.

5.2.7 Preparation of excised rat lungs and lung ventilation

Male Sprague-Dawley and Brown Norway rats (Charles River, Margate, UK) weighing 200 - 450 g were used in this study. Rats were humanely euthanized in accordance with accordance with A(SP)A 1986 (Animals for Scientific Procedures Act 1986) by an overdose of pentobarbital (Sigma-Aldrich ltd, Gillingham, UK). Lungs were extracted using a method similar to that detailed in **Chapter 4**. Therefore procedural details will not be repeated here. As before, the lungs were ultimately inserted into a sealable ventilation chamber. For these experiments the volume pulled on the syringe (V_I), resulted in roughly 3 ml of gas being inhaled (detailed in Fig. 5.3).

It was important to ensure the lungs were saturated with the correct concentration of O_2 during each experiment. To aid in this prior to an experiment the lung would be ventilated with 30 – 50 ml of a gas mixture of a similar composition to the mixture that was to be used in the experiment (hp gas mixture would be substituted with pure N_2 for pre-experiment ventilation).

When using the high-pressure mixing method, the use of additional gas meant that the 230 kPa N_2-O_2 gas mixture could only be used for two repeat experiments; gas would have to be re-mixed for the second two repeats.

Fig. 5.3 shows the gas delivery to excised rat lungs for the high-pressure gas mixing method. The gas transfer between the piston extraction-compression unit and excised rat lungs has been described in detail in **Chapter 4**.

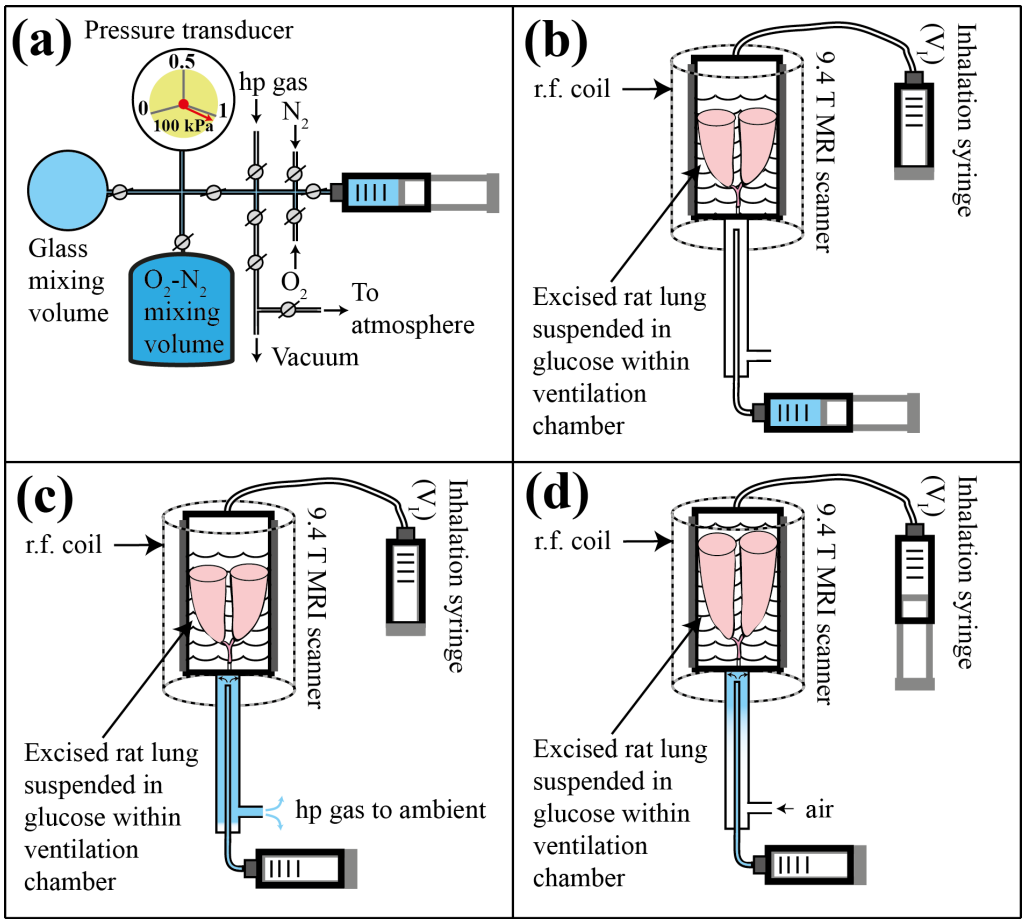

Fig. 5.3 – Diagram detailing the gas delivery to excised rat lungs for the high-pressure gas mixing method. (a) Gas transfer to the syringe. *The system displayed in Fig. 5.1 is shown again, an overpressure in the glass mixing volume allowed a glass syringe to be filled with the hp gas-N_2-O_2 gas mixture.* ***(b) The excised lung.*** *The syringe was attached to a line that connected to the bottom of the lung ventilation chamber. The lung was suspended in glucose inside of the chamber.* ***(c)*** *Pressure was applied to the syringe, displacing the existing gas in the line connected to the lung ventilation chamber. A vent to atmosphere prevented the line from exceeding atmospheric pressure.* ***(d) Lung inhalation.*** *The inhalation syringe was pulled and the glucose level and lung are forced to rise, resulting in the lung inhaling the hp gas-N_2-O_2 gas mixture from the line. The NMR sequence was run shortly after the inhalation.*

5.3 Results

5.3.1 ^{129}Xe T_1 as a function of O_2 density using the high-pressure gas mixing method

Fig. 5.4 shows the relaxation rate of ^{129}Xe ($1/T_1$) as a function of O_2 density under various conditions: in the bulk gas phase, in a porous medium, and in an excised rat lung (Brown Norway). For clarity each of these relationships has been displayed on there own (Fig. 5.4b-d) as well as together (Fig. 5.4a).

Data was analyzed using Igor Pro 6 (WaveMetrics, Lake Oswego, Oregon, USA). Four or more T_1 measurements were taken for each O_2 concentration, typically five (in some cases only four of the measurements would be used, as occasionally one of the five values would be discarded as an outlier). Measurements were averaged with the standard deviations of the averaged $1/T_1$ rates being taken and used for the error bars shown on Fig. 5.4.

It can be observed that in all cases there is a strong linear relationship between relaxation rate and O_2 density. This is in-keeping with previously reported behaviour in the bulk gas phase [2, 11]. The *relationship* observed in the porous media and lungs is consistent with what has previously been assumed [14]. It is important to note that in all of the cases presented here there is an intercept point with the axis of the graph where the O_2 density is negligible. This offset has a finite, non-zero value due to surface relaxation that remains constant independent of the O_2 density as previously been shown by Mair *et al.* [14].

Surface relaxation is more prominent when either the porous medium or lung is present, given the substantially increased surface area that the ^{129}Xe comes into contact with. Despite likely having a larger surface area than the porous medium (this cannot be determined for certain without conducting a more complete study into both media) the surface relaxation caused by the lung is less than that observed within the porous medium. This is likely due to the lung being hydrated. Previous work has shown that surface hydration can significantly increase T_1 times for ^{129}Xe [24].

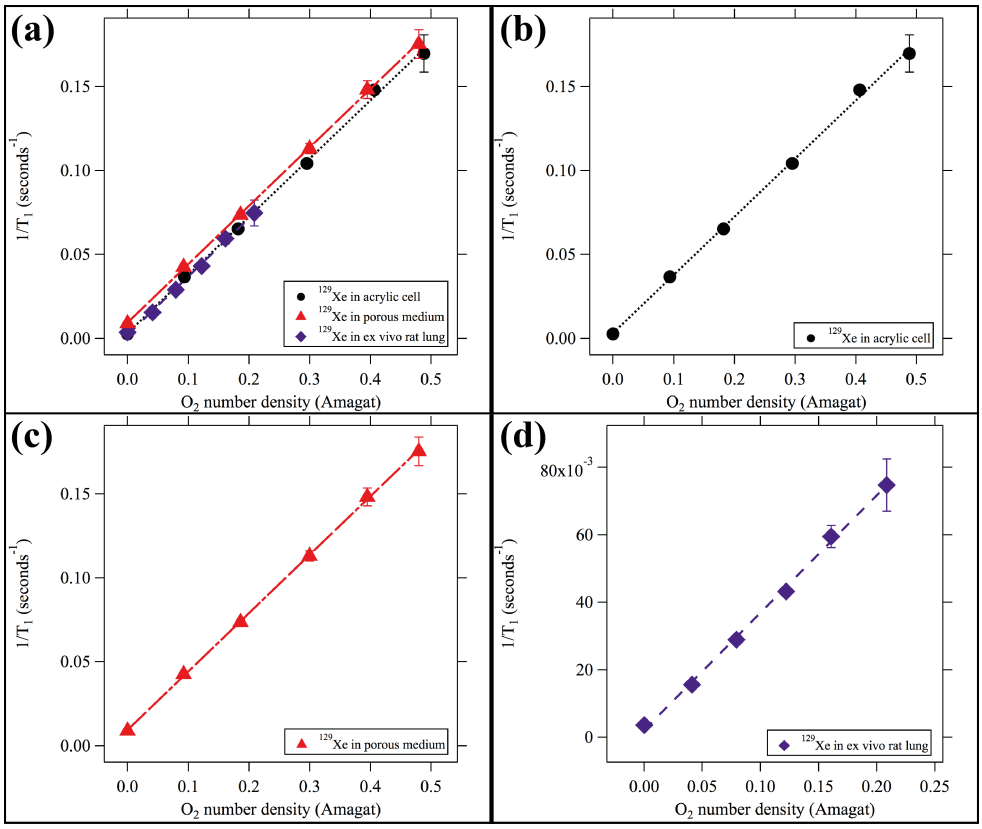

Fig. 5.4 – Relaxation rate ($1/T_1$) of ^{129}Xe as a function of O_2 density (a) Shown for the bulk gas phase, in the presence of a porous medium, and inside an excised rat lung. *The relationship between the relaxation rate and O_2 density is linear and does not change between any of the data-sets. It is also in agreement with literature values.* ***(b) In the bulk gas phase. (c) In the presence of a porous medium.*** *Note that there is an offset on the y-axis caused by surface relaxation.* ***(d) Inside an excised rat lung.*** *Only one rat lung dataset (Brown Norway rat) is presented here.*

The relaxation rate dependence on O_2 density, as well as the real and predicted relaxations due to surface interactions have been displayed in Table 5.1. Complimenting this are data taken from the literature showing the relaxation rate dependence on O_2 density.

Table 5.1 – Relaxation rate as a function of O_2 density is given for both these experiments and from literature. *These are given with details of what conditions the function was obtained under. Also displayed are the predicted values of relaxation rate in the absence of O_2 (due to surface relaxation) and the corresponding value recorded experimentally.*

Conditions	***Relaxation rate as a function of O_2 density (s^{-1} amagat^{-1})***	Relaxation rate in the absence of O_2 from fitting (s^{-1})	**Relaxation rate in the absence of O_2 from experimental observation (s^{-1})**
Acrylic cell, 9.4 T	*0.347 ± 0.006*	0.003 ± 0.002	**0.003 ± 0.000**
Glass cell, from literature, 9.4 T (Jameson *et al.*[2])	*0.343*	N/A	**N/A**
Glass cell, from literature, 4.7 T (Mair *et al.* [14])	*0.348*	0.0333	**N/A**
Plastic cell, from literature, 74 mT (Kraayvanger *et al.* [11])	*0.401 ± 0.121*	N/A	**N/A**
Porous medium, 9.4 T	*0.348 ± 0.003*	0.009 ± 0.001	**0.009 ± 0.000**
Excised rat lung, 9.4 T (1st lung. Brown Norway rat)	*0.347 ± 0.008*	0.002 ± 0.001	**0.004 ± 0.000**
Excised rat lung, 9.4 T (2nd lung. Sprague-Dawley rat)	*0.332 ± 0.006*	0.002 ± 0.001	**0.003 ± 0.000**

All of the functions of relaxation rate compared to oxygen density acquired in this work are in agreement with one another within the error. Only the data by Jameson *et al.* can be directly compared to this work, as the function is slightly dependent on the magnetic field strength [2]. Both the acrylic cell and excised lung data are in agreement with the value given by Jameson *et al.* The porous medium relationship is not in agreement within its error, however as the value is in close agreement with the other values found in this work it seems likely that the error quoted for the porous medium relationship is an underestimate.

The slight disagreement between the observed and predicted relaxation rates in the rat lungs are likely caused by the presence of small quantities of O_2. These being present either due to inadequate flushing of the lung between experiments, leaking into the system, or O_2 diffusing through the delivery line into the lung (as this line is open to atmosphere).

It is likely that the very low error on all of the experimental measurements in the absence of O_2 is affected by a leakage or the retention of O_2. Due to the sensitivity of ^{129}Xe T_1 very small quantities of O_2 could dramatically affect T_1. Given that T_1 in these cases is so long when compared to T_1 in the presence of

substantial quantities of O_2, this will alter $1/T_1$ comparatively little and have little bearing on the observed trend.

5.3.2 ^{83}Kr T_1 as a function of O_2 density using the high-pressure gas mixing method

Fig. 5.5 shows the relaxation rate of ^{83}Kr ($1/T_1$) as a function of O_2 density. The figure also shows a plot comparing the functional relationship between relaxation rate and O_2 density for ^{129}Xe and ^{83}Kr. This clearly demonstrates that the presence of O_2 is far more detrimental to ^{129}Xe polarization than ^{83}Kr polarization in accordance with the theory.

As with ^{129}Xe (and ^{3}He [3]), the relationship observed for ^{83}Kr is linear. There is an offset where the O_2 density is negligible caused by surface relaxation, as with ^{129}Xe, this offset propagates through to higher O_2 densities.

The same data analysis was applied to the ^{83}Kr measurements as described for the ^{129}Xe measurements.

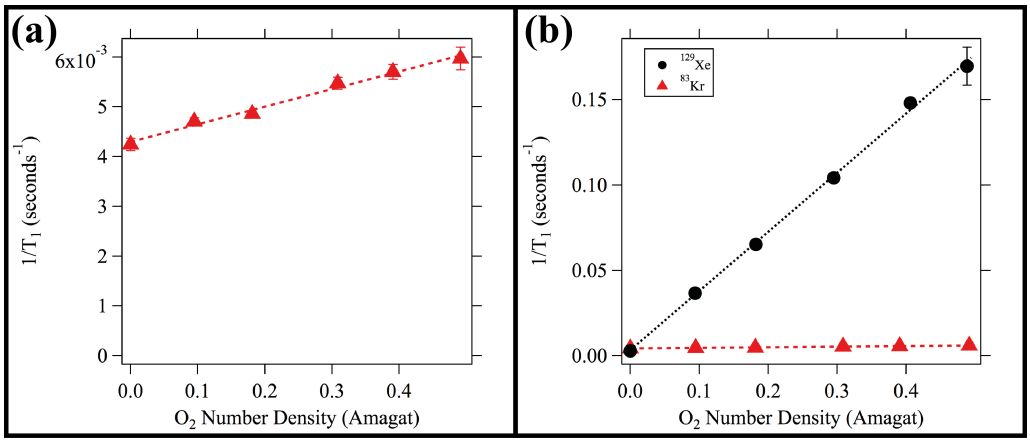

Fig. 5.5 – Relaxation rates ($1/T_1$) of noble gases as a function of O_2 density (a) ^{83}Kr relaxation shown for the bulk gas phase in a glass detection cell. *The relationship between the relaxation rate and O_2 density is linear as seen in literature for ^{129}Xe and ^{3}He.* ***(b) ^{83}Kr and ^{129}Xe relaxation shown for the bulk gas phase on a single graph for comparison purposes.*** *While not a completely rigorous comparison as the experiments were conducted in different types of detection cell (glass and acrylic respectively), this figure illustrates the relative insensitivity of ^{83}Kr T_1 to O_2 density.*

Table 5.2 – ^{83}Kr relaxation rate as a function of O_2 density extracted from Fig. 5.5. *As with ^{129}Xe, the predicted values of the relaxation rate in the absence of O_2 (due to surface relaxation) and the corresponding value recorded experimentally are given.*

Conditions	***Relaxation rate as a function of O_2 density (s^{-1} amagat^{-1})***	Relaxation rate in the absence of O_2 from fitting (s^{-1})	**Relaxation rate in the absence of O_2 from experimental observation (s^{-1})**
Glass cell, 9.4 T	*0.00353 ± 0.00020*	0.00430 ± 0.00006	**0.00424 ± 0.00013**

The result obtained falls between values previously observed in the two literature studies to look at the affect of O_2 density on ^{83}Kr T_1 [17, 18]; therefore agreeing that ^{83}Kr T_1 is relatively insensitive to the presence of O_2. Both previous studies explored the relationship in tissue, and a more pronounced effect in the absence of tissue is to be expected. This was the case in excised rat lungs where (with the errors) very little relaxation due to O_2 is observed, even at high O_2 concentrations [17].

Comparing the rate of relaxation as a function of the O_2 density for the two isotopes shows that ^{129}Xe is a factor of 98.3 ± 5.8 more sensitive to O_2 density than ^{83}Kr: A factor on this order can be justified by Eq. 5.3, showing relaxation rate as a function of spin, gyromagnetic ratio, and the spectral density function.

$$\frac{1}{T_1} = \gamma_I^2 \gamma_S^2 \hbar^2 S(S+1)\left\{\frac{1}{12}J^{(0)}(\omega_I - \omega_S) + \frac{3}{2}J^{(1)}(\omega_I) + \frac{3}{4}J^{(2)}(\omega_I + \omega_S)\right\}$$

[Eq. 5.3]

By simply taking a ratio of the squared gyromagnetic ratios of the two nuclei gives a factor of 52. This leaves a factor of roughly two between the sensitivity difference and the ratio obtained from the squared gyromagnetic ratios, which may be accounted for in the spectral density function: The spectral density function contains dependencies on both the distance (r^{-6}) as well as on correlation times. It is beyond the scope of this work to fully quantitatively analyse this behaviour.

5.3.3 Mixing hp ^{129}Xe and ^{83}Kr with O_2 using the piston extraction-compression device

The piston extraction-compression device described in **Chapter 4** was found to be a novel way to mix hp gas with a known quantity of O_2. Complimenting the data presented above, T_1 as a function of O_2 density for ^{129}Xe in the gas phase (this time in a glass detection cell), gas phase ^{83}Kr in a glass cell, and ^{129}Xe in two excised rat lungs (Sprague-Dawley have been presented (Fig. 5.6, Table 5.3).

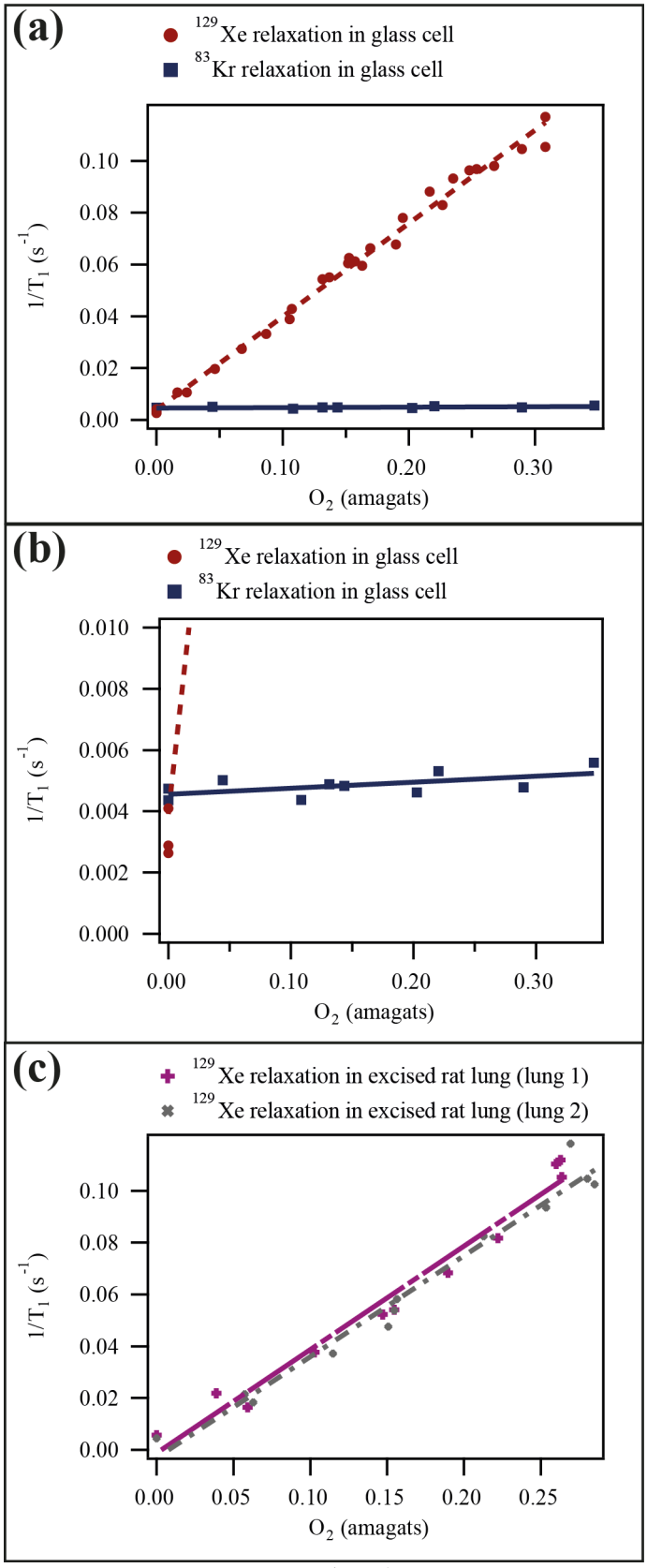

Fig 5.6 - Relaxation rate ($1/T_1$) of hp noble gas as a function of O_2 density. *The functional relationship relaxation rate and O_2 density under the various conditions shown are given in Table 5.3 (**a**) ^{129}Xe and ^{83}Kr in the bulk gas phase in a detection cell. The relationship between the relaxation rate and O_2 density is linear for both isotopes. [Continued overleaf]*

*The functional relationship for ^{129}Xe is in agreement with literature values [2]. **(b)** An expansion of (a) to better show the relationship between ^{83}Kr relaxation rate as a function of O_2 density and highlight the crossing of the Xe and Kr lines. **(c)** ^{129}Xe relaxation rate as a function of O_2 density inside two excised rat lungs. The presence of the rat lung does not seem to have a significant effect on the functional relationship.*

***Table 5.3** – Relaxation rate as a function of O_2 density for both ^{129}Xe and ^{83}Kr; an empty glass cell, and excised rat lungs are explored. Also presented is the relaxation rate in the absence of O_2 taken from the fitting. A literature value is also given. All values are extracted from Fig. 5.6.*

Conditions	***Relaxation rate as a function of O_2 density/s^{-1} $amagat^{-1}$***	**Relaxation rate in the absence of O_2 s^{-1}; taken from fitting**
^{129}Xe, glass cell	*0.360 ± 0.007*	*0.004 ± 0.001*
^{129}Xe, excised rat lung (lung 1)	*0.399 ± 0.023*	*-0.001 ± 0.004*
^{129}Xe, excised rat lung (lung 2)	*0.390 ± 0.022*	*-0.003 ± 0.004*
^{83}Kr, glass cell	*0.0020 ± 0.0009*	*0.005 ± 0.000*
^{129}Xe, glass cell, Jameson *et al.*[2]	*0.343*	-

As expected ^{129}Xe T_1 relaxation rate as a function of O_2 density is in agreement with literature values and the values listed in Table 5.1. This validates this method as a means to mix large quantities of hp gas and large quantities of O_2 well, without dramatically relaxing the hp gas. Experiments mixing hp Xe with ~16 % O_2 showed a T_1 time at the low pressures experienced (105 ± 3 mbar) to be 58 seconds. This is understandable as T_1 depends on O_2 density, not concentration.

^{129}Xe experiments in the lung are also in agreement with values obtained using the high-pressure mixing method and are close to the gas phase and literature values. Ultimately, despite being obtained using different methods, this thesis presents four sets of lungs that exhibit this relationship. It is important to note that the intercepts for both sets of data taken in excised lungs are negative, with very large errors. It is clear from Fig. 5.6c that the experimentally obtained values in the absence of O_2 give longer T_1 times than those predicted by the fitting.

The experimentally obtained values were attained by very carefully flushing of the lungs with O_2. This is a difficult procedure to do correctly as leaving even small quantities of O_2 in either the lungs or the delivery line can dramatically change the T_1 time. Performing this procedure is only possible in an *ex vivo* model. As a result the data fittings were re-fit using this experimentally determined T_1 time in the absence of O_2 as a non-adjustable intercept value. The resulting relationships given in both cases are far closer to the gas-phase value, and values from literature (Table 5.4).

Table 5.4 *– Relaxation rate as a function of O_2 density for ^{129}Xe in both excised rat lungs. The fitting has been given a non-adjustable intercept value where the experimentally determined relaxation rate in the absence of O_2 has been used. These values are extracted from a figure not presented in this work.*

Conditions	***Relaxation rate as a function of O_2 density/s^{-1} amagat^{-1}***	**Relaxation rate in the absence of O_2 s^{-1}**
^{129}Xe, excised rat lung (lung 1)	*0.366 ± 0.012*	*0.006 ± 0 (fixed)*
^{129}Xe, excised rat lung (lung 2)	*0.355 ± 0.012*	*0.004 ± 0 (fixed)*

The ^{83}Kr T_1 relaxation rate as a function of O_2 density is not in agreement with the value found in **Section 5.3.2**. Given that finding the ^{129}Xe relationship and showing its agreement with literature show the validity of each presented method, it is unlikely that either method is *wrong*. Rather it is more probable that a nuance of each method is changing the result. The main difference in the two methods is that significantly different concentrations of Kr are used each time. In the high-pressure mixing method ~6% Kr is used, whereas this method uses ~15-25% Kr. When exploring Xe, relaxation due to the formation of noble gas dimmers can be ignored, as relaxation induced by O_2 is by far the dominant relaxation mechanism. This is not necessarily the case for Kr. Cleveland *et al.* have shown that Kr T_1 relaxation is density dependent [25], this is possibly the reason for the difference in values seen here, however full characterization is beyond the scope of this work.

5.4 Conclusion

In conclusion two methods to determine the T_1 relaxation of ^{129}Xe as a function of O_2 density have been presented. These method have been applied in a model system and excised rat lungs. It has confirmed that the presence of a porous medium does not alter the relationship between relaxation rate and O_2 density.

One of these methods also offers the novel possibility of mixing high quantities of hp gas with O_2 well. Utilizing low-pressure systems allows for superior gas mixing, as well as longer mixing times without significant relaxation. This technique may be of interest for ^{129}Xe pO_2 mapping, where knowing the exact concentration of well-mixed O_2 is vital.

Methods were then applied using ^{83}Kr, where the T_1 was shown to be at least 98 times less sensitive to O_2 density than ^{129}Xe. These results varied between the methods used. It is possible that Kr density has a significant effect, however full characterization of the relaxation of Kr in the presence of O_2 was beyond the scope of this work.

^{83}Kr's insensitivity to O_2 is supported by previous work. The insensitivity to O_2, and the relative dominance of surface relaxation, allows for surface-sensitive T_1 contrast in *in vivo* systems in the presence of 21 % O_2 or higher.

5.5 References

[1] T. Hughes-Riley, J.S. Six, D.M.L. Lilburn, K.F. Stupic, A.C. Dorkes, D.E. Shaw, G.E. Pavlovskaya, T. Meersmann, Cryogenics free production of hyperpolarized 129Xe and 83Kr for biomedical MRI applications, Journal of Magnetic Resonance, 237 23-33.

[2] C.J. Jameson, A.K. Jameson, J.K. Hwang, Nuclear-Spin Relaxation by Intermolecular Magnetic Dipole Coupling in the Gas-Phase - Xe-129 in Oxygen, Journal of Chemical Physics, 89 (1988) 4074-4081.

[3] B. Saam, W. Happer, H. Middleton, Nuclear-Relaxation of He-3 in the Presence of O-2, Physical Review A, 52 (1995) 862-865.

[4] A.J. Deninger, B. Eberle, M. Ebert, T. Gro√ümann, W. Heil, H.U. Kauczor, L. Lauer, K. Markstaller, E. Otten, J. Schmiedeskamp, W. Schreiber, R. Surkau, M. Thelen, N. Weiler, Quantification of Regional Intrapulmonary Oxygen Partial Pressure Evolution during Apnea by 3He MRI, Journal of Magnetic Resonance, 141 (1999) 207-216.

[5] J. Yu, M. Ishii, M. Law, J.M. Woodburn, K. Emami, S. Kadlecek, V. Vahdat, R.A. Guyer, R.R. Rizi, Optimization of scan parameters in pulmonary partial pressure oxygen measurement by hyperpolarized He-3 MRI, Magnetic Resonance in Medicine, 59 (2008) 124-131.

[6] K. Cieslar, V. Stupar, E. Canet-Soulas, S. Gaillard, Y. Cremillieux, Alveolar oxygen partial pressure and oxygen depletion rate mapping in rats using He-3 ventilation imaging, Magnetic Resonance in Medicine, 57 (2007) 423-430.

[7] H.E. Moller, L.W. Hedlund, X.J. Chen, M.R. Carey, M.S. Chawla, C.T. Wheeler, G.A. Johnson, Measurements of hyperpolarized gas properties in the lung. Part III: He-3 T-1, Magnetic Resonance in Medicine, 45 (2001) 421-430.

[8] A.J. Deninger, B. Eberle, M. Ebert, T. 13Grossmann, G. Hanisch, W. Heil, H.-U. Kauczor, K. Markstaller, E. Otten, W. Schreiber, ^ 3He-MRI-based measurements of intrapulmonary p~ O~ 2 and its time course during apnea in healthy volunteers: first results, reproducibility, and technical limitations, NMR in Biomedicine, 13 (2000) 194-201.

[9] E.J.R. van Beek, J.M. Wild, H.U. Kauczor, W. Schreiber, J.P. Mugler, E.E. de Lange, Functional MRI of the lung using hyperpolarized 3-helium gas, Journal of Magnetic Resonance Imaging, 20 (2004) 540-554.

[10] S. Patz, F.W. Hersman, I. Muradian, M.I. Hrovat, I.C. Ruset, S. Ketel, F. Jacobson, G.P. Topulos, H. Hatabu, J.P. Butler, Hyperpolarized Xe-129 MRI: A viable functional lung imaging modality?, European Journal of Radiology, 64 (2007) 335-344.

[11] C.P.B. R.J. Kraayvanger, W. Dominguez-Viqueira, J. Parra-Robles, M. Foz, W.W. Lam, G.E. Santyr Measurement of alveolar oxygen partial pressure in the rat lung using Carr-Purcell-Meiboom-Gill spin-spin relaxation times of hyperpolarized 3He and 129Xe at 74 mT, Magnetic Resonance in Medicine, 64 (2010) 1484-1492.

[12] J. Wolber, A. Cherubini, M.O. Leach, A. Bifone, On the oxygenation,Äêdependent 129Xe T1 in blood, NMR in Biomedicine, 13 (2000) 234-237.
[13] J. Wolber, A. Cherubini, A.S.K. Dzik-Jurasz, M.O. Leach, A. Bifone, Spin-lattice relaxation of laser-polarized xenon in human blood, Proceedings of the National Academy of Sciences, 96 (1999) 3664-3669.
[14] R.W. Mair, M.N. Sen, M.D. Hurlimann, S. Patz, D.G. Cory, R.L. Walsworth, The narrow pulse approximation and long length scale determination in xenon gas diffusion NMR studies of model porous media, Journal of Magnetic Resonance, 156 (2002) 202-212.
[15] J.S.S. Theodore Hughes-Riley, David Lilburn, Karl F. Stupic, Galina E. Pavlovskaya, Thomas Meersmann, Exploring T1 and T2 relaxation in excised rat lungs, in: XeMat 2012, Dublin, Ireland, 2012.
[16] P.L. V. Pasquier, A. Delville, 129Xe NMR as a probe of gas diffusion and relaxation in disordered porous media: an application to Vycor, The Journal of Physical Chemistry, 100 (1996) 10249-10256.
[17] K.F. Stupic, N.D. Elkins, G.E. Pavlovskaya, J.E. Repine, T. Meersmann, Effects of pulmonary inhalation on hyperpolarized krypton-83 magnetic resonance T-1 relaxation, Physics in Medicine and Biology, 56 (2011) 3731-3748.
[18] G.E. Pavlovskaya, Z.I. Cleveland, K.F. Stupic, T. Meersmann, Hyperpolarized Krypton-83 as a New Contrast Agent for Magnetic Resonance Imaging, Proceedings of the National Academy of Sciences of the United States of America, 102 (2005) 18275-18279.
[19] J.M. Wild, S. Fichele, N. Woodhouse, M.N.J. Paley, L. Kasuboski, J.R. van Beek, 3D volume-localized pO(2), measurement in the human lung with He-3 MRI, Magnetic Resonance in Medicine, 53 (2005) 1055-1064.
[20] M.C. Fischer, S. Kadlecek, J.S. Yu, M. Ishii, K. Emami, V. Vahdat, D.A. Lipson, R.R. Rizi, Measurements of regional alveolar oxygen pressure using hyperpolarized He-3 MRI, Academic Radiology, 12 (2005) 1430-1439.
[21] B. Eberle, N. Weiler, K. Markstaller, H.U. Kauczor, A. Deninger, M. Ebert, T. Grossmann, W. Heil, L.O. Lauer, T.P.L. Roberts, W.G. Schreiber, R. Surkau, W.F. Dick, E.W. Otten, M. Thelen, Analysis of intrapulmonary O-2 concentration by NIR imaging of inhaled hyperpolarized helium-3, Journal of Applied Physiology, 87 (1999) 2043-2052.
[22] J.S. Six, T. Hughes-Riley, K.F. Stupic, G.E. Pavlovskaya, T. Meersmann, Pathway to Cryogen Free Production of Hyperpolarized Krypton-83 and Xenon-129, PLOS ONE, 7 (2012) e49927.
[23] J.H. Gao, L. Lemen, J.H. Xiong, B. Patyal, P.T. Fox, Magnetization and diffusion effects in NMR imaging of hyperpolarized substances, Magnetic Resonance in Medicine, 37 (1997) 153-158.
[24] Z.I. Cleveland, K.F. Stupic, G.E. Pavlovskaya, J.E. Repine, J.B. Wooten, T. Meersmann, Hyperpolarized ^{83}Kr and ^{129}Xe NMR Relaxation Measurements of Hydrated Surfaces: Implications for Materials Science and Pulmonary Diagnostics, Journal of the American Chemical Society, 129 (2007) 1784-1792.
[25] Z.I. Cleveland, T. Meersmann, Binary-collision-induced longitudinal relaxation in gas-phase Kr-83, Journal of Chemical Physics, 129 (2008) 244304.

Chapter 6

Summary

6.1 Developing ^{83}Kr as a contrast agent for MRI

The principle goal of this thesis was to develop hp ^{83}Kr as a contrast agent for MRI. The ultimate aim is to be able to use hp ^{83}Kr as a diagnostic tool clinically, however given the amount of progress required to reach this point using hp ^{83}Kr clinically was far outside of the remit of this work.

As explained in the introduction to **Chapter 3**, existing work when this thesis was started had allowed for the imaging of *ex vivo* rat lungs [1], however this image was non-slice selective and took multiple gas delivery to acquire. Surface sensitive T_1 measurements in *ex vivo* rat lungs were also achieved [2], however these were non-spatially resolved measurements limiting there potential diagnostic value. In order to be able to use hp ^{83}Kr imaging clinically, as well as take advantage of its surface sensitive T_1 relaxation, the signal intensity from the hp ^{83}Kr is a major limiting factor.

Chapter 3 outlines a method utilizing low pressure optical pumping that dramatically increased the polarization of the gas, reaching an apparent polarization of 4.4 %, as opposed to the ~ 1 % quoted for the imaged discussed above. Leading to a signal-to-noise ratio improvement of greater than a factor of 2.

SEOP is typically conducted at pressures above ambient. The procedure for hp ^{83}Kr delivery described previously involved opening a syringe to an above-ambient-pressure SEOP cell. The pressure differential resulted in the transfer of hp gas between the SEOP cell and syringe. Adjusting the pressure in the SEOP cell could alter the amount of gas produced. This is not possible when the SEOP cell is kept under ambient pressure, as required for the procedure in **Chapter 3**. Therefore a method to extract hp gas from the SEOP cell, and then compress it was sort. This was not a trivial task as the rapid quadrupolar-driven T_1 relaxation of ^{83}Kr had to be considered, limiting the types of materials that could be used in the compressor as well as transit times in the device.

The final design involving a pneumatically driven acrylic piston similar to a design used by Rosen *et al*. [3] and not unfamiliar to those working with ^{3}He MEOP [4]. This allowed for the extraction, compression, and delivery to the lung of hp ^{83}Kr with minimal polarization losses (15 % the optimal pressure for SEOP). Ultimately an apparent polarization of 2.0 % was delivered to the lung. As discussed in greater detail in **Chapter 4** there are various small improvements that could be made to further enhance the apparent polarization delivered to the lung.

In particular it should be noted that up-scaling the SEOP system, which should not prove particularly technically challenging, would allow for the generation of more hp gas. The optimal SEOP cell pressure (50 kPa) was not used as not enough gas could be extracted. Dropping to this pressure would allow for a 2.9 % apparent polarization after extraction and compression. Up-scaling the SEOP system is a necessary step for moving to larger animals (and ultimately humans), so would be a logical next step.

Available signal intensity was further enhanced by the use of isotopically enriched ^{83}Kr. This allowed for the first spatially resolved T_1 map in *ex vivo* rat lungs using ^{83}Kr: An important step in the development of ^{83}Kr as a contrast agent, and proving its viability.

While it would be sensible to conclude that a T_1 map using ^{83}Kr should show surface changes in pathological lungs, a further step in developing this technique would be to prove this. A number of pathologies either change the surface-to-volume in the lungs (emphysema [5]), change the surface chemistry of the lung (cystic fibrosis [6]), or cause airway obstruction (COPD). These changes may be identifiable in a T_1 map. Further to this, different pathologies must be investigated with this technique to determine whether different conditions can be identified from one another. Existing hp gas work has looked at diseased animal models, such as emphysema [7] and COPD [8], and these models may be replicated for a ^{83}Kr study.

Moving towards an *in vivo* system is also a necessary step. Having to keep an animal alive will introduce additional technical challenges (although presumable none that have not been overcome for other noble gases), and the motion of the lungs may induce additional polarization losses through increased relaxation. As detailed in **Chapter 5**, one factor that must be considered for an *in vivo* study is the inclusion of O_2 in a breathable gas mixture for an animal. While the effects of O_2 had previously been seen to have minimal effect on ^{83}Kr T_1 relaxation [2, 9] as theory suggests, a study into the relaxation in the gas phase would also prove useful as the O_2 and hp gas mixture should be mixed prior to inhalation. It is important to highlight that while relaxation due to surface effects dominate ^{83}Kr T_1 relaxation, an inhomogeneous gas mixture may include pockets of gas with a far higher concentration of O_2 which will have an effect on T_1 measurements. The low-pressure mixing apparatus described in **Chapter 5**, **Sections 5.2.3**, provides a means to mix the noble gas mixture and O_2 well, and rapidly, with T_1 relaxation minimized by keeping the gas at below ambient pressure for some of the process. A future step would be to make this device compatible with a respirator.

Chapter 5 provides T_1 O_2 measurements for using two different gas-mixing methodologies, and two different densities of Kr in the final mixtures. These results seem to suggest that Kr density has a noticeable effect on the relaxation mechanism even in the presence of O_2, in line with earlier work showing ^{83}Kr density dependant T_1 relaxation [10]. Fully characterizing this behaviour was beyond the scope of this work. Future work to investigate this effect further should utilize the low-pressure mixing apparatus. Switching the Kr-N_2 mixture used for optical pumping would allow for multiple densities of Kr to be investigated rapidly.

6.2 Applying techniques to hp ^{129}Xe

While the body of thesis was focussed towards developing ^{83}Kr as an MRI contrast agent, many of the techniques developed were applicable to hp ^{129}Xe.

Given its higher gryomagnetic ratio, the higher achievable polarization (discussed in **Chapter 3**), and the cheaper cost of enriched ^{129}Xe, ^{129}Xe would be a good complimentary contrast agent to ^{83}Kr for lung studies; in particular for obtaining higher resolution structural images.

Certainly the low-pressure optical pumping and extraction-compression techniques described in **Chapter 3** and **Chapter 4** are of interest for ^{129}Xe as it omits the typically used cryogenic separation step [11, 12]. In a clinical setting where cryogens and cryogen trained personnel may not be in abundance, this offers an interesting alternative where apparent high polarizations can still be achieved.

This technique (using the simpler balloon extraction-compression device) was applied to an *ex vivo* lung study exploring physiological measurements of lung function [13]. Using an *ex vivo* model avoids some of the technical challenges present in *in vivo* studies. This study primarily investigated the post mortem airway responsiveness to a bronchial constrictor, methacholine. The induce bronospam was representative of the effects of various reparatory conditions including asthma and emphysema. The effects of this were reversed using an agent used to relieve bronochospasms, salbutamol (Fig. 6.1).

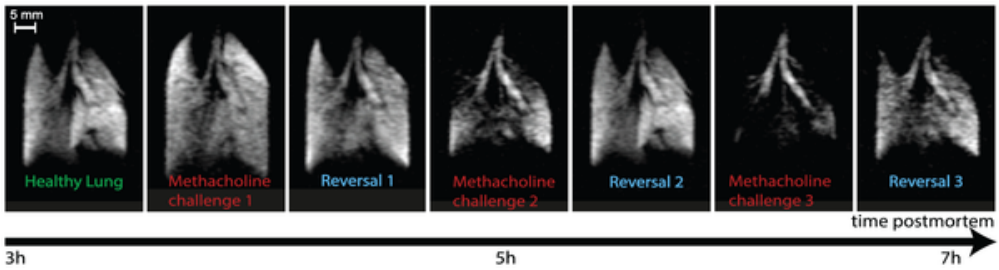

Fig 6.1 – *Taken from literature [13]. Ex vivo, slice-selective, rat lung images after intravenous injections of the bronchial constrictor methacholine and reversals. These experiments where conducted 3 hours post-mortem. Used in accordance with the Creative Commons Licence.*

While further validating the uses of the *ex vivo* model for hp gas studies, which was utilized heavy in this thesis, it also highlighted the potential of the model for drug development. For example, this method allows for measurements to be taken in the complete absence of O_2 (as done in **Chapter 5**), which is not possible *in vivo*.

The longitudinal relaxation relationship as a function of O_2 density for ^{129}Xe was also re-examined in this work and characterizing the relationship was explored further in **Chapter 5**. The relationships insensitivity to the presence of a surface was observed with a porous media and in excised rat lungs. A means to mix ^{129}Xe with O_2 well, without too much relaxation occurring, was achieved by using a low-pressure mixing method. This may prove of interest for T_1-O_2 mapping studies using ^{129}Xe, however such a study was beyond the scope of this work.

6.3 References

[1] Z.I. Cleveland, G.E. Pavlovskaya, N.D. Elkins, K.F. Stupic, J.E. Repine, T. Meersmann, Hyperpolarized Kr-83 MRI of lungs, Journal of Magnetic Resonance, 195 (2008) 232-237.
[2] K.F. Stupic, N.D. Elkins, G.E. Pavlovskaya, J.E. Repine, T. Meersmann, Effects of pulmonary inhalation on hyperpolarized krypton-83 magnetic resonance T-1 relaxation, Physics in Medicine and Biology, 56 (2011) 3731-3748.
[3] M.S. Rosen, T.E. Chupp, K.P. Coulter, R.C. Welsh, S.D. Swanson, Polarized Xe-129 optical pumping/spin exchange and delivery system for magnetic resonance spectroscopy and imaging studies, Review of Scientific Instruments, 70 (1999) 1546-1552.
[4] J. Becker, W. Heil, B. Krug, M. Leduc, M. Meyerhoff, P. Nacher, E. Otten, T. Prokscha, L. Schearer, R. Surkau, Study of mechanical compression of spin-polarized ^{3}He gas, Nuclear Instruments and Methods in Physics Research Section A: Accelerators, Spectrometers, Detectors and Associated Equipment, 346 (1994) 45-51.
[5] G.D. Massaro, D. Massaro, Retinoic acid treatment abrogates elastase-induced pulmonary emphysema in rats, Nature Medicine, 3 (1997) 675-677.
[6] J.J. Smith, S.M. Travis, E.P. Greenberg, M.J. Welsh, Cystic fibrosis airway epithelia fail to kill bacteria because of abnormal airway surface fluid, Cell, 85 (1996) 229-236.
[7] X.J. Chen, L.W. Hedlund, H.E. M√∂ller, M.S. Chawla, R.R. Maronpot, G.A. Johnson, Detection of emphysema in rat lungs by using magnetic resonance measurements of 3He diffusion, Proceedings of the National Academy of Sciences, 97 (2000) 11478-11481.
[8] L.E. Olsson, A. Smailagic, P.-O. Önnervik, P.D. Hockings, 1H and hyperpolarized 3He MR imaging of mouse with LPS-induced inflammation, Journal of Magnetic Resonance Imaging, 29 (2009) 977-981.
[9] G.E. Pavlovskaya, Z.I. Cleveland, K.F. Stupic, T. Meersmann, Hyperpolarized Krypton-83 as a New Contrast Agent for Magnetic Resonance Imaging, Proceedings of the National Academy of Sciences of the United States of America, 102 (2005) 18275-18279.
[10] Z.I. Cleveland, T. Meersmann, Density-independent contributions to longitudinal relaxation in Kr-83, Chemphyschem, 9 (2008) 1375-1379.
[11] N.N. Kuzma, B. Patton, K. Raman, W. Happer, Fast nuclear spin relaxation in hyperpolarized solid Xe-129, Physical Review Letters, 88 (2002) 147602.
[12] G. Schrank, Z. Ma, A. Schoeck, B. Saam, Characterization of a low-pressure high-capacity 129Xe flow-through polarizer, Physical Review A, 80 (2009) 063424.
[13] D.M. Lilburn, T. Hughes-Riley, J.S. Six, K.F. Stupic, D.E. Shaw, G.E. Pavlovskaya, T. Meersmann, Validating Excised Rodent Lungs for Functional Hyperpolarized Xenon-129 MRI, PLOS ONE, 8 e73468.